ERL'09

ENERGY RECOVERY LINAC WORKSHOP

ON THE BEAUTIFUL CORNELL UNIVERSITY CAMPUS, ITHACA, NY USA

JUNE 15–19, 2009

Organizing committee:
Ilan Ben-Zvi, BNL
Bruce Dunham, Cornell
Rodney Gerig, ANL
Ryoichi Hajima, JAEA
Georg Hoffstaetter, Cornell (chair)
Geoffrey Krafft, TJAF
Mike Poole, ASTEC

Cornell organizing committee:
BJ Bortz
Devin Bougie
Georg Hoffstaetter (chair)
Karl Smolenski
Monica Wesley

www.lepp.cornell.edu/events/erl09

Dear Colleagues-

The International Workshop on Energy Recovery Linacs, ERL09 was held June 8-12, 2009 on the campus of Cornell University and attracted more than 170 scientists from around the world. It was the third and largest workshop in the ERL series and the 45th ICFA Advanced Beam Dynamics Workshop. Prior ERL workshops were held at Thomas Jefferson National Accelerator Facility in Virginia, USA in 2005 and at Daresbury Laboratory, UK in 2007.

This meeting gathered a prestigious scientific community focused on next-generation accelerator physics and technology required in Energy Recovery Linacs for many applications from high brilliance x-ray sources and high power FELs to nuclear and high-energy physics colliders. An extensive introductory plenary session presented the status of all of the world's major ERL projects, showcasing the current state of the art and challenges faced in the field. Independent working group sessions addressed (1) high brightness electron guns of the DC, RF and SRF varieties, (2) optics and beam dynamics, and (3) RF and SRF technologies. Joint sessions allowed participants of different working groups to interact with each other. In closing, plenary reviews from each working group were presented.

The venue was timely and suitable as Cornell University is currently developing a proposal to build a large scale ERL for x-ray science, extending Cornell's existing circular accelerator with a 5GeV linac and a new accelerator complex. Nearly all participants toured the prototype ERL injector, the SRF laboratory, and the DC-gun test stand. The workshop banquet was held in conjunction with the CHESS annual x-ray users group meeting to bring the accelerator and x-ray researchers together socially with an eye on future professional interaction.

We were more than happy that many participants expressed their gratitude and considered the ERL 09 workshop a resounding success. We look forward to seeing you again at the next ERL workshop, to be held at KEK in Tsukuba, Japan in October of 2011.

Georg Hoffstaetter, Professor of Physics, ERL 09 Workshop Chair
Karl Smolenski, ERL 09 Editor

Contents

Organizing Committee

Ilan Ben-Zvi	BNL
Bruce Dunham	Cornell University
Rodney Gerig,	ANL
Ryoichi Hajima	JAEA
Georg Hoffstaetter (Chair)	Cornell University
Geoffrey Krafft	TJNAF
Mike Poole	ASTEC

Program Committee

Ivan Bazarov	Cornell University
Sergey Belomestnykh	Cornell University
Joseph Bisognano	SRC
Andrew Burrill	BNL
Eric Chojnacki	Cornell University
David Douglas	JLAB
Pavel Evtushenko	JLAB
Massimo Ferrario	INFN Frascati
Efim Gluskin	ANL
Bill Graves	MIT
Kathy Harkay	APS
Carlos Hernandez-Garcia	JLAB
Hiroshi Kawata	KEK
Dmitry Kayran	BNL
Jens Knobloch	BESSY
Gennady Kulipanov	BudkerINP (IAC)
John Lewellen	NPGS/APS
Matthias Liepe	Cornell University
Alex Lumpkin	FNAF
Lia Merminga	TRIUMF (Chair)
Boris Militsyn	Daresbury
Ali Nassiri	APS
George Neil	TJNAF (IAC)
Edward Pozdeyev	BNL
James Rosenzweig	UCLA
Robert Rossmanith	ANKA
Siegfried Schreiber	DESY
Jacek Sekutowicz	DESY
John Smedley	BNL
Susan Smith	Daresbury
Todd Smith	Stanford (IAC)
Jochen Teichert	FZR
Nikolay Vinokurov	Budker INP

Local Organizing Committee

BJ Bortz	Cornell University
Devin Bougie	Cornell University
Jeanne Butler	Cornell University
Georg Hoffstaetter (Chairman)	Cornell University
Karl Smolenski (Editor)	Cornell University
Michael Roman	Cornell University
Monica Wesley (Secretary)	Cornell University

ERL'09

Cornell University, 2009

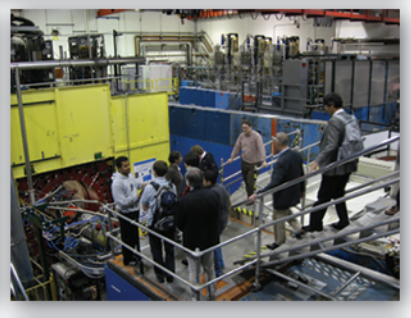

Geometry Optimization of DC and SRF Guns to Maximize Beam Brightness

M.N. Lakshmanan and I.V. Bazarov, CLASSE, Cornell University, Ithaca, NY 14853, USA
T. Miyajima, Photon Factory, KEK, Tsukuba, Japan

Abstract

A set of geometries for DC and SRF guns is studied from the perspective of beam dynamics. The geometries are parameterized and are made a part of an optimization process that minimizes emittance downstream of the gun following the emittance compensation solenoid. The setups simulated are kept to realistic field strengths by imposing an empirical gun voltage breakdown law in the DC gun case and a maximum achievable surface magnetic field for the SRF gun case.

INTRODUCTION

To realize their fullest potential for a range of applications, Energy Recovery Linacs require high brightness high current electron sources operating beyond the state of the art. Photoemission guns, operating with either DC or continuous duty RF fields, are the technology of choice. Very high accelerating gradients at the photocathodes are required to counteract the space charge forces acting on the electron bunches. In DC guns, the strength of the field is typically limited by the field emission and related high voltage breakdown phenomena. Superconducting RF (SRF) guns have the potential to overcome the limitations imposed on DC guns and allow higher operating gradients. The highest accelerating field that can be supported in an SRF gun is limited by the highest (critical) magnetic field on the cavity surface which leads to cavity quenching, even though other practical causes (e.g. field emission) may limit the gradient to much lower values. To transport the space charge dominated beam from the gun to an energy boosting linac, a high gun voltage is also desirable. In addition to high longitudinal accelerating field, field components leading to transverse focusing in the gun are important to ensure proper beam matching and high degree of emittance compensation.

Overall, the gun design is subject to a number of conflicting requirements. For a example, a stronger transverse focusing in DC guns via cathode electrode shaping typically reduces the available accelerating field otherwise possible for the same cathode-anode separation and gun voltage. Similarly, empirical data on voltage breakdown for large area in-vacuum electrodes suggests that much higher gradients are possible at the expense of a shorter gap between the electrodes and the correspondingly reduced gun voltage. Time-varying nature of fields in SRF guns introduces additional complications: the optimal phase of laser pulse arrival can be chosen either to maximize the accelerating gradient at the photocathode, the beam energy at the exit of the gun, or by requiring that the transverse momentum imparted to off-axis particles in the gun nearly does not depend on the position of particles inside the bunch [1]. All these considerations in turn are a function of the gun geometry making it a critical factor in determining the quality of the beams produced.

We have developed a technique to optimize the gun geometries using multi-objective genetic algorithms, which minimizes the beam emittance possible out of the gun while subject to a number of realistic constraints limiting the maximum fields in the gun. We outline our method, provide details on the parameterized gun geometries used in the study, and present the results of computer optimizations for low emittance beams possible from a short beamline that uses DC and (S)RF optimized gun geometries followed by an emittance compensation solenoid and a $\sim$ 1m drift.

METHOD DESCRIPTION

Parallel genetic algorithm

We have used a multiobjective evolutionary algorithm run on 160 2 GHz parallel processors to extensively survey the multivariate space for optimum solutions [2]. A detailed list of variable parameters (also known as decision variables) is given in Table 1. Refer to [2] and references therein for the description of inner workings of these algorithms. A brief summary follows for the convenience of the unfamiliar reader. The algorithm begins by running a trial set of solutions. Then the "fittest" solutions are selected from the set based on typically two criteria: beam emittance and the gun voltage or gradient. The optimizer seeks to minimize both objective parameters to produce a high brightness beam using a lower voltage in the gun (i.e. finds the smallest emittance possible at any given gun voltage). To form a new trial set for the next "generation", the algorithm applies two operators to the selected solutions of the previous generation: (1) "crossing" or "mating" of two or more solutions; and (2) slightly perturbing ("mutating") each solution to form new solutions ("offspring"). The process is then repeated with the new trial set and continues for a number of generations, effectively exploring the decision variable space for the best solutions. In the process, the solutions are subject to a set of constraints to ensure physically realistic scenarios. Finally, a set of optimal solutions is presented as the optimal front, the so-called "non-dominated set" or "Pareto front".

Treatment of field maps

Through parameterizations, the gun geometry is made a part of the decision variable space to be explored by

Table 1: Summary of parameters making up multivariate space.

Parameter Name	Comments
α_{DC}	DC gun angle
g_{DC}	DC gun gap
d_{DC}	DC gun recession
α_{SRF}	SRF gun angle
g_{SRF}	SRF gun gap
d_{SRF}	SRF gun recession
R_{SRF}	SRF gun photocathode curvature
E_{peak}	Peak E_z field strength in the gun
$SuperGaussian$	Super-gaussian nature of beam shape
Dip	Dip character of beam shape
$Ellipse$	Ellipse character of beam shape
$Slope$	Slope character of beam shape
$Tail$	Length of beam tail
$\sigma_{x,y}$	Laser spot size
B_{Peak}	Peak B_z field strength of the solenoid
$\sigma_{t,initial}$	Laser duration (fixed for DC guns)
ϕ_0	Initial RF phase (SRF gun only)

the multiobjective evolutionary algorithm. A space-charge code [3, 4] is then used to evaluate beam parameters for a given set of variable parameters (also known as decision variables) using realistic field maps obtained from E&M simulations. The electrostatic fields were obtained using POISSON for DC guns and SUPERFISH for SRF guns [5]. The fields are solved for prior to the optimization algorithm being run rather than being recalculated as a part of the optimization process. The possible gun geometries under exploration are indexed, and the optimizer uses these indexes to select the actual field map. This approach allows one to decouple the optimizer from a particular field map generating code making the optimizer applicable to a diverse set of problems. This is achieved, however, at the expense of requiring a larger amount of storage space, and that the geometry parameters are made available to the optimizer as part of a discrete, rather than continuous, range of values. Because of axial symmetry of the gun, the off-axis field expansion is employed, allowing compact representation of the field maps. E.g. with a typical 100GB storage, on the order of 10^6 field maps can be stored allowing sufficiently fine sampling of say 4-5 geometry parameters. Special care has been taken controlling the mesh quality and residual error in the field solver to ensure that the tabulated values of the field along the axis $E_z(z)$ can be correctly numerically differentiated twice to obtain the first non-linear term in the off-axis expansion.

OPTIMIZATION STUDY

Beamline

To study the effect of gun geometries, we have chosen a simple short beamline, which consists of the gun, the emittance compensating solenoid and a drift. Refer to Table 2.

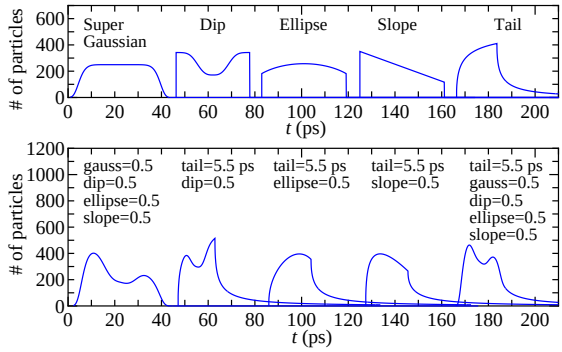

Figure 1: Illustration of the variable parameters specifying temporal laser profile. The top row shows the results of each of the parameters isolated. The second row shows examples of various combinations of parameters. The transverse profile is specified by the first three parameters (Super-gaussian, Dip, and Ellipse).

Laser shaping

The laser beam profile is specified by a set of variables [2] for each plane (transverse and longitudinal) varied over the interval [0-1] along with a tail parameter, as illustrated in Figure 1. Note, however, the temporal tail feature is not used in this study corresponding to the fact of GaAs being a prompt emitter when illuminated with the wavelength 520 nm [6, 7].

DC GUN STUDY

Parameterized gun geometry

The DC gun geometry is parameterized by the angle α_{DC} complementary to that of the electrode surfaces to the beamline, the z-displacement or gap g_{DC} between the electrodes, and the recession or deepening d_{DC} of the photocathode (Figure 2).

Voltage breakdown condition

In order to simulate realistic gun field strengths, empirical gun breakdown laws are enforced as constraints in the optimizations. Following [8], the data on high voltage breakdown from a wide set of measurements for large area electrodes is plotted in Figure 3 as a function of gap. The maximum field values allowed on the cathode electrode surface in the simulations (generally substantially larger than the cathode accelerating gradient, $E_{z,cath}$) are shown in Figure 4 as a function of the breakdown voltage.

Results

As mentioned earlier, increasing α_{DC} in the DC gun increases transverse focusing, but decreases longitudinal field strength at the cathode. Increasing the cathode-anode gap g_{DC} allows a larger voltage if operating near the breakdown, while it also reduces the available gradient at the

Table 2: Parameters and values associated with DC and SRF gun versions of the beamline used in simulations.

Parameter	Value in DC Gun Beamline	Value in SRF Gun Beamline
Gun photocathode location, z_{cath}	0	0
Solenoid location, z_{sol}	0.201 m	0.400 m
Emittance minimization point, z_ε	1.301 m	1.301 m
Thermal energy of photoelectrons, $k_B T_\perp$	120 meV	120 meV
Bunch charge, Q_{bunch}	80 pC	80 pC
Bunch length, $\sigma_{t,initial}$	12 ps	variable, 0-20 ps
Bunch shape	variable, see Fig. 1	variable, see Fig. 1

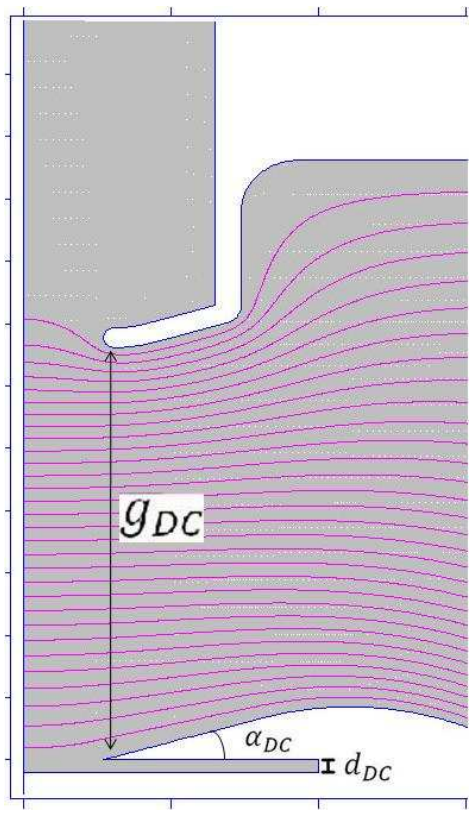

Figure 2: Closeup of the DC gun geometry, shown in the z-r plane, with the definitions of geometry parameters α_{DC}, g_{DC}, and d_{DC} illustrated. The vertical axis is the beamline z; the horizontal axis is that of the cylindrical coordinate r. Equipotential lines are shown.

photocathode and the transverse focusing kick. In addition, larger g_{DC} slightly diminishes the accelerating field at the cathode and the strength of the focusing kick.

The optimization process of choosing the optimal α_{DC} and g_{DC} results in geometries having an approximately $20°$ to $30°$ angle and a 32 mm to 42 mm gap, as can be seen in Figures 5 and 6. The photocathode field corresponding to these figures varies between 3.3 and 5 MV/m (the actual maximum field at the cathode electrode surface is substantially larger, see Fig. 4). It is a surprising result that the photocathode field is not chosen to be at the voltage breakdown limit for the lower gun voltages in the plot. This likely indicates that a particular transverse focusing at the

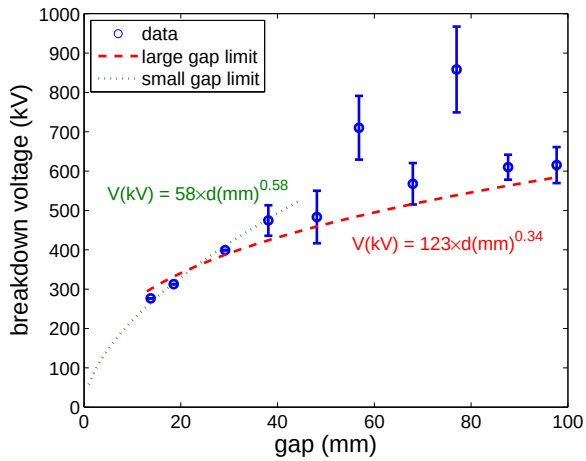

Figure 3: Adapted after [8]. Experimental data overlaid on the graph of breakdown voltage as a function of gap.

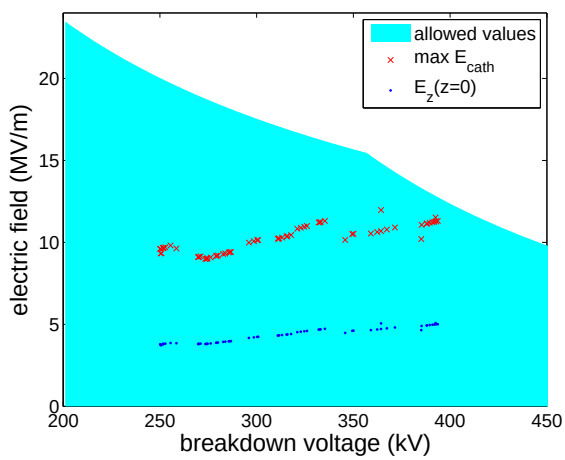

Figure 4: Simulation data from the DC gun optimization overlaid on the graph of maximum electric field as a function of breakdown voltage. $\max E_{cath}$ is the maximum electric field at the cathode electrode allowed under the breakdown constraint. $E_z(z = 0)$ is the electric field at the cathode chosen by the optimizer.

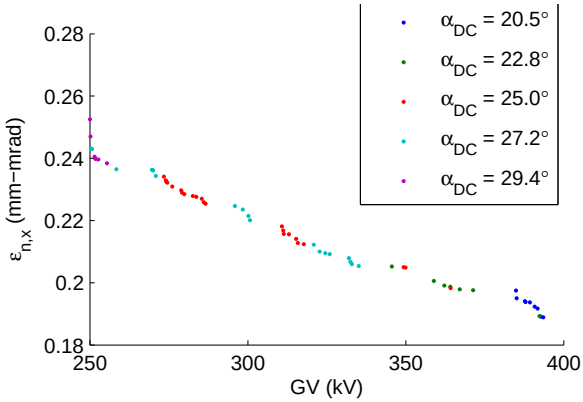

Figure 5: The resulting optimal front from the DC gun optimization after 254 generations, with each solution colored by its respective α_{DC}. The electron beam is represented with 28,000 macroparticles.

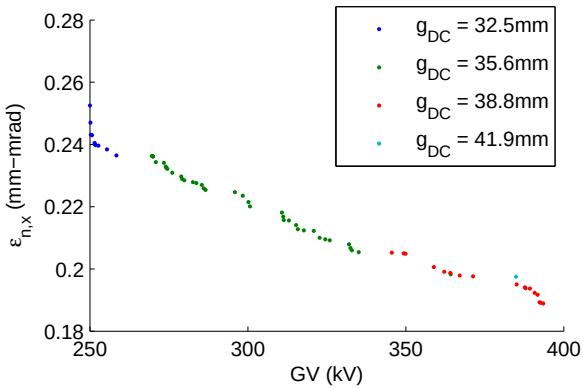

Figure 6: Optimal front from Figure 5, with each solution colored by its respective g_{DC}.

photocathode is crucial to achieving a high degree of emittance compensation. In addition, a shorter cathode-anode gap leads to a stronger unfavorable defocusing by the anode, which can be estimated using

$$\frac{1}{f_{anode}} \approx -\frac{1}{4g_{DC}} \frac{1 + eV_{gun}/mc^2}{1 + \frac{1}{2}eV_{gun}/mc^2}$$

with f_{anode} being the focusing length, eV_{gun} the kinetic energy after the gun, and mc^2 the electron rest mass energy.

The effect of photocathode recess for DC guns is discussed along with that for SRF guns in the next section.

SRF GUN STUDY

Parameterized gun geometry

For the optimization study, we have chosen a half-cell geometry. Additionally, we have simplified the SRF gun geometry from elliptically shaped, as required to mitigate multipacting, to a simpler shape shown in Figure 7 akin to a pillbox cavity. The SRF gun geometry is parameterized

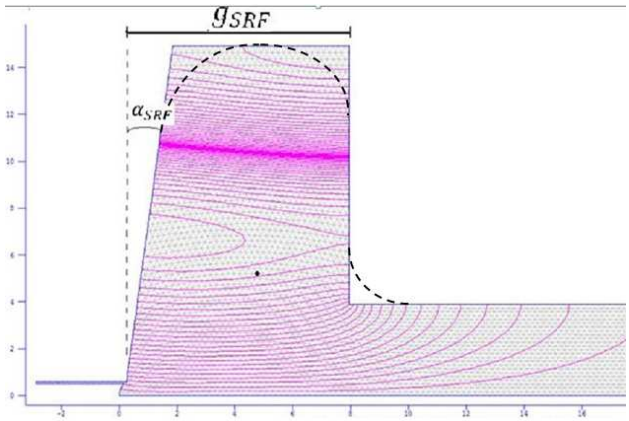

Figure 7: Simplified SRF gun geometry, shown in the z-r plane, with the definitions of the parameters α_{SRF} and g_{SRF} illustrated. The axes here are reversed from those used for the DC gun in Figures 2: the horizontal axis is the beamline z; the vertical axis is that of the cylindrical coordinate r. Lines of constant rH_ϕ, where H_ϕ is the magnitude of the azimuthal component of the magnetic field are shown.

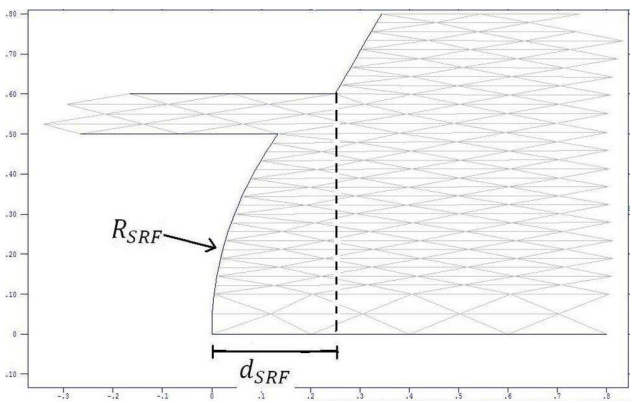

Figure 8: Close-up of the photocathode from Figure 7 with the definitions of the parameters d_{SRF} and R_{SRF} illustrated.

by the angle α_{SRF} complementary to that of the cathode surface to the beamline, the z-displacement or gap g_{SRF} between the photocathode and the other wall of the cavity, the deepening d_{SRF} and radius of curvature R_{SRF} of the photocathode surface (Figure 8), features originating from [9].

In the case of the SRF gun, an additional fourth parameter needs to be introduced to tune the cavity resonant frequency to 1.3 GHz, making it a dependent parameter. This fourth parameter is the equator radius of the cavity.

Cavity quenching condition

For a properly designed SRF gun, the field strength would be typically limited by the maximum achievable surface magnetic field $H_{SRF,crit}$ [10]. The routinely achieved surface fields in SRF cavities (TESLA 9-cell cavities oper-

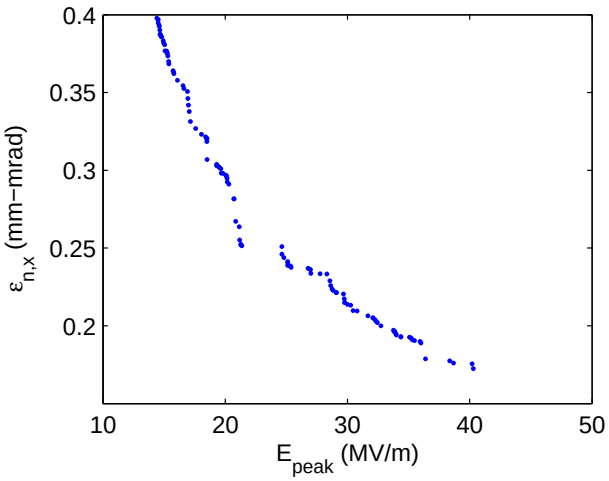

Figure 9: The resulting optimal front from the SRF gun optimization after ∼100 generations. The electron beam is represented with 28,000 macroparticles.

ating at 20 MV/m accelerating gradient) are slightly above $B_{SRF,crit} = 0.12\,\mathrm{T}$ [11]. Therefore, the SRF guns in this study have been chosen not to exceed $B_{SRF,crit} = 0.12\,\mathrm{T}$ to account for possible reduction in the gradient due to the introduction of the photocathode into the SRF gun cavity.

Results

Unlike α_{DC} in DC guns, increasing α_{SRF} in SRF guns was found to decrease focusing fields. Similar to DC guns, a larger α_{SRF} results in weaker longitudinal fields and limits the maximum achievable accelerating field by increasing the ratio of peak surface magnetic field to maximum accelerating gradient H_{pk}/E_{peak}. Therefore, a smaller α_{SRF} appears to be clearly favorable. Enlarging g_{SRF} was found to reduce the focusing fields in addition to slightly weakening the gradient at the photocathode.

The results of the SRF gun optimization are presented in Figure 9. The resulting optimum angle and gap for an SRF gun found through evolution are 7° to 12° and 30 mm to 41 mm respectively. The actual accelerating field at the photocathode at the moment of photoelectron emission varies from 4 to 17 MV/m in Figure 9. Note that our choice of the opening pipe (38 mm radius) may have effectively precluded the exploration of smaller g_{SRF} as the accelerating field tends to be dominated by the longer tail of $E_z(z)$ determined by the pipe opening. Smaller pipe openings will be investigated in [13].

The parameters d_{DC} and d_{SRF} are found to be "sloppy" [12] in the sense that they have a hardly noticeable effect on emittance (less than 5%, compared to keeping $d_{DC} = d_{SRF} = 0$).

Introducing curvature to the photocathode, on the other hand, boosts focusing fields right at the photocathode without sacrificing much the accelerating field. The optimization results support a curvature R_{SRF} of 15 mm.

CONCLUSION

We have presented gun geometry optimizations for DC and SRF guns. We show that very low emittance can be obtained from DC guns with moderate voltages sufficiently below the empirical voltage breakdown condition. SRF guns demonstrate a similar performance, although at larger peak electric fields, while not exceeding limits on the maximum achievable surface magnetic field. We investigate further the factors in the gun geometry affecting the beam brightness in [13].

REFERENCES

[1] I.V. Bazarov and G.A. Krafft, in USPAS course on Recirculated and Energy Recovered Linacs (2008), http://www.lepp.cornell.edu/∼ib38/uspas08/lec3.pdf.

[2] I.V. Bazarov and C.K. Sinclair, Physical Review Special Topics-Accelerators and Beams 8, 34202 (2005).

[3] K. Flottmann, http://www.desy.de/∼mpyflo/.

[4] S. van der Geer and M. de Loos, http://www.pulsar.nl/gpt.

[5] J. Billen and L. Young, Los Alamos National Laboratory, LA-UR-96-1834 (1996).

[6] I.V. Bazarov et al., Journal of Applied Physics, 103 (2008) 054901

[7] I.V. Bazarov et al., Physical Review Special Topics: Accelerator Beam 11 (2008) 040702

[8] P. Slade. The Vacuum Interrupter: Theory, Design, and Application. (CRC Press, 2007).

[9] D. Janssen and V. Volkov, Nuclear Inst. and Methods in Physics Research, A 452, 34 (2000).

[10] H. Padamsee, J. Knobloch, and T. Hays, RF superconductivity for accelerators (Wiley, 1998).

[11] V. Shemelin (2009), private communication.

[12] R. Gutenkunst, J. Waterfall, F. Casey, K. Brown, C. Myers, and J. Sethna, PLoS Comput Biol 3, e189 (2007).

[13] "Geometry optimization of DC and SRF guns to maximize beam brightness", in preparation

ERL09 WG1 SUMMARY: DC GUN TECHNOLOGICAL CHALLENGES

N. Nishimori[1], I. Bazarov[2], B. Dunham[2], J. Grames[3], C. Hernandez-Garcia[3],
L. Jones[4], B. Militsyn[4], M. Poelker[3], K. Surles-Law[3], M. Yamamoto[5]

[1] JAEA, Tokai-mura, Ibaraki 319-1195, Japan

[2] Cornell University, Ithaca, NY 14853, U.S.A.

[3] Jefferson Lab., Newport News, VA 23606, U.S.A.

[4] STFC Daresbury Lab., Warrington, WA4 4AD, U.K.

[5] KEK, Tsukuba, Ibaraki 305-0801, Japan

Abstract

This paper summarizes technological challenges of photoemission DC guns being developed for the future energy recovery linac (ERL) light sources (LS). Anticipated new applications of ERL-LS demand an electron gun capable of producing an extremely low emittance beam at very high average current. The low emittance requires unprecedentedly high voltage equal to or greater than 500 kV between cathode/anode electrodes together with high accelerating gradient on the photocathode. The technological challenge is to develop a high voltage insulator system, which can withstand field emission from the electrodes. A high voltage processing technique and a challenge to suppress field emission are discussed. The high average current requires prolonged cathode life time, which is governed by ion back-bombardment. Challenges to mitigate the cathode damage caused by ion back-bompardment are surveyed. We also discuss high voltage power supply which can afford sufficient high average current, load-lock system capable of accomodating quick cathode exchange to minimize accelerator down time, and vacum technology to suppress both field emission and ion back-bombardment. A gun geometry satisfying both high gun voltage and high accelerating gradient is also proposed.

INTRODUCTION

Electron guns capable of providing reliable CW beam with average current ~100mA and emittance of a few microns (normalized RMS) are being developed for the next generation energy recovery linacs (ERL) light sources in various research laboratories [1,2]. A DC photoemission electron gun with an activated GaAs photocathode illuminated with 532 nm laser light is considered to be one of most promising candidates of the guns for the ERL light sources, since a 350 kV DC gun successfully delivered 9.1 mA CW electron beam to the Jefferson Lab (JLab) 10 kW IR upgrade Free Electron Laser (FEL) [3]. In this paper we survey technological challenges and related developments in DC photoemission electron guns as high current sources for ERLs.

The high voltage power supply determines limits of the maximum beam energy and current from the guns. The low emittance necessary for ERLs typically requires a DC voltage equal to or greater than 500 kV to reduce non-linear space charge effects in the low energy regime [4]. The fluctuation of beam arrival time at insertion devices should be suppressed for pump-probe experiments using fs x-rays from ERLs. A study shows synchronization stability of ERL systems is governed by injector stability [5]. This sets the requirement on the ripple of DC gun high voltage to be on the order of 10^{-3}. The next generation ERL light sources usually require the beam current from 10 mA to 100 mA. Consequently, a high voltage power supply with voltage greater than 500 kV, and stability of 10^{-3} or better and current greater than 10 mA needs to be developed. Conventional Cockcroft Walton high voltage power supplies with voltage above 500 kV and currents up to 10 mA are used in JLab, Daresbury Laboratory (DL), and JAEA/KEK. A high voltage power supply of 100 mA and 750 kV for Cornell Univ. is developed using cross transformer technology [6].

The ceramic insulator is a simple structure to support a cathode electrode inside the vacuum and is electrically connected to a high voltage power supply outside the vacuum. Operation of photoemission guns at voltages greater than 350 kV is however very difficult, since field emission from electrode structures can lead to voltage breakdown, insulator punch-through, and other problems on the ceramics. Recently three ways to resolve the field emission problem have been proposed. The first is the use of a ceramic insulator with a controlled bulk resistivity utilized at DL. This permits any charge build-up on the ceramic surface to be dissipated to ground. Using this insulator technology, 485 kV was achieved during conditioning at DL. The second is an inverted insulator similar to the metal-ceramic X-ray tubes where a high voltage feed passing through the insulator center is connected to a high voltage terminal. The inverted insulator eliminates the electrode structures typical for normal insulators, which might be the sources of field emission. The third is a segmented insulator, where a number of ceramics are stacked in series with Kovar ring electrode sandwiched between adjacent two ceramics. These insulators are widely used in electrostatic

accelerators. The guard rings attached to each electrode prevents field emitted electrons from reaching the ceramic surface. Potentials on the guard rings are fixed with an external resistor divider.

High voltage electrode conditioning up to a voltage typically 20-30% higher than operational is required to reach high photocathode dark lifetime each time after the gun chamber is exposed to air. No unique recipe for high voltage conditioning exists. Gun conditioning using noble gases can be employed to successfully process field emission sites in the gun. Successful experience at JLab and DL using krypton in high voltage processing is described.

Suppression of field emission from the cathode electrodes is essential to protect the ceramic insulator, avoid pressure rise and other problems such as punch-through on the insulator surface. Several laboratories have developed test stands for dark current measurements between large area cathode and anode electrodes to determine the best materials and surface cleaning techniques for dark current suppression. A combination of molybdenum cathode and titanium anode was reported to be the best combination a few years ago by a group at Nagoya Univ. [7]. Employing high pressure rinsing technique used for SRF cavity cleaning is proved to be effective to suppress dark current from the cathode electrodes [8]. This was one of the highlights of the previous ERL workshop [9]. Since these separate measurements were performed with a gap shorter than the real scale electron gun system at voltage much lower than 500 kV, construction of real scale test stands is planned at several laboratories. A new real scale study by Jlab polarized gun group shows that niobium electrodes demonstrate smaller dark currents than stainless steel. Vacuum determined by pump system and outgassing rate of vacuum chamber materials governs the cathode lifetime [10]. Vacuum in the 10^{-10} Pa range with a partial pressure of oxidant like oxygen of less than 10^{-12} Pa are required in the gun chambers as the result. The NEG pump speed was measured as a function of pressure by the JLab polarized gun group [10]. A massive pump unit of 22,000 l/s NEG and 400 l/s ion pumps is used for the Cornell gun to reach mid 10^{-10} Pa [8]. Outgassing from vacuum chamber materials can be suppressed by treating the material or using different materials from stainless steels. A 400 °C/96 hours bakeout for SUS304 and SUS316L in the air as well as vacuum is found to reduce the outgassing rate to as low as $2\text{x}10^{-14}$ l·Torr/$s^{-1}cm^{-2}$ [11]. This technique is used in JLab and Cornell Univ. The outgassing rate of chemically polished titanium is claimed to be $4.5\text{x}10^{-16}$ l·Torr/$s^{-1}cm^{-2}$ [12]. This material is used in preparation and high voltage chambers for JAEA/KEK gun system.

Load-locked preparation systems are used to heat clean activate and store the photocathodes, then transfer them into the high voltage gun chambers. Separate preparation systems from the high voltage chamber are widely used in GaAs photocathode based polarized and un-polarized guns inclusive Cornell ERL installation [8], and currently implemented in the JLab FEL, DL ALICE, and JAEA/KEK guns. The separate system easily accommodates several photocathode pucks for reduction of machine down–time, and permit testing of different cathode materials. A survey of various preparation systems used in DC photoemission guns is presented.

Photocathode operational lifetime is limited by the ion back-bombardment, where residual gas between cathode and anode electrodes is ionized by the electron beam and accelerated towards the cathode surface. The lifetime can be improved by increasing the drive laser spot size, since the ion damage would be distributed over a larger area while the ion production rate remains the same. Lifetime enhancement was observed for larger laser spot sizes at JLab polarized gun [13]. The ion production in a beam transport line downstream from the anode electrode is another source of ion back-bombardment. A positive potential barrier to repel the ions [14] has been experimentally tested at JLab [15] and University of Mainz in their polarized guns. The results of the test are described in this paper.

The lower limit of achievable beam emitance was recently formulated [16], which shows that employing photocathode material with low thermal emittance and applying high accelerating field on the photocathode are the keys for generation of high brightness beam. An actual gun design requires additional design parameters such as optimal gun voltage, transverse focusing, and voltage breakdown criteria. The gun geometry can be optimized by a computer simulation which takes into account of all the gun parameters. A segmented gun design is proposed to decouple two conflicting requirements of a higher gun voltage with a large cathode/anode gap and a higher accelerating field with a small gap.

HIGH VOLTAGE POWER SUPPLY

B. Dunham

The high voltage (HV) power supply for a DC photocathode gun is one of the most important, but often overlooked components of the entire system. A well established set of demands is required prior to considering what power supply to obtain. In this section, a description of these requirements will be covered.

The first item to determine is the highest voltage needed for routine operation, and what overhead is needed for conditioning. All HV devices must be conditioned above the nominal values in order to obtain stable operation, with +20% being a typical number for industrial devices. Photocathode guns, particularly those using vacuum sensitive photocathodes, often require additional margin to have good cathode dark lifetime. Dark currents (from field emission) in the pA range are sufficient to produce noticeable local heating and light (x-rays and UV) which contribute to secondaries and vacuum level increases. For example, if 500 kV is the desired operating value, 600 kV would provide the minimum acceptable overhead.

For any gun that injects a beam into an RF accelerator, control of the arrival time, or phase jitter, of the electron bunch is of critical importance. The phase change at a distance L away from the gun caused by gun voltage variation is given by

$$\Delta\varphi = 2\pi f \frac{L}{c} \frac{\gamma - 1}{(\gamma\beta)^3} \frac{\Delta V_{gun}}{V_{gun}},$$

where φ is in radians, f is the RF frequency, c is the speed of light, and $\Delta V_{gun}/V_{gun}$ is relative ripple of the gun voltage. In terms of RF phase, variations of the order ± 1 degree are acceptable for low emittance beams. For example, at 1.3 GHz, ± 1° is approximately ± 2 ps, corresponding to a shift of ± 450 volts (0.18%) 1 meter away from a 250 kV gun. The voltage ripple needs to be specified over the frequency ranges present in the power supply, typically up to 60 kHz (or more) for modern switching supplies.

Even monitoring ripple at the levels required at the higher frequencies for a particular power supply may not be straightforward. In such a case, we consider using a time-of-flight detector (a beam position monitor, for instance) downstream from the gun to monitor the arrival time of the electron bunches. This can easily measure the arrival time with picosecond accuracy at many tens of kilohertz, and the resulting signal can be sent back to the power supply feedback control loop. For known problem frequencies or instabilities in the HV power supply, one could also consider *feed-forward* methods.

The current and current stability are the next most important requirements. The current is determined by the maximum needs of the accelerator at the nominal voltage, plus some headroom for controls and future development. Cost of these supplies is typically around $10 per watt, so careful consideration should be given to the maximum level requested. Additionally, much less average current is needed for processing than for beam operations, so it is possible to roll-off the current requirements at higher voltages.

For photocathode guns, the current stability and the response of the voltage to changes in the current is of utmost importance. Drive lasers should be stable in power to < 1%, so the HV should be insensitive to changes in current of this level over a wide frequency range. As the cathode efficiency drops over time, it is expected that the laser power will be increased to compensate and maintain a constant output.

Another concern for photocathode guns used in ERLs is how to ramp-up the current to reach the maximum operating value. Two strategies exist: 1) start in CW mode at low current and ramp up the bunch charge; or 2) start in pulsed mode a full bunch charge and increase the duty factor until CW mode is reached. Both methods have difficulties. For case #1, the focusing changes as the bunch charge is increased, requiring one to either adjust the optics settings to compensate, or pick a sub-optimal setting that can work for the full range of bunch charges. For case #2, one must have a flexible laser pulse generation system that can handle the full laser power without damage for duty factors from 0 to 100%. For existing systems, it is possible to turn on directly to a few mA without tripping of the RF systems. Beyond that, the HV power supply must be able to ramp up the current quickly (50 - 100 ms is desirable) while maintaining a constant voltage at low ripple.

Accelerator designers often want to modulate the beam current, or even make gaps in the pulse train, for numerous reasons. The effects on the power supply response must be studied carefully for such requests, and included in early design of the supply and the control circuitry. As we have seen already, the voltage must be kept constant to a few tenths of a percent in order to minimize phase jitter. An instantaneous drop to 0 current will cause the voltage to rise, and the subsequent turn-on will cause it to droop, leading to transients in the beam and possible beam loss.

There are a number of mechanical requirements to consider as well. Many facilities enclose the high voltage power supply and electron gun in a tank of pressurized SF_6 in order to reduce the size of the device. One alternative is to enclose the supply in a very large faraday cage, and connect the gun and power supply using a cable, and another is to submerse the gun and power supply in an oil tank (often used for klystron modulators) [17]. All three have advantages and disadvantages, for example, using oil is generally not desirable when dealing with the extreme ultra-high vacuum conditions needed for a photocathode gun. SF_6 gas is a greenhouse gas and expensive, so one must provide a means to recover it efficiently. For labs that do not cycle the HV pressure

tank very often, commerical SF_6 recovery systems are available, but tend to take many hours to empty and fill a tank. A custom system can be constructed if frequent empty/fill cycles are needed. There has been some discussion about finding alternative dielectric gasses in case SF_6 is ever banned due to its deleterious effects on the atmosphere, and our community will have to follow any legislative changes closely. In addition, as pressures of 1 to 5 atm are commonly employed, many labs have to deal with recent pressure vessel regulations. The last area to be concerned about is mechanical vibrations, as most SF_6 systems have a fan (or blower) plus heat exchanger to cool and circulate the gas around the HV components. The fans should be either isolated or mounted remotely, and care should be taken to avoid any mechanical resonances in the pressure vessel that are close to the frequencies of the fans.

High voltage electrode conditioning techniques will be covered in another section of this paper. To use a DC power supply for conditioning, a processing resistor must be inserted between the gun and power supply to limit the amount of current drawn during an arc. Values between 10 and 100 M-Ohm are typically used, but the exact value will depend on the system. This resistor must be removed after processing to avoid the voltage drop when drawing high currents during operation. To do this, the SF_6 tank must be opened, or a method for remotely inserting a lower value resistor (or shorting rod) must be included in the design.

Finally, where does one find the kind of power supplies that can meet the requirements discussed above? For voltages up to 225 kV and currents of tens of mA, there are many products available, as this is in the range of industrial X-ray tube manufactures. Beyond this, only a few companies (in the US) produce the kind of supplies needed for very high voltage DC photocathode guns. For example, up to 500-600 kV and currents to ~10 mA, Glassman High Voltage Inc. and Kaiser Systems Inc. make good systems. Kaiser Systems has also made compact supplies to 750 kV/100 mA for the Cornell gun. Pulse Electronic Engineering Co. Ltd. in Japan has made a power supply to 550 kV/10 mA for the JAEA/KEK gun.

HIGH VOLTAGE INSULATORS

L. Jones

The use of a DC photocathode electron gun confers many design and operational advantages compared to RF guns. The flexibility to design a vacuum chamber with any number of ports permits extremely high vacuum levels (XHV) to be achieved, allowing the use of high quantum efficiency cathodes such as Gallium Arsenide, coupled with longer-wavelength drive laser with significantly reduced power compared to RF guns. However, the complication of applying the DC HV bias needed to accelerate the photoemitted electron beam is an issue which is pushing the current boundaries of engineering technology. The insulator must fulfil a number of key operational criteria, specifically: separating the gun XHV vacuum from the pressurised HV insulating gas; providing electrical insulation to the level of hundreds of kilovolts; withstanding field emission and dissipating charge.

Field emission is the primary limiting factor in the performance of a photoinjector gun. The presence of a field emitter can severely degrade the electron beam quality delivered by the gun, or can cause the charging of ceramic insulators. In extreme cases, this can cause failure of the ceramic due to punch-through or tracking, or damage/failure of the vacuum vessel due to localised heating through electron-stimulated desorption. Field emission also affects the vacuum, so severely degrades photocathode lifetime.

Early DC guns such as the IR-FEL gun at JLab [18] used an impregnated surface coating to dissipate any charge accumulated on the ceramic surface through field emission. However, the first embodiment of this coating was not successful as the gun failed to operate at the intended design voltage, though the upgraded gun did perform at its design voltage.

Another solution is the use of a ceramic with bulk-doped controlled resistivity. This approach has been successfully implemented at Daresbury Laboratory using the proprietary WESGO 970CD material. This insulator proved highly effective during HV conditioning to 485 kV, and in beam operations at 350 kV, though problems have been encountered with the long-term reliability of the vacuum joints under load due to thermal cycling during baking. The favourable electrical performance of the material prompted a 3-way collaboration between Daresbury, Jefferson and Cornell, with the aim of finding a workable solution using a bulk-doped ceramic with reliable vacuum joints. Presently, CPI have delivered a 14” unit with a ‘book-end’ style vacuum joint to Daresbury, and Kyocera have delivered a 16” version to Cornell, both using the WESGO material. Neither of these units have yet been tested under electrical or mechanical load.

SLAC proposed the use of an inverted ceramic, using standard components developed by X-ray tube manufacturers [19]. This had the significant advantage of using off-the-shelf parts, so was cheap, but the draw-back was that the power supplies and ceramics are only rated to 225 kV, so limiting the operational voltage of a gun based

on this technology to perhaps 200 kV. At Jefferson Laboratory, the CEBAF source group have recently installed a polarised gun based on this ceramic technology, the characteristics of which match well with their 100 kV gun operating voltage. The IR-FEL group have designed a gun using two inverted ceramics mounted in opposition. These will use the WESGO bulk-doped material, and will be rated for operation at 500 kV. The use of two ceramics in opposition serves to balance mechanical loads within the gun, and to provide geometric symmetry. The shape of the inverted ceramic conveys an additional advantage in that the surface plane of the ceramic is almost perpendicular to the HV cathode ball, so significantly reducing the likelihood of field-emitted electrons impacting directly on the ceramics themselves, and increasing reliability.

The use of segmented ceramics is common in DC electrostatic accelerators. The complete ceramic comprises a series of small hoops stacked alternately with overlapping 'chevrons' which act as shields for the insulating material. The chevrons are highly effective at shielding the ceramic from field-emitted electrons, though clearly there is a large number of ceramic-metal joints which have to be made in the manufacture of such a device. The chevrons also have to be connected via a ladder of resistors to grade their potential, with one end tied to earth. This design has been used successfully for the 100 kV gun at NIKHEF [20], the 200 kV gun at Nagoya University [21], and the 230 kV gun at JAERI FEL [22]. The segmented ceramics employed in the JAEA/KEK 500 kV gun is made by Hitacahi-Haramachi [23, 24]. The high voltage conditioning is under progress. Cornell plan to use a similar design in their next ceramic to be made by Kyocera.

The use is growing of external load-lock cathode preparation systems, and this itself is an important step forward. The use of Caesium in the cathode activation process invariably leads to contamination of the insulator over time, ultimately resulting in its electrical failure. This has been experienced most recently at Daresbury where insulator failure resulted in the failure of the conditioning resistor.

The focus for development should be to design an insulator with appropriate levels of vacuum performance, operating at perhaps 600 kV, and conditioned to 750 kV. Technology and economics may dictate that such an insulator will be in multiple segments, so failure of a single segment will not then necessitate complete replacement of the insulator, though it does mean there are additional vacuum joints which must then withstand repeated cycles of baking under high mechanical load.

HIGH VOLTAGE PROCESSING

C. Hernandez-Garcia

Introduction

The surface chemistry on the Cs:GaAs photocathode imposes extreme requirements for the vacuum in the gun chamber, while the need to extract and quickly accelerate the electron beam demands hundreds of kV with gradients around 10 MV/m. It is not sufficient to polish and clean the electrodes to minimize field emission. After assembling the gun and establishing ultra high vacuum conditions, the electrodes need to be high voltage conditioned. At an average rate of 5 kV per hour, this is a time consuming but essential process before the gun can be operated at the desired voltage.

The JLab FEL team has successfully conditioned two generations of DC photoemission guns to 450 kV for operation at 350 kV [3,25]. However, field emission has caused numerous problems puncturing insulators, opening vacuum leaks and damaging electrodes. These problems are common to all DC photoemission guns.

High Voltage Processing

High voltage conditioning in DC guns is nominally performed under vacuum conditions. Basic requirements include a current-limiting (conditioning) resistor in series with the high voltage power supply (HVPS), the ability to immediately shut-off the voltage at a desired current set point, plus radiation monitors and vacuum gauges in the form of ion pump read-back. It is important to shut the voltage off instead of lowering the voltage when the current reaches the desired limit set point, this allows for any charge accumulation in the insulator to drain while the voltage is ramped back up.

There are commonly three cases of field emission for a particular voltage set point: a) erratic current, b) current increasing with time, and c) self-sustained current. In case a), the usual procedure is to maintain the voltage for a few minutes until the field emission current self-extinguishes, although in some occasions a sudden current burst precedes the emitter burn-off. For case b), while the voltage is held constant, the current slowly increases, eventually reaching the trip limit and turning-off the HVPS. In some occasions, the trip limit is reached suddenly with a current burst, and when the voltage is recovered the field emission current has extinguished; in other occasions, the field emitter can sharpen by surface migration, leading to higher current at the original onset voltage. A sharp emitter is relatively easy to burn off by adjusting the voltage to limit the field emission current at ~10 μA until it self-extinguishes. Case c) is probably the

most difficult to process since the field emission current can be self-sustained at levels beyond 100 μA. At hundreds of kV, there is enough power to cause damage. Pulsing the voltage for a few μs would be ideal, as is done in RF cavity processing. However, the response time of the HVPS is in the order of tens of ms. Typically this type of field emitter burns off in tens of minutes if the voltage is held constant until the field emission current extinguishes.

Beyond ~150 kV, voltage-induced gas desorption contributes to the complexity of the process. In the absence of field emission, the pressure in the gun vacuum chamber rises from 10^{-10} Torr to 10^{-8} Torr with every kV increment, and the Residual Gas Analyzer (RGA) indicates increases in H_2, CH_4, CO and CO_2. The time taken for the vacuum to recover is voltage dependent. Below 200 kV, it takes around 5 minutes; near 400 kV it can take up to 60 minutes. However, field-emitted electrons striking the chamber walls and desorbing gas dominate the vacuum behaviour. This voltage-induced gas desorption phase has a very sharp onset. If the gun is fully-conditioned to 350 kV, it can operate for years at that voltage, but if it is increased by 1 kV, gas desorption is observed again.

High Voltage processing with inert gases

Gas processing is very effective in burning field emitters with self-sustained current. Field emission current ionizes the inert gas atoms that are accelerated towards the negatively biased electrodes, effectively back-ion bombarding the field emitter until the geometry or the work function is altered.

Helium is commonly used for processing superconducting RF cavities and has also shown good results for the Cornell gun [26]. However, there is always a risk to develop a leak especially in the ceramic insulator due to the lack of vacuum diagnostics at the 10^{-5} Torr level where the gas processing takes place. It must be ensured that the pressure is set at the vacuum chamber and not by ion gauges near the turbo pump, where the pressure will be lower. The NEGs do not react with inert gasses and continue pumping other gasses. It should be noted that this process is not a DC glow discharge since the pressure is too low to ignite plasma.

In the JLab FEL gun helium processing was less effective, but krypton quickly burned emitters off below 250 kV, as shown in Fig. 1. A detailed description of the setup is given in [27], later this procedure has also been highly successful used at DL.

After processing a field emitter, the Kr gas can be pumped–out, and the ion pumps turned back on to resume normal high voltage conditioning. However, this procedure did not work for the FEL at 270 kV, and Kr gas processing continued for tens of hours. At 315 kV a pattern was observed in both the current and radiation traces with every kV increment. The pattern resembled the gas desorption phase observed under nominal vacuum conditions, only that the signal from the radiation monitors behaved as the ion pump pressure. The radiation tracked the high voltage current with every voltage increment, showing a sharp rise followed by an exponential decay. High voltage conditioning with Kr was successful in eliminating emitters and at the same time the process had evolved into the gas desorption phase, which continued to 415 kV at a rate of 1 kV/hour, until both the current and the radiation were at baseline. Progress was monitored every ten hours with the gun under nominal vacuum conditions, by verifying that the on-set voltage for observing radiation increased by about 10 kV. Finally, the voltage was ramped to 365 kV and maintained for several hours while both current and radiation remained at background levels [28]. The FEL gun is currently operational at 350 kV.

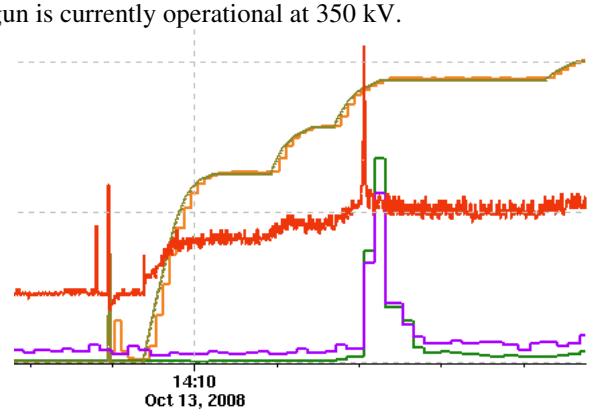

Figure 1: Emitter burning off while ramping up to 250 kV. The horizontal scale is in minutes. The red trace is the current (0-0.5 mA), purple and green traces are the radiation monitors signals (0-100 mR/h), and yellow trace is the voltage (0-400 kV).

FIELD EMISSION MEASUREMENS AT JEFFERSON LAB

M. Poelker and K. Surles-Law

Intdoduction

As mentioned numerous times above, field emission inside DC high voltage photoguns can lead to big problems at accelerator facilities. Constant low-level field emission degrades vacuum within the gun, reducing gun operational lifetime via electron stimulated desorption of gas and subsequent photocathode QE loss

from ion back-bombardment. Large bursts of field emission can be catastrophic, leading to damage of the photocathode and other gun components, particularly the high voltage insulator, which sometimes results in a complete loss of vacuum. These problems were particularly difficult to overcome in older "vent/bake" style photoguns, where the photocathode was activated to negative electron affinity within the high voltage chamber, with cesium serving to reduce the work function of the GaAs photocathode surface, but also inadvertently reducing the work function of the metallic cathode electrode structure as well. Often, a vent/bake gun could support just a few photocathode activations before cesium-enhanced field emission made the gun inoperable. Today, gun groups adopt a load lock-style design, with cesium applied to the photocathode in a separate vacuum chamber isolated from the high voltage region of the gun. The key factors that influence field emission inside modern load-lock style photoguns are the desired operating voltage of the gun, the gun geometry which determines field gradient, and the choice of electrode materials and polishing techniques. Vacuum may not play a role in the onset of field emission, but can contribute to enhancement of field emission via ionization of residual gas and ion back-bombardment. Other factors are frequently discussed, for example, surface cleanliness and contamination, and more academic topics such as the role of hydrogen diffusing from the electrode material and grain boundaries.

Extremely demanding emittance requirements of proposed ERLs necessitate very high bias voltages: ~ 350 kV or more. The field gradient within the gun can be adjusted to some extent, for example by choosing an appropriate cathode/anode gap, and by prudently choosing large distances to other grounded gun components such as the vacuum chamber - but just as ERL emittance requirements dictate high bias voltage, a high gradient within the photogun is unavoidable because the beam must be quickly accelerated to relativistic speed to overcome deleterious effects of space charge. It seems certain that DC high voltage guns for ERLs must operate with gradients of 10 MV/m or more, roughly a factor of two higher than gradients inside the original DC high voltage photoguns used for decades to generate polarized electron beams at nuclear and high energy physics accelerator facilities.

Traditionally, photogun electrodes have been manufactured from vacuum-arc remelt stainless steel, polished by hand to sub-micron finish with diamond grit [29]. More recently, groups have begun to explore in earnest different electrode materials and polishing techniques, recognizing the need to reliably manufacture "quiet" electrodes that can operate at very high bias voltage and gradient without field emission [7,30]. Of note is the extremely thorough study of ref. [7] that explored primary field emission from the cathode electrodes and subsequent field emission enhancement due to ionization of residual gas and ion-back-bombardment of the cathode electrode, including the effect of stimulated desorption of gas from the anode. Their work indicated molybdenum performed very well as cathode material, and titanium serving best for the anode.

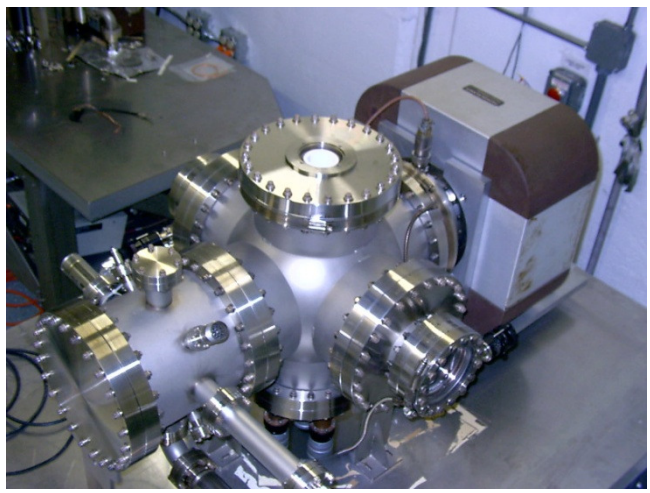

Figure 2: The Jefferson Lab High Voltage Test Stand. Bias voltages up to 250 kV can be applied to cathode electrodes attached to the inverted insulator that extends into the UHV chamber, visible at top of photograph. Vacuum translation stages, bottom of photograph, provide a means to reduce the cathode/anode gap to a few millimeters, to reach gradients > 30 MV/m, but larger gaps more closely explore the field emission properties of actual gun designs.

At Jefferson Lab, a high voltage test stand was constructed (Fig. 2) with an inverted insulator that allows high voltage processing of full-size photogun electrodes up to 250 kV, with a GaAs photocathode installed (but not activated) and with anode/cathode gap that can be adjusted from 4 to 50 mm, to vary the gradient over a large range. Besides providing a means to study different electrode materials and polishing/processing techniques, the test stand provides a means to operate cathode electrodes at actual CEBAF voltage and gradient before installation inside a photogun - electrodes can be re-worked or discarded if found unacceptable without wasting accelerator time. In addition, the test stand provides a means for more "aggressive" high voltage processing techniques without fear of damaging the actual photogun. More recently, the test stand was used to

quantify benefits of krypton-ion processing (krypton-ion back bombardment of field emitters) [28].

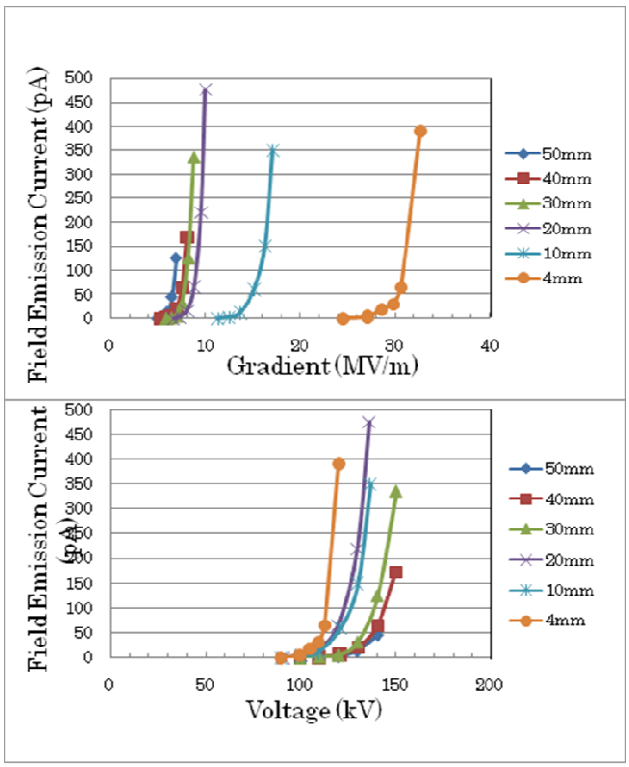

Figure 3: "Benchmark" results from diamond-paste polished 304 stainless steel. The cathode electrode had been used inside a CEBAF 100 kV photogun for many years. Same field emission data, but plotted versus gradient (top) and bias voltage (bottom).

Results

Tests using stainless steel electrodes provide a benchmark against which other electrode materials and polishing techniques are compared. The data in Fig. 3 were obtained using electrodes made of vacuum-arc remelt 304 stainless steel (SS), first polished with silicon carbide paper and then with diamond grit of successively finer grit size. The cathode electrode had been used inside a CEBAF photogun for years, and is considered thoroughly "processed". One obvious feature of these plots is that results obtained with small gaps are not particularly useful – i.e., one cannot assume that since this cathode electrode exhibited no measureable field emission at 25 MV/m with a 4 mm gap, it would perform well at 50 mm gap. Rather, these plots suggest field emission from diamond-paste polished stainless steel electrodes, when configured with typical gun anode/cathode gaps, "turns ON" at disappointingly low values of ~ 5 MV/m and ~ 100 kV.

Everyone knows diamond-paste polishing (DPP) is a labor-intensive process – it can take weeks to polish a complicated electrode structure. And because results often vary sample-to-sample and across laboratories, there are nagging fears that results depend on subtle variations in polishing technique: for example, diamond particles can become embedded beneath "peaks' that get rolled over due to excessive pressure applied to the sample during polishing. For these reasons, groups have re-visited electropolishing as alternative to DPP. Full details of experimental results must wait for another publication, but preliminary results from Jefferson Lab indicate electropolishing provides comparable results as shown in Fig. 3, but requiring significantly less time and effort.

Two single-crystal niobium electrodes were manufactured and evaluated inside the high voltage test stand. Both electrodes were polished using the standard SRF practice known as BCP (buffer chemical polish). Another SRF-practice was employed: high pressure rinsing as a means to remove contaminants. Niobium electrode #1 performed very well, exceeding the performance of DPP stainless steel (Fig. 4), "quiet" to ~ 150 kV with 50 mm gap. Niobium electrode #2, however, performed poorly initially, but improved after several iterations of krypton processing. Regrettably, both electrodes suffered high voltage breakdowns and could not sustain subsequent application of comparable high voltage. This work will continue at Jefferson Lab, including studying other niobium electrodes: polycrystalline material referred to as fine grain and large grain niobium, and using the electropolishing technique.

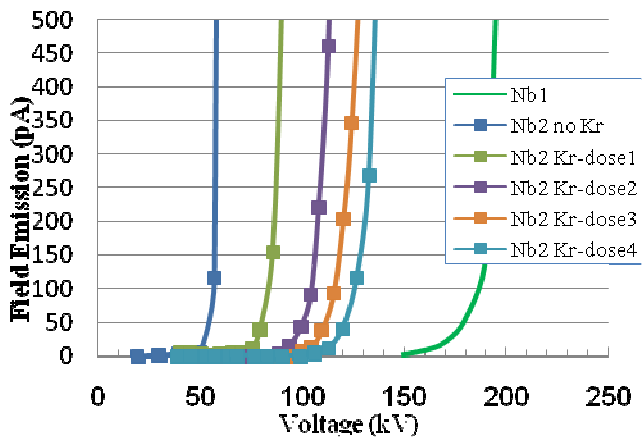

Figure 4: Field emission measurements of two single crystal niobium electrodes, polished with BCP. See text for details.

Table 1: Basic information of gun vacuum systems

Institute	Chamber material	Chamber treatment	Vacuum pump system	Bake out condition	NEG activation	Ultimate Vacuum
Cornell	SUS316L	400°C air-bake, 100 hours	NEG: 20000 L/s IP: 400 L/s	150 °C, 24 hours	400 °C, 45 min	4 E-10 Pa
JLAB FEL	SUS316 LN	400°C air-bake, 360 hours	NEG: 3000L/s IP: 80L/s	250°C 160hours	400°C, 60min	5E-10 Pa
CEBAF	SUS316L & SUS316LN	EP-ed, 400°C vacuum-bake, 200 hours	NEG: 8800 L/s (ten WP1250s) IP: 30 L/s	250°C 30 hours	400°C, 60 min	4 E-10 Pa
Daresbury	SS304L & SS316LN	--	NEG:3,900 l/s IP: 150 L/s	200 - 220 °C ~ 2 weeks	~500 °C, 60 min	2 to 4 E-9 Pa
JAEA(250kV)	Titanium	CP	NEG: 2000 L/s IP: 500 L/s	200 °C 20 hours	450 °C, 60 min	5 E-9 Pa
KEK/Nagoya (200kV)	SUS316L & SUS304L	EP	NEG: 850 L/s IP: 400 L/s	200 °C, ~100 hours	400 °C, ~ 3 hours	2 E-9 Pa

Conclusion

For stainless steel electrodes, keeping gradient below ~ 5MV/m seems prudent, although understandably, this might be impossible for very high voltage ERL photoguns. So the search for materials and polishing techniques that provide quiet electrodes to 10 MV/m at actual gun voltage must remain a critical R&D focus for the DC high voltage photogun community.

VACUUM

M.Yamamoto

The ultra-high vacuum system is indispensable for suppressing ion back-bombardment in photocathode DC guns. This is because the residual gases in the gun vacuum chamber are ionized by the extracted electron beams and accelerated back into the photocathode, resulting in damage of the cathode crystal structure or degradation of the negative electron affinity of the cathode surface. Improving the ultimate vacuum is straightforward way to solve the ion back-bombardment problem.

The ultimate pressure p [Pa] is denoted by $p=qA/S$, where q [Pa m/s] is the outgassing rate of the vacuum chamber material per unit area and unit time, A [m^2] the internal vacuum chamber area and S [m^3/s] the pump speed. Use of a massive pump system and a chamber material with low outgassing rate is essential for achieving the extremely high vacuum (XHV).

The basic information on vacuum system of electron guns at various laboratories are summarized in Table 1. For reduction of outgassing, components installed in the vacuum chamber and chamber itself are rinsed in ultrasonically cleaned acetone, ethanol, or deionized water solutions. They are polished electrolytically or chemically, and degassed by vacuum firing before assembling. The gun chamber is then baked to 150~250 °C for about a day to a week to eliminate hydro-carbons, carbon dioxide, carbon monoxide, nitrogen and water. The partial pressure of water and carbon dioxide should be sufficiently low 10^{-11} Pa or less for long cathode dark-lifetime [2,31]. The most significant source of outgassing in UHV/XHV is mainly hydrogen dissolved in materials. There are two ways to reduce the outgassing rate. One is formation of a passive layer, which acts as a barrier for bulk hydrogen diffusion or inhibits surface processes of adsorption and recombination. The other is formation of a surface layer with low hydrogen content.

Air-baked stainless steel is employed in Cornell University and Jefferson FEL [8,11]. The thick oxide layer formed on the stainless surface after the air-baking reduces the subsequent baking temperature to ~150°C for shorter time duration around a day. The CEBAF injector group employs vacuum baked stainless steel (400°C for 200 hours), which was electro-polished and high pressure rinsed before vacuum baking. A chemically polished titanium used for JAEA/KEK gun has very low outgassing rate of $6x10^{-13}$ Pam/s [12]. Use of other low outgassing materials such as BeCu and SUS316L with TiN coat may help improve vacuum of gun vacuum chambers [32-34].

A non-evaporable getter (NEG) pump and an ion pump (IP) are employed in gun vacuum chambers. The NEG pump provides extensive pumping of the dominant residual gas of hydrogen under UHV/XHV condition, while the IP pumps noble gasses and methane that are

poorly pumped by the NEG pump. The IP pump speed decreases as the operating pressure decreases under UHV condition less than 10^{-6} Pa, since ionization rate of residual gases inside IP becomes low. Recently, M. Poelker et al. performed pump speed measurements of some commercially available IPs under XHV condition. The preliminary data indicates the effective pump speed decreases down to almost zero in the range of 10^{-10} Pa. A cryopump designed carefully to fulfill the XHV specifications may be a candidate as an alternative of IP [35,36].

A limit of ultimate pressure of NEG pumps is estimated from Sievert's law. This gives extremely low equilibrium pressure of hydrogen at the room temperature. However, there are few experimental data of the NEG pump speed in the XHV environment except for ref. [37].

In order to achieve ultimate vacuum of the order 10^{-10} Pa or less with several m^2 vacuum area of a gun chamber, one should use low-outgassing chamber materials of $\leq 10^{-10}$ [Pa m/s] and a vacuum pump with large effective pump speed of >5 m^3/s under XHV condition.

III-V PHOTOCATHODE PREPARATION SYSTEMS

B.Militsyn

Originally III-V family photocathodes such as GaAs, GaAsP, InGaAsP and similar were mainly used in DC guns for production of polarised electrons. As grown, these materials have a positive electron affinity, which for GaAs is 4 eV. In order to make GaAs photocathodes able to emit electrons when illuminated by 532 nm light, typical for ERL DC guns, its surface should be brought to Negative (NEA) or small, less than 1 eV, Positive Electron Affinity (PEA) state. This process basically comprises deposition on the atomically-clean photocathode surface of a thin layer of Cs and an oxidant, typically O_2 or NF_3, and is called activation. Before the activation, the surface of the photocathode is heat cleaned in order to remove As and Ga oxides.

At earlier stages of the photocathode gun development and at certain installations operating currently, heat cleaning and activation of the photocathodes were performed directly in the gun [21,38-40]. Eventually it was recognised that activation in the gun had serious disadvantages: activation process control was poor, it was difficult to provide extra high vacuum conditions for photocathode operation, products of the photocathode heat cleaning and vapour of caesium could contaminate the gun ceramic which limited the maximum high voltage achievable in the gun and, finally, replacement of the photocathode required several weeks which was not acceptable for practical installations.

In modern photoinjectors, activation takes place in a dedicated Photocathode Preparation System (PPS). The first PPS was developed at SLAC [41] and operated with polarized electron source of the Stanford Linear Collider. It was a dedicated vacuum system consisting of two chambers - loading and preparation. The photocathode was brought into the loading chamber, and then transferred to the preparation chamber, whose vacuum is maintained at extreme high vacuum (XHV) conditions, with a vacuum manipulator. For replacement of the photocathode, the PPS was temporally attached to the gun forming united vacuum system; the photocathode activated in the preparation chamber was then transferred to the gun with a manipulator. The SLAC preparation system was a great step forward for improving quality of photocathode preparation, although the downtime required for photocathode exchange was still high – a several hour period.

The next step in PPS development was made at the University of Mainz in the framework of the development of a polarized electron source for the MAMI project [42]. In the MAMI design, a side-loading mechanism for the photocathode was implemented which allowed the PPS to be permanently connected to the gun. This dramatically reduced the downtime required for photocathode exchange to the order of one hour. Another solution, which permits the PPS to be permanently connected to the gun and allows the more preferable back-loading of photocathodes, was proposed at SLAC in their so-called "Inverted gun" [17]. Permanent PPS connection was also used in traditional guns with a double insulator scheme [19,43] where the PPS was connected to the gun from the high voltage side with an additional full voltage insulator. Recent gun designs are based on vertical orientation of the insulator and horizontal orientation of the electrode system [8,44] also allowing back-loading of the photocathode.

Modern PPS consist typically of two chambers: a loading chamber (LC) and an activation chamber (AC). Recently, some PPS have also been equipped with a Hydrogen Cleaning Chamber (HCC). Figure 5 shows an engineer's view of the three chambers PPS which has been designed for operation with ALICE ERL [45].

As activated photocathodes are very sensitive to the presence of oxidants in the residual atmosphere, for example the 1/e lifetime of GaAs does not exceed $2 \cdot 10^{-8}$ mbar·s of oxygen exposition [46], XHV conditions are maintained in the AC. The typical pressure in an AC is less than 10^{-11} mbar, with partial pressures of oxygen, water vapours and CO_2 of less than 10^{-14} mbar. In order to

Table 2: Basic parameters of the preparation photo cathode systems designed for operation with high average current photoinjectors.

Institution/ Installation	Design	Preloading treatment	Preactivation treatment	Activation procedure	Results with bulk GaAs	Rejuvenation procedure	Vacuum conditions	Remarks
Cornell University	Two chambers	Chemical etching (H_2SO_4) and anodizing	Heat cleaning at 550°C for 2 hours	Cs-NF_3 "Yo-Yo"	10-15% at 532 nm	Heat cleaning	PC $5.0\cdot10^{-12}$ mbar LC $5.0\cdot10^{-11}$ mbar	
STFC Daresbury Laboratory	Three chambers (up to 6 samples in carousel)	HCl etching (not yet implemented)	Heat cleaning at 450°C	Cs-O_2/NF_3 "Yo-Yo"	15% at 635 nm	Atomic hydrogen cleaning	PC $1.4\cdot10^{-11}$ mbar LC $5.0\cdot10^{-10}$ mbar HCC $4.0\cdot10^{-11}$ mbar	
JAEA	Two chambers	HCl etching	Heat cleaning at 500°C for 1 hour	Cs-O "Yo-Yo"	7-10% at 633 nm	Atomic hydrogen cleaning (optional)	AC $2.5\cdot10^{-9}$ Pa LC $5.0\cdot10^{-8}$ Pa	
KEK (Nagoya)	Two chambers	HCl etching	Heat cleaning at 500°C for 1 hour	Cs-O "Yo-Yo"	7-10 % at 780 nm	Atomic hydrogen cleaning (optional)	AC $1.0\cdot10^{-8}$ Pa, LC $1.0\cdot10^{-7}$ Pa	
TJNAF/CEBAF	Four chambers inclusive suitcase and bakable adapter		Heat cleaning at 550°C for 2 hours	Cs-NF3 "Yo-Yo"	20% at 532 nm	Heat cleaning	PC $7.0\cdot10^{-12}$ mbar LC high 10^{-11} mbar	Mask activation

routinely maintain such extreme vacuum conditions, AC is usually equipped with a high performance Ion Pumps (IP) and Non-Evaporable Getters (NEG), and it is never ventilated to atmosphere. Vacuum in the AC is measured with an extractor gauge and a RGA.

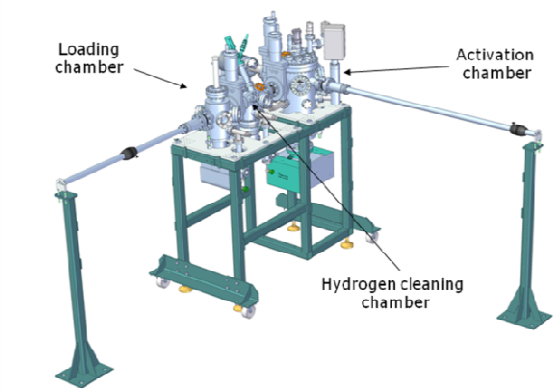

Figure 5: Engineer's view of the Photocathode Preparation System designed for ALICE ERL.

Loading of the photocathode is performed via the LC, which is preferably vented to dry nitrogen gas only during loading. The pumping system of the LC includes an IP and an oil-free preliminary pumping station. After the photocathode is placed into the LC, it is pumped down to a pressure of 10^{-9} mbar and eventually baked out at a temperature of 120-150 °C in order to remove water from the samples. Once acceptable vacuum in the LC is established, the photocathode is heat cleaned at a temperature of typically 600 °C for 1-2 hours. This procedure, depending on PPS design, may take place either in the LC, HCC or AC. Temperature of the samples is measured with a pyrometer. In some installations the surface is etched before loading in a pure nitrogen atmosphere using hydrochloric or sulphuric acid to remove oxides. Thereafter the photocathode is transferred into the LC in a transport vessel in pure nitrogen atmosphere to prevent appearance of new oxides. The heat cleaning temperature of the etched photocathodes may be reduced to 450 °C. Some vendors cover photocathodes with a thin arsenic layer in order to prevent its oxidation. This "arsenic cap" is evaporated before activation. A heat cleaned photocathode is then activated by means of a Cs-O_2 or Cs-NF_3 "Yo-Yo" procedure.

Caesium is evaporated from a Cs dispenser while the high purity oxidant gas is delivered from a cylinder via a leak valve. Sometimes for better control of the gas stream, a computer-controllable piezoelectric leak valve is used. During activation the photocathode is illuminated with a lamp or laser and the photocurrent is monitored with a pico-ammeter. As at high temperature the Cs source may emit ions which mask photocurrent, a modulated laser is preferable. A synchronous detector is then used for current detection.

Activated photocathodes are transferred to the gun using a vacuum manipulator. For a short time, the vacuum valve between PPS and gun is opened, and the depleted photocathode is retracted back to the AC. The freshly activated photocathode is transferred to the gun and the valve is closed. The depleted photocathode may be cleaned and reactivated again. For rejuvenation of a depleted photocathode, atomic hydrogen cleaning is carried out in the HCC [47].

As the lifetime of photocathodes expressed by total extracted charge when operating in a DC gun is restricted to only a few hundred Coulombs [48], corresponding to operational life-time of a few hours at ERL operational

conditions with average extracted current of 100 mA, the PPS should be ready to deliver an activated photocathode every few hours. For this, the PPS will normally contain several photocathodes, one of which is activated.

Presently, PPS design may be considered to be well established. The typical initial quantum efficiency of the activated photocathode can reach 20% at a wavelength of 532 nm making it sufficient for operation in ERL high-current guns.

ION BACK-BOMBARDMENT

J. Grames and M. Poelker

Ion back-bombardment is the key factor limiting photogun operating lifetime. Residual gas inside the gun vacuum chamber and nearby beam line can be ionized by the extracted electron beam or field emission from the high voltage electrodes. Ions produced within or reaching the cathode/anode gap are accelerated toward the photocathode by the gun's static electric field. Ions with sufficient kinetic energy can strike the photocathode surface and sputter away the chemicals used to create the negative electron affinity condition necessary for photoemission. Energetic ions can also penetrate the photocathode surface, damaging the GaAs crystal structure or serving as unwanted dopant species that alter the photocathode band structure, reducing quantum efficiency (QE). This process is illustrated in Fig. 6, with a characteristic photocathode "QE scan" exhibiting the effect of ion back-bombardment.

At CEBAF and other accelerators, production photoguns exhibit charge lifetime of a few hundred Coulombs (i.e., before QE falls to 1/e of initial value). Some ERLs however must deliver thousands of Coulombs per day. To put high current ERL requirements into perspective, consider that a photogun with just 100C charge lifetime could satisfy accelerator requirements for only minutes before some sort of action would be required, for example, move the drive laser spot to a fresh photocathode location, heat/reactivate the photocathode, or replace the photocathode. Each of these actions represents downtime for the accelerator. Therefore, improving vacuum inside the gun is critical for high average current, milliampere-class ERLs: both static vacuum without beam, and during gun operation with beam.

Improving static vacuum inside DC high voltage photoguns has been a central R&D focus for years, with all photoguns today relying on non-evaporable getter (NEG) pumps and ion pumps (to pump inert gasses not pumped by NEGs). It is now typical that vacuum inside NEG/ion-pumped photoguns is in the upper-10^{-12} to low-10^{-11} Torr range but accurate pressure measurement in this range is difficult.

On the static vacuum front, the Cornell group recently verified the efficacy of reducing the outgassing rate of vacuum chamber materials via the LIGO "high temperature" 400C bake process [11], with more than an order of magnitude reduction in outgassing rate compared to "typical" stainless steel baked at 250C. The technique is relatively easy to implement and should provide significant base pressure improvement - provided there are no fundamental limitations of NEGs and ion pumps.

On the "dynamic" vacuum front (i.e., vacuum while operating the gun), it is extremely important to eliminate field emission from the cathode electrode, which can degrade vacuum via electron stimulated desorption. In addition, it is extremely important to effectively manage all of the extracted beam leaving the photocathode, including beam not intentionally produced, for example, from extraneous laser reflections or background light illuminating the activated surface of the photocathode. Anodizing the edge of the photocathode [2], or limiting the active area with a mask [49], are helpful steps toward eliminating this unwanted electron beam. In addition, cathode/anode designers must consider beam transport from the entire photocathode surface, not just from the desired location of the beam. The gun electrodes must be designed to capture the "extra" beam and deliver it far from the gun.

Short of improving vacuum, there are several techniques that can be employed to prolong photocathode lifetime. Hydrogen is the dominant gas species inside a UHV/XHV chamber and the hydrogen ionization cross-section peaks at ~ 30 V, falling sharply at higher voltages [50]. One technique – employed "for free" by the very-high-voltage ERL gun community - is to operate at very high bias voltage. At very high bias voltage (assuming there is no field emission), there should be considerably fewer hydrogen ions created by the extracted beam, although this claim awaits experimental verification.

It has been known for years that ions created near the anode are preferentially directed toward the electrostatic center of the photocathode [51]. Another technique to prolong photocathode lifetime is to operate with the laser beam positioned away from the electrostatic center of the photocathode. Unfortunately, modeling predictions suggest this leads to emittance degradation of the beam [52].

More recently, Grames et al., determined that ions produced downstream of the anode contribute to photocathode QE decay [15], and these ions are also delivered to the electrostatic center of the photocathode. It is relatively easy to eliminate these ions by simply

applying a small positive bias (~ few hundred volts) to an electrically isolated anode.

Finally, Grames et al., determined that operating the photogun with a larger laser spot size can improve lifetime [13], by effectively distributing ion back-bombardment over a larger area of the photocathode. However, this technique (like off-axis drive laser operation) leads to emittance degradation.

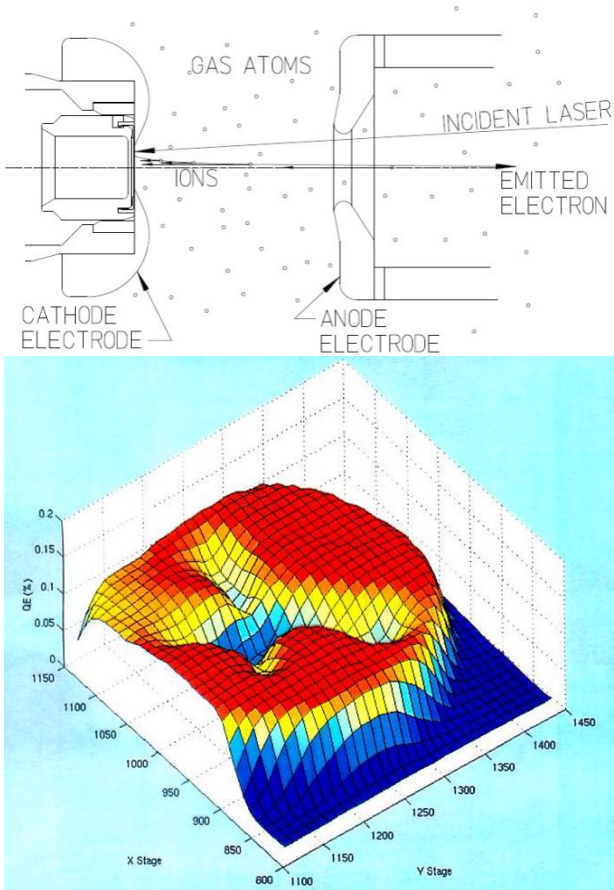

Figure 6: Top: Illustration showing cathode/anode structure, photoemitted electrons and ion back-bombardment for off-axis illumination of photocathode. Bottom: plot of QE across the surface of the photocathode damaged by ions. The electron beam was extracted from three different radial locations. Note QE "trenches" that terminate at a common "electrostatic center".

Conclusion

The "tricks" described above to prolong photogun operating lifetime certainly help enhance our understanding of these complicated devices, but are unlikely to provide sufficient means to meet the requirements of high current ERLs. Therefore, improving vacuum inside DC high voltage photoguns remains an extremely important task. In the realm of improving static vacuum, there are a number of topics that need R&D attention: cryogenic-pumping as an alternative to NEGs and improved vacuum gauging, to accurately measure pressure in the 10^{-12} Torr range and lower. Complimentary studies to identify limitations of NEGs and ion pumps also seem warranted. Finally, there needs to be greater appreciation for the role of cathode electrode design, in terms of transporting all of the extracted beam from the photocathode – both wanted and unwanted beam.

NEW IDEAS AND DESIGN CONSIDERATIONS

I. Bazarov

The photoemission DC guns have been reliably delivering up to about 10 mA of average currents with normalized RMS emittances of ~5-8 mm·mrad. A number of emerging applications nevertheless require substantially improved emittances (on the order of 0.1 mm·mrad) at comparable or higher beam currents. R&D programs are underway in several laboratories to address the outstanding issues for very low emittance DC photoemission guns capable of delivering beam currents of 10-100 mA. Below we survey some new directions under exploration to achieve the improved performance.

Cathode field and thermal emittance

Even for the DC guns operating currently at voltages of up to 350 kV, a significant improvement in beam brightness will be made possible through emittance compensation processes, and a better control of the initial electron bunch 3D distribution via laser shaping. A lower limit to the achievable emittance has been recently formulated for photoemission guns in terms of the cathode field and intrinsic (thermal) emittance of the photocathode material [16]

$$\varepsilon_{\mathrm{nx}}(\mathrm{mm\cdot mr}) = \alpha \times 0.015 \sqrt{q(\mathrm{pC}) \frac{kT_{\perp}(\mathrm{meV})}{E_{cath}(\mathrm{MV/m})}}\,, \quad (1)$$

with q being the charge per bunch, E_{cath} the accelerating gradient at the photocathode and $kT_{\perp}$ the effective transverse energy (temperature) of the photoemitted electrons. The parameter α depends on additional details such as the 3D laser pulse distribution, the degree of emittance compensation, etc. For a well-designed injector system, $\alpha \approx 0.3-0.9$. For example, using typical DC gun parameters: $E_{cath} = 3.5$ MV/m (the gun voltage 350 kV

and the cathode-anode gap of 10 cm), $kT_{\perp} = 120$ meV corresponding to GaAs at 520 nm wavelength illumination [53], and the bunch charge of 80 pC, one concludes from Eq. (1) that emittances of no larger than 0.8 mm·mrad should be achievable. Similar conclusion follows from computer optimizations of the beam dynamics with experimentally benchmarked space charge codes [54]. Therefore, proper realization of space charge emittance compensation is the primary route towards significant reduction in emittance beyond that which has already been demonstrated from DC guns.

Additional improvements in achievable beam brightness will become possible when employing photocathodes with lower transverse energy spread and by increasing the cathode electric field. Without further discussing the important subject of photocathodes for low emittance beam production, we point out several additional considerations to low emittance beam production arising from the gun electrode design.

Optimal Gun Voltage

While the gun voltage is not a parameter that directly defines the beam brightness at the photocathode, $1/\gamma^2$ scaling of space charge forces in the gun vicinity as well as operational experience make it a key design objective for DC guns. Previous simulation studies suggest that a properly designed 400-600 kV DC gun can allow low emittances (0.2 mm·mrad at 80 pC), and that the emittance improvements are modest for gun voltages above 750 kV at these charges [4]. Besides, this gun voltage level is well matched to the use of an RF buncher downstream of the gun for velocity compression.

Transverse focusing

Ideally, external focusing in the gun, either due to electric or magnetic fields should counteract the defocusing due to the space charge, which at the gun exit can be estimated using

$$\frac{1}{f_{s.c.}} \approx -\frac{I}{I_0}\frac{d}{r^2}\frac{mc^2}{eV_{gun}}\frac{1}{\beta\gamma}\ln\frac{2d}{(1+\gamma)z_i},$$

for a cylindrical beam with radius *r*, (peak) current *I*, cathode-anode gap *d*, and normalized momentum $\beta\gamma$ corresponding to kinetic energy eV_{gun}, and z_i being on the order of the bunch dimension ($z_i \sim r$). $I_0 = 17$ kA.

Additional defocusing due to anode is always present in DC guns and contributes further to beam divergence. The effective defocusing is largely independent from the anode geometry and is given by:

$$\frac{1}{f_{anode}} \approx -\frac{1}{4d}\frac{1+eV_{gun}/mc^2}{1+\frac{1}{2}eV_{gun}/mc^2}$$

The required focusing can be achieved through appropriate electrode shaping (Pierce-like electrode geometry) and magnetic solenoidal fields. The former allows focusing in the vicinity of the photocathode but does so at the expense of a somewhat reduced E_{cath} possible otherwise for a flat cathode with the same cathode-anode gap. Magnetic focusing, on the other hand, requires a vanishingly small field at the photocathode to avoid emittance increase due to canonical momentum conservation, and is most effective when the solenoid is placed some distance from the cathode unless a bucking solenoid can be employed. The DC gun geometry typically prevents bucking solenoid coil placement in the immediate vicinity of the photocathode, thus, a combination of both cathode Pierce-like angle and an external solenoid placed right after the gun are needed to achieve the desired focusing effect.

Voltage breakdown criteria

The main technological challenge to the DC guns is due to problems of field emission and the voltage breakdown, which limit the maximum available gradient and voltage. The best practices to the material selection, surface preparation and cleanliness are required in order to achieve the best performance. A body of experimental work on performance of large area electrodes has been accrued over the years, which should serve as a guide when arriving at the actual gun geometry. Most notably, the trade-off of the highest achieved voltage data versus the gap for large area parallel electrodes is summarized in Fig. 7. As a rule of thumb, the electric field should not exceed the breakdown condition anywhere on the surface of the cathode electrode. The actual electric field on the photocathode itself for a given voltage and gap can be noticeably smaller than what's suggested in Fig. 7 when electrode shaping for transverse focusing is employed.

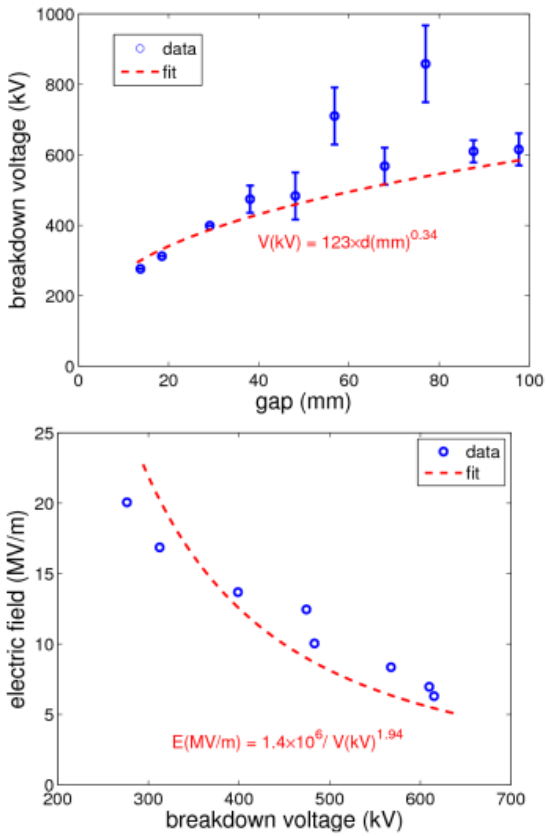

Figure 7: Adopted from [55]: (top) voltage breakdown vs. gap; (bottom) maximum field vs. voltage.

Parameterized gun geometry

Overall, the optimal gun geometry is subject to several potentially conflicting requirements: maximize E_{cath}, increase the gun voltage, and provide a stronger electrostatic focusing at the photocathode. The last two generally lead to a reduced maximum E_{cath} when operating at the voltage breakdown limit. The problem of choosing optimal gun geometry in the cathode-anode region can be most efficiently addressed via computer optimizations: field maps corresponding to a parameterized gun geometry are calculated and the smallest emittance possible with this geometry is numerically determined via space charge code simulations. A scan of the gun geometry parameters (e.g. the gap and the cathode angle) and the gun voltage is then performed subject to a number of realistic constraints to arrive at the optimum geometry for best emittance performance [56]. Figure 8 shows results of such study with optimizations performed for 80 pC/bunch with emittance minimized after a short beamline (1.3 m) consisting of the gun and a favourably placed solenoid. Each point in Fig. 8 corresponds to an optimized gun geometry for the given voltage. The cathode angle and the gap in the plot vary from 20 to 30° and 32 to 42 mm respectively across the gun voltages span.

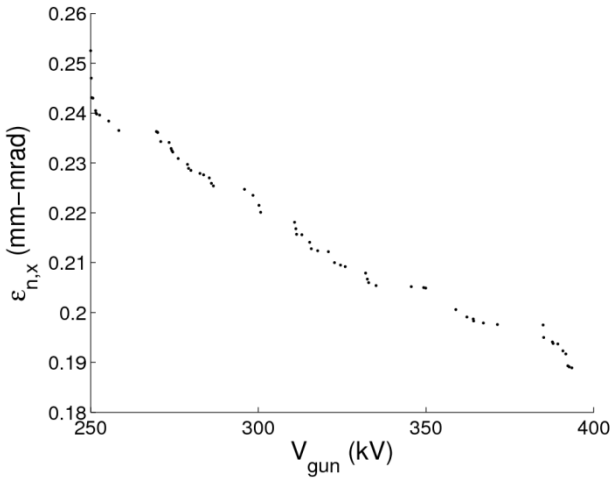

Figure 8: Beam emittance performance for optimized gun geometry at different gun voltages. The bunch charge is 80 pC, and the rms laser pulse duration is 12 ps.

Segmented gun

To a certain extent, it is possible to decouple the two conflicting requirements of a higher gun voltage (a large gap) and a higher E_{cath} (a small gap) by considering a two gap DC gun. Figure 9 illustrates the concept. Such a gun will feature a small (1.5-2 cm) gap with a modest 250 kV voltage followed by a larger gap with uncritical dimension of 5-10 cm with a larger 350-500 kV voltage. This would allow the creation of a high field at the photocathode (>10 MV/m) together with the more optimal overall gun voltage of 600-750 kV. Further investigations about the practicality of this approach are required.

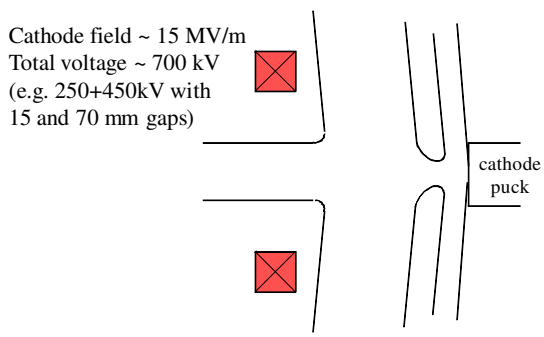

Figure 9: A double-gap DC gun.

CONCLUSION

This paper summarizes the presentations and discussion of DC gun sessions of Working Group 1 at ERL09 Workshop. The superconducting and normal conducting RF guns, drive laser and cathode sessions are summarized in an accompanying paper [57]. The technological challenges presented and discussed at ERL09 will be addressed worldwide to promise a brighter future of ERL light sources. The conveners of WG1 express their appreciation to all the participants and organizers of ERL09 for a fruitful workshop.

ACKNOWLEDGMENTS

This work is supported by the Office of Naval Research, the Joint Technology Office, the Air Force Research Laboratory, USA, the U.S. Night Vision Lab, the Commonwealth of Virginia, by DOE Contract DE-AC05-060R23177, both USA, and Science and Technology Facilities Council, UK, MEXT Quantum Beam Technology Program, JSPS Grants-in-Aid for Scientific Research in Japan (20360424).

REFERENCES

[1] Charles K. Sinclair, "DC photoemission electron guns as ERL sources", Nucl. Inst. and Meth. A 557 (2006) 69

[2] C. K. Sinclair, P. A. Adderley, B. M. Dunham, J. C. Hansknecht, P. Hartmann, M. Poelker, J. S. Price, P. M. Rutt, W. J. Schneider, and M. Steigerwald, "Development of a high average current polarized electron source with long cathode operational lifetime", Phys. Rev. ST Accel. Beams 10 (2007) 023501

[3] C. Hernandez-Garcia, T. Siggins, S. Benson, D. Bullard, H. F. Dylla, K. Jordan, C. Murray, G. R. Neil, M. Shinn, and R. Walker, "A High Average Current DC GaAs Photocathode Gun for ERLs and FELs", PAC05, Knoxville, Tennessee, 2005, p. 3117

[4] Ivan V. Bazarov and Charles K. Sinclair, "Multivariate Optimization of a high brightness dc gun photoinjector", Phys. Rev. ST Accel. Beams 8 (2005) 034202

[5] Florian Loehl, "Synchronization Needs", ERL09, Cornell University, Ithaca, 2009, http://www.lepp.cornell.edu/Events/ERL09/Agenda.html

[6] Uwe Uhmeyer, "KSI's Cross Insulated Core Transformer Technology", Proceedings of the 18th International Symposium on High Energy Spin Physics (SPIN2008), AIP Conf. Proc. 1149, (AIP, New York, 2009), 1099

[7] F. Furuta , T. Nakanishi, S. Okumi, T. Gotou, M. Yamamoto, M. Miyamoto, M. Kuwahara, N. Yamamoto, K. Naniwa, K. Yasui, H. Matsumoto, M. Yoshioka, K. Togawa, "Reduction of field emission dark current for high-field gradient electron gun by using a molybdenum cathode and titanium anode", Nucl. Inst. and Meth. A 538 (2005) 33

[8] B. M. Dunham, C. K. Sinclair, I. V. Bazarov, Y. Li, X. Liu, and K. W. Smolenski, "Performance of a Very High Voltage Photoemission Electron Gun for a High Brightness, High Average Current ERL Injector", PAC07, Albuquerque, New Mexico, 2007, TUPMS021, 1224

[9] A. Burrill and M. Poelker, "ERL07 Working Group 1 Summary: Electron Guns and Injector Designs", ERL07, Daresbury, UK, 2007, 139

[10] M. Poelker, P. Adderley, J. Brittian, J. Clark, J. Grames, J. Hansknecht, J. McCarter, M.L. Stutzman, R. Suleiman, K. Surles-Law, "Status of High Polarization DC High Voltage Gallium Arsenide Photoelectron Guns", PAC07, Albuquerque, New Mexico, 2007, FRXAB01, 3756

[11] C.D. Park, S.M. Chung, Xianghong Liu, and Yulin Li, "Reduction in hydrogen outgassing from stainless steels by a medium-temperature heat treatment", J. Vac. Sci. Tech. A 26 (2008) 1166

[12] H. Kurisu, G. Kimoto, H. Fujii, K. Tanaka, S. Yamamoto, M. Matsuura, K. Ishizawa, T. Nomura, and N. Murashige, "Outgassing Properties of Chemically Polished Titanium Materials", J. Vac. Soc. Jpn. 49, (2006) 254 [in Japanese]

[13] J. Grames, M. Poelker, P. Adderley, J. Brittian, J. Clark, J. Hansknecht, D. Machie, M.L. Stutzman, and K. Surles-Law, "Measurements of Photocathode Operational Lifetime at Beam Currents up to 10 mA using an Improved DC High Voltage GaAs Photogun", Proc. of the 17th Spin Physics Symposium, Kyoto, Japan, 2006, 1037

[14] E. Pozdeyev, "Ion trapping and cathode bombardment by trapped ions in dc photoguns", Phys. Rev. ST Accel. Beams 10 (2007) 083051

[15] J. Grames, P. Adderley, J. Brittian, J. Clark, J. Hansknecht, D. Machie, M. Poelker, E. Pozdeyev, M. Stutzman, K. Surles-Law, "A Biased Anode to Suppress Ion Back-Bombardment in a DC High Voltage Photoelectron Gun", 12th International Workshop on Polarized Ion Sources, Targets and Polarimetry, AIP Conf. Proc. 980, (2007) 110

[16] I.V. Bazarov, B.M. Dunham, C.K. Sinclair, "Maximum achievable beam brightness from photoinjectors", Phys. Rev. Lett. 102 (2009) 104801

[17] K. Togawa, T. Shintake, T. Inagaki, K. Onoe, T. Tanaka, H. Baba, and H. Matsumoto ,"CeB6 electron gun for low-emittance injector", Phys. Rev. ST Accel. Beams 10, (2007) 020703

[18] C.K. Sinclair, "A 500 kV photoemission electron gun for the CEBAF FEL", Nucl. Inst. And Meth. A318 (1992) 410

[19] M. Briedenbach, M. Foss, J. Hodgson, A. Kulikov, A. Odian, G. Putallaz, H. Rogers, R. Schindler, K. Skarpaas, M. Zolotorev, "An inverted-geometry, high voltage polarized electron gun with UHV load lock", Nucl. Inst. and Meth. A350 (1994) 1

[20] C.W. de Jager, V.Ya. Korchagin, B.L. Militsyn, V.N. Osipov, N.H. Papadakis, S.G. Popov, M.J.J. van den Putte, Yu.M. Shatunov, Yu.F. Tokarev, "The Photocathode Gun of The Polarized Electron Source at NIKHEF", The Seventh International Workshop on Polarized Gas Targets and Polarized Beams, AIP Conf. Proc. 421 (AIP, New York, 1998), 483

[21] Tsutomu Nakanishi, "Polarized electron source using NEA-GaAs photocathode", Proc. of LINAC2002, Gyeongju, Korea, 811

[22] N. Nishimori, R. Nagai, R. Hajima, T. Shizuma, E.J. Minehara, "A Thermionic Electron Gun System for the JAERI Superconducting FEL ", EPAC00, Vienna, Austria, 2000, 1672

[23] N. Nishimori, R. Nagai, H. Iijima, Y. Honda, T. Muto, M. Kuriki, M. Yamamoto, S. Okumi, T. Nakanishi, and R. Hajima, "Development of an electron gun for an ERL based light source in Japan", Proceedings of the 18th International Symposium on High Energy Spin Physics (SPIN2008), (Ref. [6]), 1094

[24] R. Hajima et al.,"Design and Fabrication of a 500-kV Photocathode DC Gun for ERL Light Sources", in Proc. of PAC09, Vancouver, Canada, 2009

[25] T. Siggins, C. Sinclair, C. Bohn, D. Bullard, D. Douglas, A. Grippo, J. Gubeli, G.A. Krafft, B. Yunn, "Performance of a DC GaAs photocathode gun for the Jefferson lab FEL", Nucl. Inst. And Meth. A 475, (2001) 549

[26] B. Dunham, Private communication.

[27] C. Hernandez-Garcia, JLab Technical Note JLAB-TN-08-065.

[28] C. Hernandez-Garcia, S.V. Benson, G. Biallas, D. Bullard, P. Evtushenko, K. Jordan, M. Klopf, D. Sexton, C. Tennant, R. Walker, and G. Williams, "DC High Voltage Conditioning of Photoemission Guns at Jefferson Lab FEL", Proceedings of the 18th International Symposium on High Energy Spin Physics (SPIN2008), (Ref. [6]), 1071

[29] J. Francis, SLC Procedural Note FP-238-042-94 (1991)

[30] N. Theodore et.al., "Nitrogen-Implanted Silicon Oxynitride: A Coating for Suppressing Field Emission From Stainless Steel Used in High-Voltage Applications", IEEE Trans. Plasma Sci., 34, 1074 (2006)

[31] R. Alley, H. Aoyagi, J. Clendenin, J. Frisch, C. Garden, E. Hoyt, R. Kirby, L. Klaisner, A. Kulikov, R. Miller, G. Mulhollan, C. Prescott, P. Saez, D. Schultz, H. Tang, J. Turner, K. Witte, M. Woods, A.D. Yeremian, M. Zolotorev, "The Stanford linear accelerator polarized electron source" Nucl. Instr. and Meth. A 365 (1995) 1

[32] Fumio Watanabe, "Extremely low-outgassing material: 0.2% beryllium copper alloy", J. Vac. Sci. Technol. A 22, (2004) 181

[33] K. Saito, S. Inayoshi, Y. Yang, and S. Tsukahara, "TiN thin film on stainless steel for extremely high vacuum material", J. Vac. Sci. Technol. A 13 (1995) 556

[34] H. Akimichi and M. Hirata, "Generation and pressure measurement of extremely high vacuum (XHV) using a TiN coated chamber", Metrologia 42 (2005) S184

[35] T. Kikuchi, N. Ohsako and Y. Hayashi, "Capability of Obtaining Extreme High Vacuum by Commercial G-M refrigerator-Cooled Cryopump", Vacuum 41 (1990) 1941

[36] Hiroyuki Yamakawa, "Development and performance of bakeable cryopumps for extreme high vacuum", Vacuum 44 (1993) 675

[37] M.L. Stutzman, P. Adderley, J. Brittian, J. Clark, J. Grames, J. Hansknecht, G.R. Myneni, M. Poelker, "Characterization of the CEBAF 100 kV DC GaAs photoelectron gun vacuum system", Nucl. Instr. and Meth. A 574 (2007) 213

[38] B.M. Dunham, Ph.D. thesis, University of Illinois at Urbana-Champaign (1993)

[39] G.D. Cates, V.W. Hughes, R. Michaels, H.R. Schaefer, T.J. Gay, M.S. Lubell, R. Wilson, G.W. Dodson, K.A. Dow, S.B. Kowalski, K. Isakovich, K.S. Kumar, M.E. Schulze, P.A. Souder, D.H. Kimet, "The BATES polarized electron source", Nucl. Inst. and Meth. A278 (1989) 293

[40] L.B. Jones, S.P. Jamison, Y.M. Saveliev, K.J. Middleman and S.L. Smith, "Status of the ALICE Energy-Recovery Linac", Proceedings of the 18th International Symposium on High Energy Spin Physics (SPIN2008), (Ref. [6]), 1084

[41] R.E. Kirby, G.J. Collet, K. Skarpaas, "An In-Situ Photocathode Loading System for the SLC Polarized Electron Gun", Proc. of PAC'93, 3030

[42] K. Aulenbacher, Ch. Nachtigall, H.G. Andresen, J. Bermuth, Th. Dombo, P. Drescher, H. Euteneuer, H. Fischer, D.v. Harrach, P. Hartmann, J. Hoffmann, P. Jennewein, K.H. Kaiser, S. Kobis, H.J. Kreidel, J. Langbein, M. Petri, S. Plutzer, E. Reichert, M. Schemies, H.-J. Schope, K.-H. Steffens, M. Steigerwald, H. Trautner, Th. Weis, "The MAMI source of polarized electrons", Nucl. Inst. and Meth. A391 (1997) 498

[43] M.J.J. van den Putte, C.W. De Jager, S.G. Konstantinov *et al.*, "The Polarized Electron

Source at NIKHEF", Seventh International Workshop on Polarized Gas Targets and Polarized Beams, (Ref. [20]), 260
[44] W.J. Schneider, P. Adderley, J. Clark, A. Day, B. Dunham, J. Hansknecht, P. Hartmann, J. Hogan, R. Kazimi, D. Machie, M. Poelker, J.S. Price, P.M. Rutt, K. Ryan, C.K. Sinclair and M. Steigerwald, "A load-locked gun for the Jefferson Lab Polarized Injector", PAC99, New York, 1999, 1991
[45] B.L. Militsyn, I. Burrows, R.J. Cash, B.D. Fell, L.B. Jones, J.W. McKenzie, K.J. Middleman, S.N. Kosolobov, H.E. Scheibler, A.S. Terekhov, "Design of an upgrade to the ALICE photocathode electron gun", EPAC08, Genoa, Italy, 235
[46] S. Pastuszka, A.S. Terekhov, A. Wolf, "'Stable to unstable' transition in the (Cs, O) activation layer on GaAs (100) surfaces with negative electron affinity in extremely high vacuum", Applied Surface Science 99, (1996) 361
[47] D.A. Orlov, C. Krantz, A. Wolf *et al.*, "Long term operation of high quantum efficiency GaAs(Cs,O) photocathodes using multiple re-cleaning by atomic hydrogen", J. App. Phys. In print.
[48] J. Grames, P. Adderley, J. Brittian, D. Charles, J. Clark, J. Hansknecht, M. Poelker, M. Stutzman, K. Surles-Law, "Ion Back-Bombardment of GaAs Photocathodes Inside DC High Voltage Electron Guns", PAC05, Knoxville, Tennessee, (2005) 2875
[49] K. Aulenbacher et.al., "Status of the polarized source at MAMI", 15th International Spin Physics Symposium, AIP Conf. Proc. 675, (2002) 1088
[50] H2 ionization cross section plot
[51] K. Aulenbacher et al., SLAC Report 432 (1993)
[52] Fay Hannon, private communication
[53] I.V. Bazarov, B.M. Dunham, Y. Li, X. Liu, D.G. Ouzounov, C.K. Sinclair, F. Hannon, T. Miyajima, "Thermal emittance and response time measurements of negative electron affinity photocathodes", J. Appl. Phys., 103 (2008) 054901
[54] I.V. Bazarov, B.M. Dunham, C. Gulliford, Y. Li, X. Liu, C.K. Sinclair, K. Soong, "Benchmarking of 3D space charge codes using direct phase space measurements from photoemission high voltage DC gun", Phys. Rev. ST Accel. Beams 11 (2008) 100703
[55] P.G. Slade, The vacuum interrupter: theory, design, and application, CRC Press, 2008
[56] M. Lakshmanan et al., "Geometry Optimization of DC and SRF Guns to Maximize Beam Brightness", these proceedings
[57] J.W. Lewellen, H. Bluem, A. Burrill, T.L. Grimm, T. Kamps, R. Legg, K. Liu, T. Rao, J. Smedley, J. Teichert, S. Zhang, "ERL 2009 WG1 Summary Paper: Drive Lasers and RF GUn operation and challenges", these proceedings

ERL 2009 WG1 SUMMARY PAPER: DRIVE LASERS AND RF GUN OPERATION AND CHALLENGES*

J.W. Lewellen[1], H. Bluem[2], A. Burrill[3], T.L. Grimm[4], T. Kamps[5], R. Legg[6], K. Liu[7], T. Rao[3], J. Smedley[3], J. Teichert[8], S. Zhang[9]
[1] Naval Postgraduate School, Monterey, CA 93943, USA
[2] Advanced Energy Systems, Inc., Princeton, NJ 08824, USA
[3] Brookhaven National Laboratory, Upton, NY 11973, USA
[4] Niowave, Inc., Lansing, MI 48906, USA
[5] Helmholtz-Zentrum Berlin, 14109 Berlin, Germany
[6] University of Wisconsin-Madison, Stoughton, WI 53589, USA
[7] Peking University, Beijing 100871, People's Republic of China
[8] Forschungszentrum Dresden-Rossendorf, 01314 Dresden, Germany
[9] Thomas Jefferson National Accelerator Facility, Newport News, VA 23606, USA

Abstract

Working Group I of the 2009 Energy Recovery Linac Workshop focused on high-brightness, high-power electron beam sources for energy recovery linacs (ERLs), and relevant technology such as development of drive lasers. The WG1 summary paper was broken into two parts: DC guns and loadlocks; and RF guns and drive lasers. This was done both to retain more manageable paper sizes, and because SRF guns are in an earlier stage of development than DC guns. This paper describes the advances, concepts, and thoughts for the latter topics presented at the workshop.

There are many challenges to the successful operation of SRF guns as high-brightness, high-average-current beam sources. These combine the set of challenges for high-current SRF cavities (fabrication, cleaning and processing, HOM extraction, etc.), with challenges for high-average-current photocathode sources (photocathode fabrication, quantum efficiency and lifetime, drive laser technology, etc.). New challenges also arise from this combination, such as the requirement for having removable cathodes in an SRF cavity. Practical approaches have been, and are currently being, found to address the problems, and the base of knowledge and experience continues to grow.

Alternate ideas are also beginning to make inroads. Hybrid DC-SRF guns, pioneered by Peking University, offer promise for combining the best features of both technologies. Quarter-wave SRF cavities offer compact size for a given frequency, potentially easier fabrication than elliptical cells, and very high transit-time factors for quasi-DC operation. Also, the use of normal-conducting cavities, usually dismissed out of hand due to the required RF power consumption, may become practical with advanced cavity designs.

This paper summarizes the state-of-the-art of drive lasers, cathode development and RF gun-based injectors for ERL beam sources The focus in the field has been on DC and SRF guns to date, but interesting approaches for hybrid DC/SRF guns and normal-conducting RF guns are also presented. The paper concludes with discussions of operational issues and concerns, technical issues related to beam source realization, and future concepts.

SUMMARY ON ERL DRIVE LASERS

S. Zhang and T. Rao

CURRENT STATUS

Significant progress on ERL drive lasers has been seen since ERL07. The status of each drive laser is summarized below based on the reports given by different labs during this workshop (specification details are given in Table 1):

- JLab has replaced its flashlamp-pumped drive laser and commissioned a 25W/532nm diode-pumped MOPA system in 2008. The new drive laser has been driving the JLab ERL FEL with adjustable CW micro-pulse frequency from 75MHz down to below 0.5MHz. The macro-pulse width and frequency are also adjustable up to 1ms/60Hz (limited to 1kHz) for routine machine setup. The system shows better amplitude and temporal stability. Unexpected high degree of phase sensitivity from laser oscillator was observed and still remains a primary concern, although considerable effort has been made to suppress the phase noise. A pulse stacker was also installed to change the laser pulse length and shape [1].
- Daresbury Laboratory's 5W/532nm drive laser was commissioned in 2006 and is running for ERL machine beam operation. The laser system has a 0.2% duty cycle with a fixed 81.25MHz micro-pulse frequency and up to 100us/20Hz macro-pulse structure. An issue of temperature instability has arisen from corrosion inside the cooling circuit. This has caused problems in maintaining the pump diode temperature correctly and stably, resulting in longer pulses and reduced SHG efficiency [2].

Table 1: Summary of Drive Laser Specifications

Lab	JLab	Daresbury	Cornell	BNL
Configuration	MOPA	MOPA	MOPA	MOPA
Gain medium	Nd:YVO_4	Nd:YVO_4	Yb-fiber	Nd:YVO_4
Wavelength(nm)	532 (SHG)	532(SHG)	520(SHG)	532(SHG),355(THG)
Pulse (ps)	20, 50	7, 13, 28	2, 30~40	5~12
Power (W)	25	5	15	10 @ 532, 5 @ 355
Max pulse energy (nJ)	300(75MHz) 2000(2MHz)	60	12	500 (10 MHz)
MicroPulse Freq.(MHz)	Variable SMP[1] ~75CW	81.25CW	1300CW	10MHz CW
MacroPulse (μs) &Freq.	0.2~1000 SS[2]~1kHz	SMP to 100 20Hz	0.1~10 1kHz	SMP~10 SS~100kHz
Pulse contrast	$7x10^4$	$>10^6$ at 532 nm	~ 10^6	$3x10^5$
Amplitude stability (rms)	<1%	~1%	<1%	<1%
Phase stability	0.6ps (rms) (10Hz~40MHz)	<0.65ps (0.1 Hz – 1 MHz)	<1ps	0.5 ps (10 Hz-10 MHz)
Pointing Stability(urad)	20		5 (w. Stabilizer)	2-3
Spatial Shape	Truncated Gaussian	Truncated Gaussian (Gaussian + pinhole)	Top-hat (BS[3])	Planned for: Top-hat (BS)
Temporal shape	S. Gaussian (PS[4])	Quasi-Top-hat (PS)	Quasi-Top-hat (PS)	Planned for: Top-hat (PS)
Potential bunch charge	nC (1% QE)	80 pC (1% QE)	77pC	15 nC (10 %QE)
Achiv. bunch charge(pC)	270 135(routine operation)	~130	10	Pending test
Operation Status	ERL	ERL	Injector	Installed, pending cathode illumination

[1] SMP:single-micro-pulse [2]SS:single-shot [3]BS:beam shaper [4]PS:pulse stacker

- Cornell's drive laser is a 1040nm all-fiber system with 1.3GHz fixed micro-pulse frequency. Temporal shaping by pulse stackers was demonstrated and produced quasi-flat-top electron bunches [3]. A pointing stabilizer was tested and showed improved pointing stability. 15W SHG has been achieved, but attempts to generate higher power were hindered by poor power stability of pump-diodes and fiber holder heating issue. A previously-built 50MHz fiber laser is being resumed for intended emittance measurement [4].
- BNL has received a 5W/355nm/10MHz laser from Lumera as the first step to demonstrate nC charge on future ERL accelerator. The laser installation is underway and the test with cathode is expected in year of 2010. Assuming a 10% QE as demonstrated in the laboratory, this laser with CsK_2Sb cathode can deliver up to 150 mA average current and up to 15 nC/pulse. The pulse selection system allows the selection of arbitrary number of pulses from the pulse train with up to 100kHz repetition rate and CW operation at 10MHz. Flat-top laser distributions have been obtained with a commercial spatial beam shaper and multi-crystal pulse stacker at 532nm on a different laser with similar parameters [5].

DISCUSSION AND PROSPECTS

Laser Power and Pulse Control

With the rapid development of advanced laser technology, the laser power needed for 100s of mA electron beam is not a limiting factor any more. But it still requires significant effort to make any commercial laser a robust ERL drive laser with full control of variable macro/micro pulse structures and high pulse contrast, which are crucial for tuning ERL machines, especially in the 10~100s MHz range. In addition, as showed by JLab's test, proper cooling of GaAs cathodes is necessary in order to alleviate the serious temperature rise induced by laser power deposition into the cathode wafer [1]. This may become less significant with multi-alkali cathodes deposited on metal substrates, especially in an SRF gun environment. Further investigation into the issue is necessary.

Stability

The amplitude stability of all available candidate lasers appears satisfactory. Additional stabilizers may be needed for XFEL machines for less than 10urad pointing stability. A question about the phase stability of the SESAM-mode-locked lasers was raised by JLab, based on their experience. This may need broader observation to compare.

Laser Architecture

The laser architecture is of great importance in case of high power systems (10s~100s of Watts). The MOPA configuration seems to be the preferred choice for such ERL drive lasers which demand both short pulse and high power. The idea of combining fiber lasers as seeds and bulk gain materials as power amplifiers will likely be a feasible approach that takes the advantages of both while avoiding their drawbacks.

Pulse Shape and Duration

Both experiments and simulations have shown that uniform laser distributions in both time and space help to reduce the emittance of electron bunches. Cornell's experiment with pulse stacker shows good agreement between the longitudinal profiles of the laser pulses and electron bunches [3]. Spatial beam shapers are well studied and commercially available, but also very sensitive to laser parameters and alignment. Generation of electron bunches with ellipsoidal distributions via space-charge blowout has been demonstrated at low charge of 15pC [6]. A method to generate ellipsoidal optical pulses was experimentally demonstrated [7], but needs to be tested with a gun and photocathode for verification. Finally, it is worth mentioning that, in addition to the laser pulse shape, the actual pulse duration also plays an important part in the performance of an ERL machine, based on simulation and JLab's experience [1].

PHOTOCATHODES FOR HIGH-CURRENT SRF GUNS

J. Smedley

INTRODUCTION

For ERLs operating up to 1 mA average current, several cathode options are available. As described elsewhere, using metallic superconductors as cathodes is reasonable in this regime [8,9]; lead has been shown to be significantly superior to niobium [10]. Plating the cathode region of the injector back wall with lead has little impact on the operating gradient that can be achieved – peak gradients of 40 MV/m have been demonstrated in cavities with lead cathodes [11,12]. Another potential cathode option for the sub-mA regime is Nb plated with 5nm of CsBr. CsBr has been demonstrated to provide a x50 improvement to copper cathodes [13], and a coating of 5 nm in the cathode region is expected to have minimal impact on the cavity RF performance. Although this cathode has yet to be tested in an injector, preliminary measurements by J. Maldonado achieved a QE of $5x10^{-4}$ at 260 nm. This represents an improvement of x800 compared to the niobium substrate, and a factor of four compared to lead at the same wavelength. On a copper substrate, this cathode has been shown to be resistant to brief air exposure, making it far more rugged than standard semiconductor cathodes.

For operating currents up to 10 mA, Cs_2Te is an attractive option. For operating currents of 100mA and above, three cathode technologies are being investigated in the community: III-V semiconductors with negative electron affinity (principally Cs:GaAs), alkali antimonides and diamond amplified photocathodes. The first two cathodes are "established" technologies both for accelerators [14] and in the broader photocathode community, while the diamond amplifier is an ongoing research project [15,16].

BI-ALKALI EXPERIENCE AT BNL

The alkali antimonides offer high QE at visible wavelengths, with vacuum requirements that are more forgiving than GaAs. In some applications [17], alkali antimonide cathodes are used at atmospheric pressure (of argon and methane)! For the BNL ERL, the primary cathode will be K_2CsSb. This cathode is created by sequential deposition on a warm (150C) substrate. Copper and stainless steel (SS) have been investigated as substrates; SS is clearly superior. Antimony is deposited first, with a typical thickness of 20nm. Potassium is deposited second, with a target thickness twice that used for Sb. Finally cesium is added, while monitoring the QE at 532nm. The cathode is complete when the QE stops rising; at this point Cs deposition is halted and the substrate is cooled to room temperature. Figure 1 shows typical response curves for three cathodes on SS substrates, measured with a lamp source and monochromator. For cathode 3, a lower substrate

temperature during deposition was attempted, resulting in a marginal decrease in QE. For cathodes 2&4, the QE was measured with a 532nm CW laser, resulting in close agreement with the lamp values (even with six orders of magnitude more power).

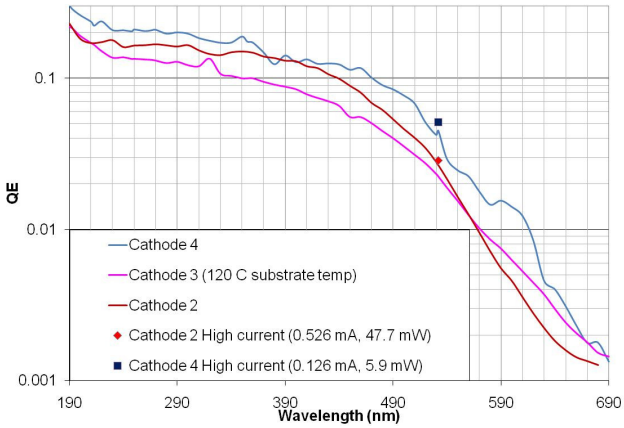

Figure 1: K_2CsSb spectral response.

The dark lifetime of the cathode in the deposition chamber is effectively unlimited – no change in the QE was observed after 40 days of storage at 0.1 nTorr vacuum. The decay of the QE in the deposition chamber was measured (figure 2) under high current density (1.3 mA/mm^2); this is the design average current density for the BNL ERL cathode. To achieve this current density, a CW green laser was focused to an 80 micron FWHM spot on the cathode. In this test, the emitted electrons are dumped into an anode 25 mm from the cathode. This lifetime is therefore a worst case, at least with respect to electron stimulated desorption (ESD). The decay is likely dominated by ESD, as the lifetime depends on the anode bias; no decay was observed for bias voltages under 1keV.

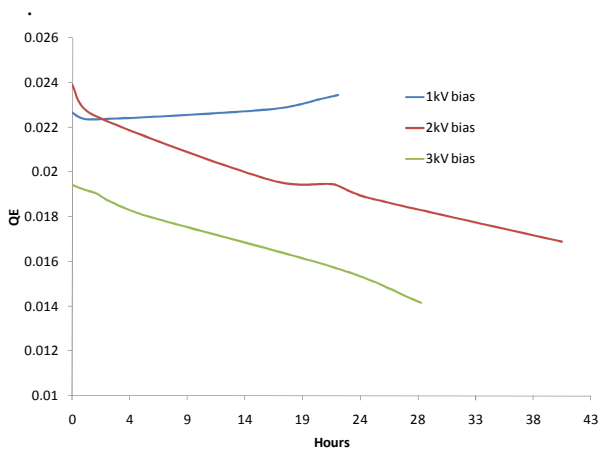

Figure 2: QE decay w/ 1.3 mA/mm^2 current density.

OUTSTANDING ISSUES

Photocathode development for high current injectors is a vibrant area of investigation, and several avenues exist for further work. One test that is sorely lacking is an apples-to-apples comparison of Cs:GaAs and an alkali antimonide (perhaps K_2CsSb) in an injector. Both cathodes have good QE in the green; the vacuum in current DC injectors using GaAs cathodes is easily sufficient for K_2CsSb; thus this seems to be a test that is well within the capabilities of the community.

More generally, continued development of cathode materials is critical as ERLs push to higher average current. Use of the materials analysis tools (UPS/XPS, LEED/XRD, etc.) available at the synchrotrons and nanocenters worldwide will likely produce better (and better understood) cathodes.

SUPERCONDUCTING ELLIPTICAL RF GUNS

A. Burrill and T. Kamps

OVERVIEW

The development of elliptical SRF injectors, pioneered at Wuppertal University in 1991 [18], continues to make strong advances with several interesting projects currently underway. Three laboratories, Brookhaven National Lab (BNL), Forschungszentrum Dresden-Rossendorf (FZD) and Helmhotz Zentrum Berlin (HZB), presented material on elliptical SRF injectors designed for use in ERLs, and each has taken a unique approach to solving the problems associated with providing a small emittance, short electron bunch to the ERL each system is driving. This section will highlight the material presented and try to gauge when each system will see both first beam, and first use in an ERL. This should also serve as a mile-marker for subsequent workshops in order to gauge the advances being realized with this technology.

FZD

The Wuppertal cavity design was subsequently fabricated and tested by D. Janssen et al. in 2000 & 2002 [19,20]. It was a ½ cell 1.3 GHz Tesla style gun with a non-resonant RF choke cavity which served to isolate the normal conducting cathode, both thermally and electrically, from the SRF cavity. This cavity made use of a Cs_2Te photocathode irradiated by a UV laser operating at 263 nm with 5 ps pulses delivered at 26 MHz, and achieved a maximum bunch charge of 20 pC. The system demonstrated stable operation over 7 weeks at 4.2K with a steady Q of 2.5x10^8.

This work led to the design of the current 3 ½ cell SRF injector, shown in Figure 3, designed for use at ELBE (**E**lectron **L**inear accelerator with high **B**rilliance and low **E**mittance) and the focus of the FZD SRF injector work [21]. This gun is a 3½ cell 1.3 GHz Tesla style design utilizing the non-resonant RF choke for cathode insertion. This system has been designed to operate utilizing a Cs_2Te photocathode and is designed for a variety of operating conditions, summarized in Table 2. To date the cavity has produced a 2.1 MeV electron beam with a maximum bunch charge of 200 pC and a transverse normalized emittance of 3 μm at 80 pC. Future plans include connecting the gun to the ELBE accelerator at the end of 2009, as well as the fabrication of 2 new injectors

Table 2: Elliptical cavity gun performance specifications

Facility		**FZD**		**HZB**		**BNL**	
Mode		ELBE	High Charge	HoBiCaT/ Stage 1	B*ERL*inPro/ Stage 2	High Current	High Charge
Electron Energy	MeV	9.5		1.5		2.5	3
RF Frequency	MHz	1300		1300		703	
Design Peak Field	MV/m	50		40		30	35
Achieved Peak Field	MV/m	13.5		45			
Bunch Charge	pC	77	1000	77-1000	77	1400	5000
Repetition rate	MHz	13	0.5	0.03	1300	352	9.38
Laser pulse	ps	4	15	12	15	20	30
Laser wavelength	nm	262		258	355/532	355	
Cathode		Cs_2Te		Pb	CsK_2Sb	CsK_2Sb	
Transverse rms emittance	µm	1	2.5	3	1	2.3	4.8
Average current	mA	1	0.5	$30 \cdot 10^{-3}$	100	500	50
Peak current	A	20	67	6	5	70	166

of similar design that should realize the full 9.5 MeV beam in 2010.

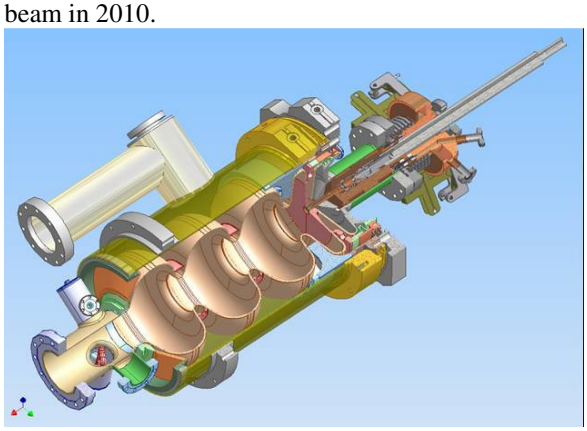

Figure 3. The FZD 3 1/2 cell 1.3 GHz photoinjector.

HZB

The work reported by HZB takes a very different approach to development of an SRF injector suitable for use in an ERL. The approach is staged and the first stage of the development aims at the design of an all SC high brightness gun. This gun, shown in Figure 4, is a 1.3 GHz 1½ cell injector where the back wall of the photoinjector has a small area coated with lead, a superconductor, that is used as the photocathode [9,22]. The goal of this program is to build a robust injector capable of operating at 1 mA average current, 77 pC bunch charge, with a 1 µm emittance. By utilizing the back wall as the photocathode the additional complications associated with introducing a normal conducting photocathode are avoided. This idea grew from the BNL design of a 1.3 GHz ½ cell injector which used the bare Nb surface as the photocathode, however Pb provides ~2 orders of magnitude improvement in quantum efficiency compared to Nb at the same wavelength [10]. To date the gun has been tested at Jefferson Lab in the vertical test area (VTA) and has reached 45 MV/m peak field with a Q of 1.0×10^{10}. Separately the QE of Pb has been measured to be ~0.05% at 258 nm, the desired operating wavelength of the HZB program.

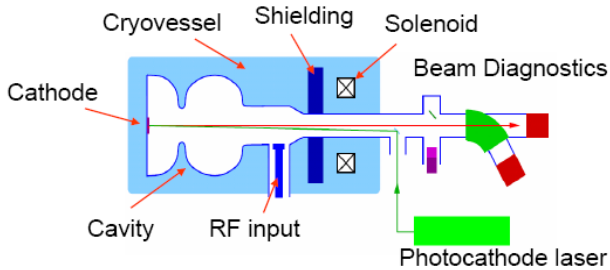

Figure 4. The HZB 1 1/2 cell 1.3 GHz photoinjector layout schematic.

This program is designed as a test-bed for technologies, called B*ERL*inPro [23], for a full scale ERL-based next generation light source. For emittance compensation a superconducting solenoid with NbTi coils will be placed close to the SRF cavity inside the cryovessel. The solenoid field shape and decay are important, especially in the direction of the SRF cavity. Therefore a design with compensation coils or a special flux return yoke is foreseen. The photocathode drive laser is designed to deliver UV laser pulses of a few ps length with 10 µJ energy per pulse, enough to achieve some pC to 1 nC bunch charge for beam dynamics studies in the space-charge dominated regime.

The first milestone of the project, planned for spring 2010, is to perform RF measurements of the interaction between the SRF cavity and solenoid in the HoBiCaT cryovessel. In the next step the drive laser and beam diagnostic devices will be added for first beam operation in autumn 2010.

The testing sequence will then continue with measurement of beam from the injector in the fall of 2010. For the next stage a SC gun cavity with NC cathode insert is foreseen. Then a CsK2Sb cathode is required to reach also high brightness at high average current.

BNL

The BNL SRF injector program began with the aforementioned 1.3 GHz ½ cell injector and has subsequently grown to include the use of a GaAs photocathode in a 1.3 GHz plug gun [24] as well as the design of a novel quarter wavelength choke joint used to isolate the photocathode from the cavity [25]. The main thrust of the BNL ERL injector program is aimed at the testing of a 703 MHz ½ cell injector designed to operate with a CsK_2Sb photocathode illuminated at 355 nm and delivering between 50 and 500 mA average current [26]. The gun, shown in Figure 5, is in the final stages of fabrication and should begin vertical testing in late 2009 with first beam tests in late 2010. The cavity is designed to deliver a 2.5 MeV electron beam to the ERL with 1.4 nC bunches and a normalize emittance of 2.3 μm. The full set of beam parameters are listed in Table 2, and similar to the other two guns discussed includes several different operating regimes in order to fully probe the applicability of this design.

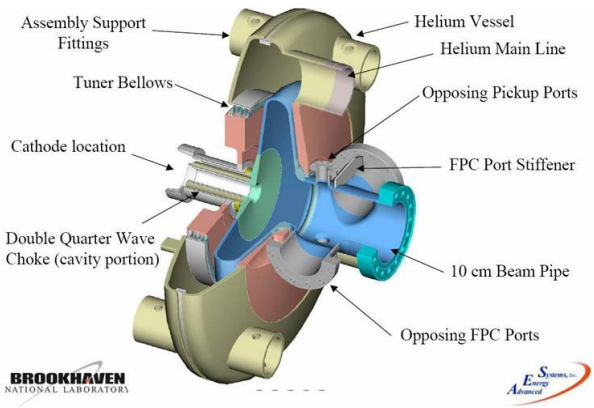

Figure 5. The overview of the BNL 703 MHz SRF injector with the quarter wave choke joint for cathode insertion.

QUARTER WAVE SUPERCONDUCTING RF GUNS

T.L. Grimm

Superconducting RF guns and accelerating cavities for electrons have typically coupled cylindrical waveguide TM010 modes together, while superconducting RF cavities for low energy heavy ions have used coaxial type cavities with TEM modes [27,28]. Recently, coaxial quarter wave cavities have been proposed for electrons due to several potential advantages. The status of quarter wave superconducting RF gun development is reviewed here.

The quarter wave cavity is much more compact than the cylindrical waveguide cavities, thereby allowing operation at much lower frequencies of 100-500 MHz. Figure 6 shows three quarter wave guns under development at Brookhaven National Lab (BNL), University of Wisconsin (UW) and Naval Postgraduate School (NPS) along with their RF frequency and energy gain, respectively. The primary advantages of a quarter wave structure are:

- Cryoplant operation at 4.2-4.5 K
- Small accelerating gap so electric field is effectively DC
- Less RF current on the cathode
- High power, inexpensive CW sources
- Reduced sensitivity to DC magnetic fields
- Improved photocathode lifetime

The compactness of the quarter wave gun reduces the electromagnetic performance compared to traditional cylindrical waveguide cavities at a given frequency, but due to operation at lower frequency the degradation is more than offset. Bulk niobium cavities have demonstrated peak surface fields on the niobium of 100 MV/m and 200 mT at 1.8 K. Typical design levels of half these values are conservatively chosen for a high reliability system at temperatures up to 4.5 K. Therefore, cathode fields around 50 MV/m are possible with extracted electron beam energies of 1 MeV or higher in CW applications. The resulting gap is small compared to an RF period so the fields are effectively electrostatic which improves beam dynamics. Multipacting has been shown to not be a critical issue in these structures as long as good processing procedures and operating vacuum levels are maintained.

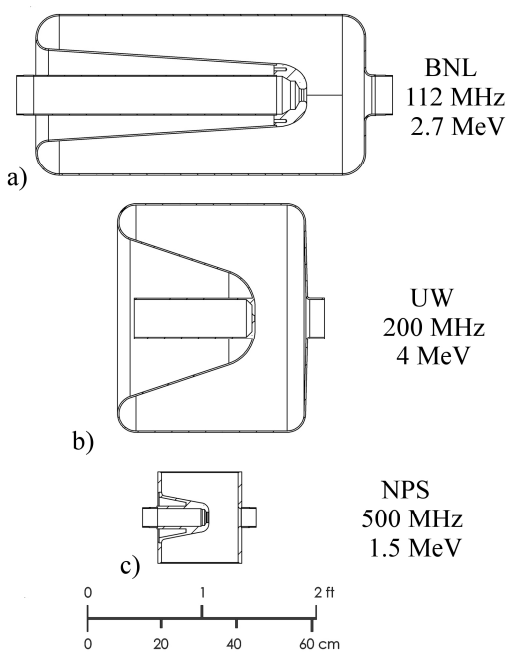

Figure 6. Quarter wave superconducting RF guns under development at: a) BNL, b) UW and c) NPS.

The cathode is usually placed at the end of the inner conductor where the electric fields are largest. Since the amount of charge or current flowing on and off the

cathode is reduced, the cathode can be electrically and mechanically isolated. This allows operation of cathodes at cryogenic through room temperature. Figure 7 shows a Superfish simulation of the NPS gun with the cathode slightly recessed to give a Pierce like geometry with electric field focusing at the cathode.

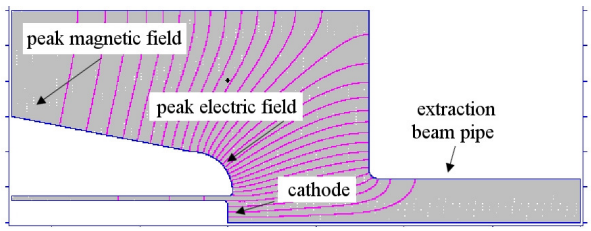

Figure 7. Electric field lines of the 500 MHz NPS quarter wave gun.

Due to cryogenic pumping and cleanroom processing of the cavity, vacuum levels similar to the DC guns are possible. Also, since the electric field in the quarter wave gun is time varying, the cathode damage from ionization along the electron beam trajectory and the subsequent high energy ion back bombardment should be greatly reduced, thereby increasing photocathode lifetime.

A superconducting solenoid can be placed adjacent to the cavity for focusing and emittance compensation. Simulations of all three guns presented here have shown that nC bunches can be generated with the very high brightness necessary for applications such as FELs and high energy electron cooling.

Development of the NPS gun is the most advanced so its design will be presented to show the general characteristics of quarter wave guns. Figure 8 shows the NPS gun cryomodule without the cathode assembly or the axial power coupler.

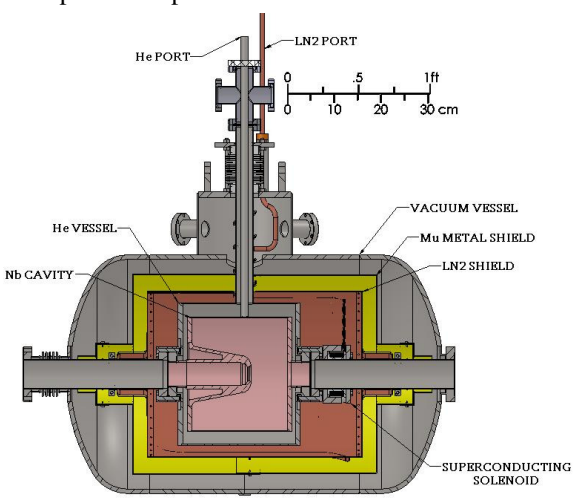

Figure 8. NPS 500 MHz superconducting gun cryomodule

The niobium quarter wave cavity is surrounded by a stainless steel helium vessel to maintain cryogenic temperatures. The niobium-titanium solenoid is on the beamline and has magnetic shielding. The gun cavity and solenoid are surrounded by a liquid nitrogen shield and multi-layer insulation. Finally, a mu-metal shield and low carbon steel vacuum vessel surround the entire system. The insulating vacuum is isolated from the beamline vacuum which is hermetically sealed after processing in the cleanroom.

The cathode assembly and load lock system are attached on the inner conductor side of the quarter wave gun. The power coupler is inserted axially down the extraction beam line to reduce any dipole kicks and to couple strongly to dangerous higher order modes.

Initial demonstration tests and experimental results are anticipated in 2010 for these quarter wave guns. Future developments include coupling the quarter wave cavity to additional cells, high power input couplers with higher order mode extraction, and cathode research with photo, thermionic, field emission and secondary electron emitters. Also the use of multiple modes and frequency operation for focusing and bunch length control can be explored.

HYBRID DC-SRF GUN

K. Liu

The DC-SRF (or SC) photocathode injector developed by Peking University is one of the new candidate low emittance, high brightness electron beam sources. This new design, which integrates a Pierce DC gun and a superconducting cavity, was first proposed by Peking University in 2001 [29]. It has been preliminary demonstrated by the beam experiments with a prototype including a Pierce gun and a 1.5 cell cavity. Energy gain of 1.1MeV was obtained at 4.4 K [30].

To meet the requirement of the ERL-based FEL program at Peking University, an upgraded DC-SRF injector with a 100kV Pierce gun and a 3.5 cell superconducting cavity was designed and manufactured. (Figure 9). The design acceleration gradient, bunch charge, repetition rate and emittance are 13MV/m, 100pC, 26MHz and 1.2 μm respectively [31].

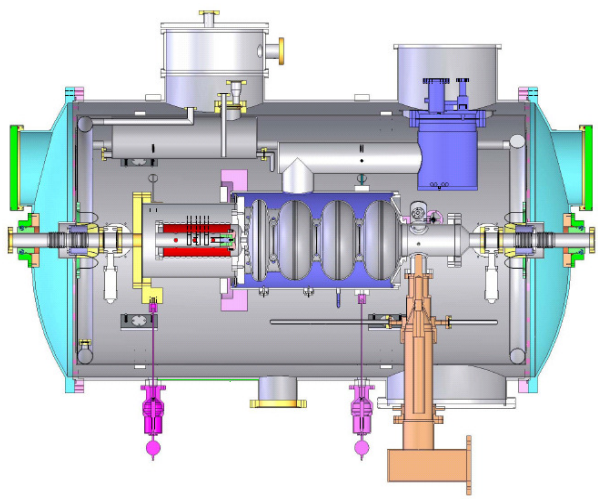

Figure 9. Schematic of 3+1/2 cavity DC-SRF injector

The vertical test of the 3.5 cell cavity, made of large grain niobium, has been carried out at the Jefferson Lab by Dr. Rongli Geng. The initial result was 7MV/m, limited by field emission in the half cell. After heat treatment at 800°C and BCP, the acceleration gradient reached 23.4MV/m and the Q slope is not obvious, as shown in Figure 10. Manufacture of the cryostat, including magnetic shielding of high μ iron, the cavity tuning system, RF power input coupler, liquid helium vessel, liquid nitrogen shielding and supporting components have been finished and the commissioning of the upgraded 3.5 cell DC-SRF photo-injector will be started soon.

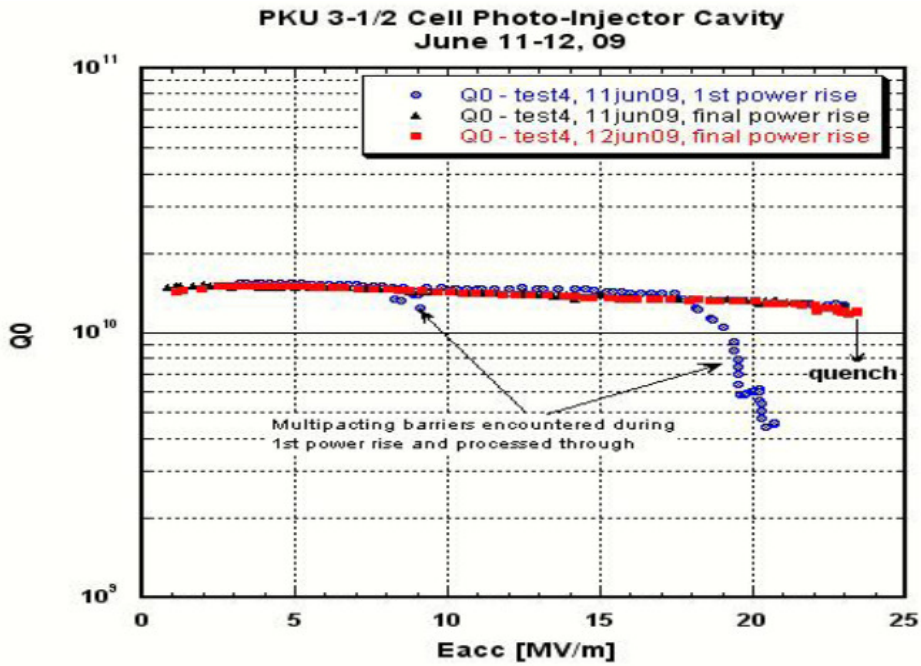

Figure 10. Vertical test result of 3.5 cell large grain Nb cavity

NORMAL-CONDUCTING RF GUN DESIGN ALTERNATIVES

H. Bluem

INTRODUCTION

Normal-conducting Radio Frequency (NCRF) photocathode guns have been very successful in producing low emittance beams in pulsed, high-gradient, low duty-factor operation. For high duty-factor or CW operation, wall losses quickly become the limiting factor, leading to lower accelerating gradients. The problem becomes one of optimizing both the overall losses for a given cathode surface electric field as well as reducing the peak surface losses at local hot-spots. For conventional copper accelerating cavities, the most efficient design is a re-entrant shape which has a high shunt impedance and reasonably evenly distributed wall losses. This shape has tapered nose cones on either side of the interaction gap. The taper is important to spread the wall currents through a larger surface area to improve efficiency and manage the local heat load.

Applying a re-entrant geometry to an NCRF gun can significantly improve the efficiency and allow a higher cathode gradient than would be possible with a pillbox design at the same frequency.

NORMAL CONDUCTING GUNS

The LUX photoinjector [32,33] project sought to develop a multicell photoinjector using a re-entrant design for the cathode cell for a 5% duty factor at 1.3 GHz. However, ERLs require CW electron beams meaning a CW RF gun is required.

To further increase the RF efficiency, one can also reduce the RF frequency. This approach is being considered at BNL [34] as a backup photoinjector to the SRF gun. A mildly re-entrant gun operating at 144 MHz has been designed with a peak cathode field of 8.1 MV/m. Another very low frequency gun design is being pursued at LBNL [35]. This design is strongly re-entrant but only on one side with a very small gap for quasi-DC fields with an operating frequency less than 100 MHz.

One can also achieve the desired results at higher RF frequencies for better compatibility with ERLs [36]. A 1.3 GHz re-entrant gun was designed to serve as a prototype of the concept. Scaling to lower frequency such as 700 MHz should improve the thermal performance. The goal was to limit stress levels to less than 7300 psi in the copper body of the gun. Simulations showed that a cathode field level of 23 MV/m can be supported allowing a transverse emittance less than 1 μm to be achieved. The stress contours at 23 MV/m peak cathode field are shown in Figure 11.

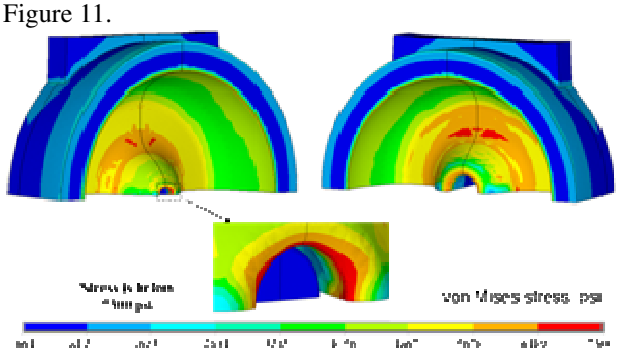

Figure 11: Stress contours on the cavity surface.

Since copper has a non-linear stress-strain curve at low strains, below 0.2%, inelastic analysis was performed to look at more realistic strains and to determine expected frequency shifts of the gun due to operating temperature, coolant pressure and ambient pressure. This analysis shows that the frequency shift at operating temperature is -350 kHz and changes a small amount after each cycle. The results indicate that the frequency shift is an additional -518 Hz after five cycles and -650 Hz after 9 cycles. Looking at the local change in frequency shift, one obtains -50 Hz/cycle at 5 cycles and -20 Hz/cycle at 9 cycles. The change in frequency shift is decreasing with increasing cycles, and it is well within the RF capabilities to track the frequency after each cycle.

Another interesting possibility is to drive the gun through the cathode stalk. The coupling factor can be varied across a very broad range by changing the geometry of the cathode stalk. The target coupling in the subject design is relatively low to accommodate a low average current beam at a 1 MHz bunch repetition rate. Achieving low coupling factors is a challenge in this design, while high coupling factors are easier to achieve. Electrical isolation of the cathode stalk is also possible, allowing a bias voltage to be applied to the stalk to reduce the risk of multipacting.

OPERATIONAL ISSUES – THE FZD EXPERIENCE

J. *Teichert*

PHOTOCATHODES FOR SRF GUNS

For CW operation with medium average currents up to about 10 mA, cesium telluride photo cathodes (PC) seem to be well-suited. This type of semiconductor PC is widely used in normal conducting RF guns [37,38]. Their high photoemission threshold of 3.8 - 4 eV requires UV light, but quantum efficiencies (QEs) up to 20% and operational lifetimes of months have been achieved. The Cs_2Te PCs must be prepared, stored and handled in UHV with a pressure of at most 10^{-9} mbar. For the SRF gun at the FZD, a PC preparation lab was established and systems for the exchange of the PCs have been designed and installed. Figure 12 shows the cathode transfer system attached to the SRF gun.

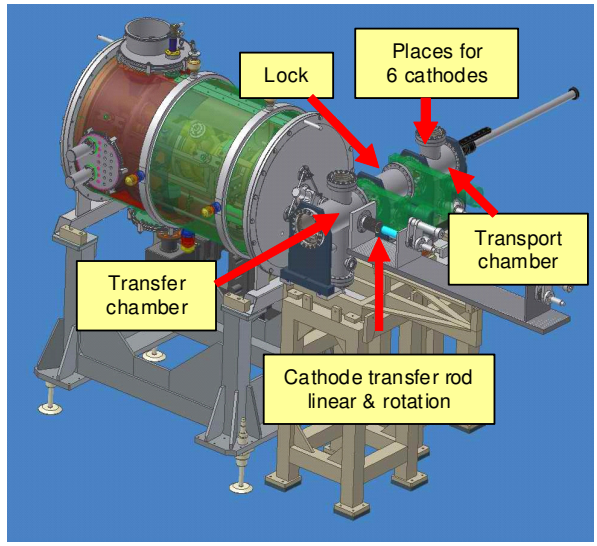

Figure 12. Design of the photo cathode transfer system of the SRF gun at FZD.

A second similar system is connected to the photo cathode preparation equipment. In the transport chamber the PCs are moved and stored before their use in the gun. The design of the cathode plug differs from that in NC guns since the cathode must be separated from the cavity and cooled with liquid nitrogen; further, the prevention of particle production is essential. The FZD design also ensures that the cathodes can be exchanged without warming up the cryomodule.

The evaporation equipment allows the fabrication of Cs_2Te films with the standard technique, where at first a ~10 nm Te layer is deposited following the Cs deposition until the maximum of photo current is reached, as well as the co-evaporation introduced by CERN [39]. The PCs produced with the standard technique in 2008/09 had QEs of 5 – 8% after preparation [40]. Some technical shortcomings caused an increase of vacuum pressure during PC exchange in the transfer system with the result that the PCs had QEs of about 0.1% in the gun [41]. This technical problem was solved. For the first set of Cs_2Te PCs produced in 2009 the long-term behavior is shown in Figure 13. According to the gun specification, 1% QE is sufficient for operation and could be sustained for storage times longer than 60 days. For the cathode transferred into the gun, no QE drop-down was found. This PC was in operation until the end of the run in June without any change in QE. Typical emission currents were between 1 and 20 µA.

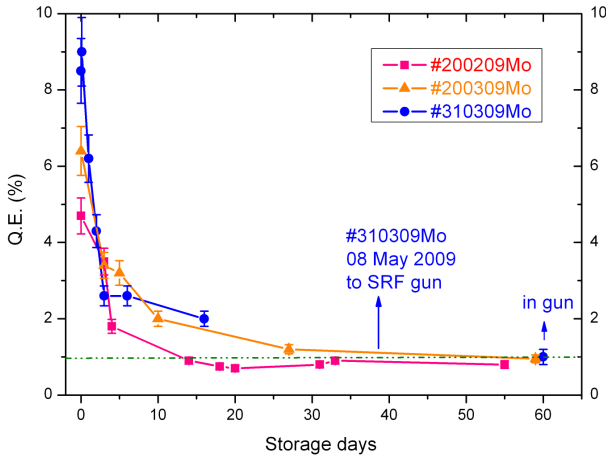

Figure 13. Long-term behavior of Cs_2Te photo cathodes for the SRF gun.

THE ROSSENDORF SRF GUN

The SRF gun for the SC linear accelerator ELBE was developed within a collaboration of the German institutes BESSY/HZB, DESY, MBI and FZD, and was put into operation in 2007. The niobium cavity with 1.3 GHz resonance frequency consists of 3½ cells and an additional choke cell. The full cells have the standard TESLA shape [42] whereas the half-cell has a special design obtained from RF and beam dynamical simulations. In the cavity a normal conducting PC, metallic or semiconducting, can be used. The PC is thermally isolated from the cavity by a vacuum gap, held by a special support system and cooled with liquid nitrogen. The cavity has two tuners (the first for the half-cell and the second for the three TESLA cells together), two HOM couplers, and an ELBE-type input coupler for 10 kW RF power [43]. Details of the SCRF gun design have been published elsewhere [44].

The cavity was fabricated at ACCEL, surface treated (buffered chemical polishing) and cleaned at DESY and ACCEL, and the vertical tests were carried out at DESY. The main problem was the cleaning of the cavity due to the small apertures in the choke and the half-cell and a surface damage produced during treatment [45]. After repeated cleaning and four vertical tests a maximum peak field of 23 MV/m could be achieved, still limited by field emission. After helium tank welding, cryostat assembly and gun commissioning an acceleration gradient of 5.5 MV/m was obtained which corresponds to a peak field of 15 MV/m. The results of the regularly measured cavity performance (unloaded quality factor Q_0 vs. acceleration gradient) are summarized in Figure 14. A high power processing carried out at the end of the run in 2008 improved the gradient to 6.5 MV/m (18 MV/m peak field). The curve obtained in 2009 (11^{th} measurement) verifies the curve from 2007, i.e. any degradation of the cavity performance could not be found after about 500 h beam time with Cs_2Te cathodes in the cavity.

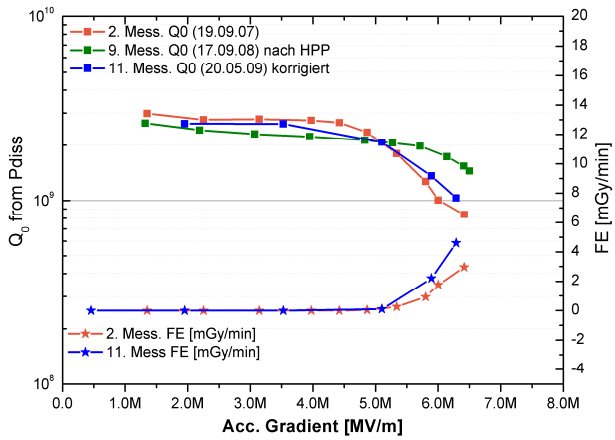

Figure 14. Unloaded quality factor Q_0 vs. acceleration gradient and the corresponding field emission dose (right side). "2.Meas" taken September 2007, "9.Meas" taken after high power RF processing (HPP) of the cavity in September 200; "11.Meas" taken after reinstallation in spring 2009.

Since for the present cavity the designed acceleration gradient could not be achieved and the field at the cathode is rather low, the electron beam dynamics are mainly determined by space charge effects. Thus beam parameter measurements were focused on the question of which bunch charges and emittances could be produced with the given gradient. Figure 15 shows laser phase scan measurements for different laser repetition rates between 2 and 125 kHz at constant laser power of 55 mW. The bunch charge (current) was measured with a Faraday cup about 1 m downstream from the gun. At the optimum laser phase, 300 pC could be produced. The maximum average current achieved up to now was 15 µA at 125 kHz repetition rate and 130 pC.

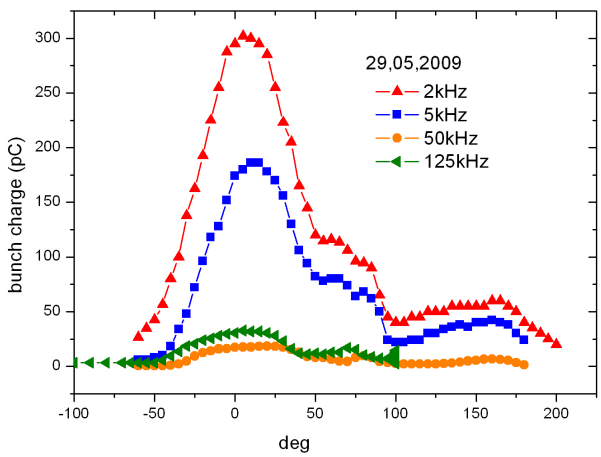

Figure 15. Laser phase scan with 55 mW laser power for different laser pulse repetition rates.

Simulations showed that the coaxial channel between the half-cell back wall and and the cathode stem is the most critical place for multipacting in the cavity. Indeed, multipacting was found at that position during ramping-up the RF. With a DC bias of the cathode up to -7 kV the

effect could be eliminated. The strength and duration of this effect were different for different cathodes, which will be studied more systematically. Compared to the quarter wave choke joint of BNL [46] the choke filter design of the FZD cavity does not produce multipacting problems.

The transverse emittance has been measured with the solenoid scan method using the gun solenoid and two following screens, with the results shown in Figure 16.

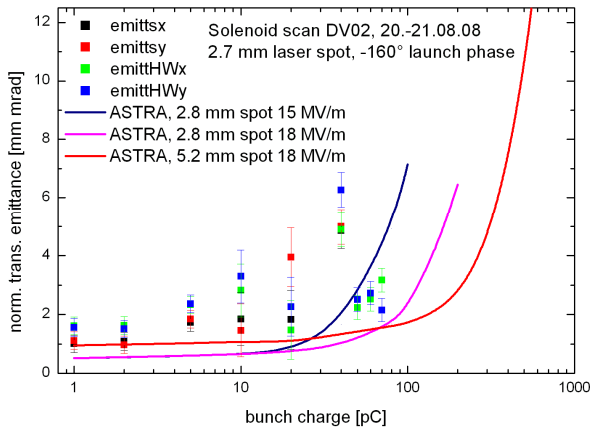

Figure 16. Normalized transverse emittance as a function of bunch charge at optimum laser launch phase measured with the solenoid scan method using beam spot on screen 2. Measurement in horizontal (x) and vertical (y) direction, direct rms beam spot size (emittHM), and Gaussian fit (emitts).

For the measurements, the acceleration gradient was 5 MV/m, the laser spot diameter 2.7 mm. Measurements were carried out up to 70 pC. For higher bunch charges the method could not be applied. The strong space charge effect causes a solenoid current dependence of the beam size which could not be fitted with the theoretical curve. Furthermore the beam shows an increasing halo. The results of the emittance measurements as function of bunch charge are presented in Figure 16.

The measurement agrees sufficiently with the ASTRA simulation performed with similar parameters (2.8 mm Laser spot, 15 MV/m peak field). Further simulations show that an increase of the acceleration gradient to 6.5 MV/m (18 MV/m peak field) and an optimized laser spot of 5.3 mm diameter would allow bunch charges up to 400 pC with transverse emittances ≤ 8 mm mrad, which is acceptable for ELBE.

A summary of the beam parameter measurements carried out in 2008 is given in Table 3. The table also shows the planned parameters for the two operational modes at ELBE with the existing cavity. Two new slightly modified cavities have been designed and are under construction in collaboration with JLab. For these cavities a higher gradient is expected allowing operation with the design parameters given in two last rows of the table. The gun will be operated in two different modes: the FEL mode with 13 MHz and low emittance for the FELs, and the second mode with maximum bunch charge for neutron and positron production.

INSTALLATION AND CONNECTION ISSUES

R. Legg

Several potential problem areas were highlighted during the workshop concerning SRF electron gun installation and interconnection issues. Residual magnetic fields in and around the cryostat must be carefully degaussed or aberrant magnetic fields can be "frozen" into the cavity's structure [47]. The peak field levels only need to be a few gauss to produce an integrated field which distorts the beam. Unfortunately, the field itself may be inside the cryostat making it inaccessible and difficult to do a direct measurement. The resulting beam aberration is difficult to trace since many other magnetic elements may be involved. Careful installation of the cavity is essential to avoid this issue.

The means to put a DC bias of several hundred volts on the cathode to suppress multipactoring in the region between the cavity and the warm cathode after installation

Table 3: Measurement results and design parameters of the Rossendorf SRF gun, showing the results of measurements in 2008, the operational parameters for 2009 with the existing cavity, and the expected parameters for a new cavity with higher gradient.

	present cavity			new "high gradient cavity"		
	measured ´08	FEL mode	high charge mode	FEL mode	high charge mode	
electron energy	2.1 MeV	3 MeV		≤ 9.5 MV/m		
peak field	13.5 MV/m	18 MV/m		50 MV/m		
laser rep. Rate	1-125 MHz	13 MHz	2-250 kHz	13 MHz	≤500 kHz	
laser pulse length (FWHM)	15 ps	4 ps	15 ps	4 ps	15 ps	
laser spot size	2.7 mm	5.2 mm	5.2 mm	2 mm	5 mm	
bunch charge	≤ 200 pC	77 pC	400 pC	77 pC	1 nC	
average current	1 µA	1 mA	100 µA	1 mA	0.5 mA	
peak current	13 A	20 A	26 A	20 A	67 A	
transverse norm. emittance (rms)	3±1 mm mrad @ 80 pC	2 mm mrad	7.5 mm mrad	1 mm mrad	2.5 mm mrad	

was deemed crucial by both the FZD and BNL groups [48,49]. This requires planning for the electrical isolation of the cathode and its support tube and for the connection of the cathode to an external power supply.

Alignment of the cathode with respect to the cavity was also considered key. Initial installation and alignment of the cathode holder requires that the cathode be placed both transversely and longitudinally with respect to cavity very precisely. FZD suggests a precision much better than 0.1 millimeters [50]. The process is further complicated by the differences in shrinkage by the various materials in the cavity and the cathode holder as they are cooled.

Alignment of the solenoid and downstream elements with the cathode spot is important to minimizing emittance growth due to chromatic effects. Cornell [51] uses stages to move their solenoid to the electrical centerline of the beam path from the gun. By adjusting the solenoid position, they minimize the chromatic and steering effects caused by misalignment and they can track the cathode spot as it is moved off-axis to avoid ion back bombardment of the emission site. JLAB [52] sees an increase from 3 to 5 μm caused by the cathode spot being off-axis relative to the solenoid and buncher. The increase does not affect their ability to lase and consequently has not been looked at further.

Solenoids are commonly used for emittance compensation [44,45,46,47]. To move the solenoid closer to the cathode, several groups are using superconducting solenoids (made of Nb, NbTi or high-Tc wires) located within the cryovessel, with cooling typically provided from the helium dewar to the solenoid either with straps or cooling passages. This allowed the solenoid to be placed as close as possible to the cathode for optimal emittance compensation. BNL had further suggested using a bucking coil to cancel the field and allow the solenoid to be placed closer yet to the cathode. At least one design used a niobium shield over the solenoid which excluded field from the cavity in the event of a cavity quench.

Photocathodes are a common element for SRF and DC electron guns. Field emission and / or dark current from photocathodes has been a problem for JLAB [52]; but have not been for Cornell [51] at 250 kV on the photocathode. T. Rao suggested nano-patterning the cathode to limit specular reflection from the cathode which might cause photoemission in the cavity. This would also minimize the effect of reflections in the drive laser transport line causing halo or multiple beams. Certainly care must be taken in selecting the optical elements in the drive laser line to prevent unintended beam effects. This is also a problem as the photon energy of the drive laser is increased for metal cathodes [57] where ordinary optical elements are not transparent, and many materials in the gun cavity may have work functions lower than the photon energy.

RF couplers [58] for the presently planned SRF electron guns are typically coaxial rather than waveguide designs. They have the advantage that they are more compact with a smaller heat leak than the waveguide designs; but the waveguide designs have better power handling capability and are simpler to cool. All current SRF gun designs use coaxial couplers. The consensus at the Workshop for the lack of waveguide-based designs was that compactness and simplicity were the overriding factors in the coupler selection. Another other issue will be vacuum pumping through these couplers as the power requirements go up. With greater power will come increased heat and gas desorption and the need for increased pumping to prevent condensation in the cavity.

JLAB [52] mentioned that they had more problems with their mundane equipment. Conventional facilities for an SRF electron gun and its drive laser include cooling water, liquid N_2, liquid He, AC power, dry N_2 gas, compressed air and an HVAC system of surpassing quality for constant room and water temperatures. There are also associated problems of vibrations, unintended electrical ground paths, stray magnetic fields and instrumentation and control requirements. Finally, or more correctly, firstly, there are the safety and interlock systems [59] to protect the personnel and equipment from injury or damage. All these "low tech" systems must be interfaced to the electron gun and its enclosure and work properly for the gun to start to do its job.

CLOSING THOUGHTS AND COMMENTS

Developments are proceeding apace for both DC and SRF guns. Development of SRF guns has branched into two types, elliptical and quarter-wave cavity geometries, with each having advantages and disadvantages. While there has been more development of the elliptical cavity designs to date, performance data from both designs is expected in the near future.

There are no shortage of problems and concerns for ERL injector development. While some of these, such as cathode selection and conventional facilities, will be common to all ERL beam sources, others are specific to the type of beam source used. Therefore, the increasing number of beam source candidate designs may be seen as a positive development, indicating the great amount of thought and effort being directed to identifying and ameliorating these effects.

ACKNOWLEDGEMENTS

The conveners and participants of Working Group I wish to thank the conference organizers, and our fellows in the community, for a successful and thought-provoking workshop.

REFERENCES

[1] S. Zhang, Tuesday's talk, this Workshop
[2] L. Jones, Tuesday's talk, this Workshop
[3] I. Bazarov, Proced. PAC09, Vancouver (2009)
[4] B. Dunham, Monday's talk, This Workshop
[5] A.Shama, PRST 12 (3), 033501 (2009).
[6] P. Musumeci, PRL 100, 244801(2008)
[7] Y. Li, Tuesday's talk, this Workshop

[8] J. Smedley, T. Rao, and Q. Zhao, J. Appl. Phys. **98**, 043111 (2005).
[9] J. Smedley, T. Rao, and J. Sekutowicz, Phys. Rev. ST Accel. Beams. 11, 013502 (2008).
[10] T. Rao et al., Proceedings of 2005 Particle Accelerator Conference, Knoxville, TN
[11] J. Smedley et al, Proc. of PAC07, 1365 (2007).
[12] J. Sekutowicz et al, Proc. of PAC07, 962 (2007).
[13] Juan R. Maldonado et al, Phys. Rev. ST, Accel. Beams, **11** 060702(2008)
[14] D.H. Dowell, S.Z. Bethel, K.D. Friddell, Nucl. Inst. and Meth. in Phys. Res. A 356 167 (1995)
[15] X. Chang et al, Proc. of PAC09, (2009).
[16] J. Smedley et al., Diamond Amplified Photocathodes, MRS Fall 2007, 1039-P09-02 (2007)
[17] A. Lyashenko et al., J. Appl. Phys. (2009) accepted, arXiv:0904.4881
[18] A. Michalke, PhD Thesis, WUB-DIS 92-5 Univ. Wuppertal, 1992.
[19] E. Barthels, et al., Nucl. Inst. and Meth, A 445 (2000) 408.
[20] D. Janssen, et al., Nucl. Inst and Meth. A 507 (2003) 314.
[21] A. Arnold, et al., Nucl. Inst. and Meth. A 577 (2006) 440.
[22] J. Sekutowicz et al., Phys. Rev. ST Accel. Beams. 8, 010701 (2005).
[23] J. Knobloch et al, to be published, see http://www.helmholtz-berlin.de/forschung/gross-geraete/beschleunigerphysik/berlinpro/index_de.html
[24] J. Kewisch et al., Proceedings of 2009 Particle Accelerator Conference, Vancouver, Canada.
[25] A. Burrill et al., Proceedings of 2007 Particle Accelerator Conference, Albuquerque, NM.
[26] D. Kayran et al., Proceedings to LINAC08 Victoria BC, Canada.
[27] M. Johnson et al., "Cryomodule Design for a Superconducting Linac with Quarter-Wave, Half-Wave and Focusing Elements", Proc. of the 2005 IEEE Particle Accelerator Conference, Knoxville TN (2005).
[28] W. Hartung et al., "Niobium Quarter-Wave Resonator Development for the Rare Isotope Accelerator", Proc. of the 11th Workshop on RF Superconductivity, Travemunde, Germany (2003). (arXiv:physics/0412031v1)
[29] Kui Zhao et al., Nucl. Instr. and Meth. A475 (2001), p. 564.
[30] Jiankui Hao et al., Nucl. Instr. and Meth. A557 (2006), p. 138.
[31] Feng Zhu et al., High Energy Physics and Nuclear Physics, Vol.31, No.5(2007), p.496.
[32] R.A. Rimmer et. al., "A high-gradient CW RF photo-cathode electron gun for high-current injectors," Proc. PAC05, Oakridge, TN, USA (2005) 473-475.
[33] J.W. Staples et. al., "Engineering design of the LUX photoinjector," Proc. European Particle Accelerator Conf. 2004, Lucerne, Switzerland (2004) 473-475.
[34] X. Chang et. al., "High Average Current Low Emittance Beam Employing CW Normal Conducting Gun," Proc. PAC07, Albuquerque, NM, USA (2007) 2547.
[35] J.W. Staples et. al., "Design of a VHF-Band RF Photoinjector with Megahertz Beam Repetition Rate," Proc. PAC07, Albuquerque, NM, USA (2007) 2990.
[36] H. Bluem et. al., "Normal Conducting CW RF Gun Design for High Performance Electron Beams," Proc. EPAC08, Genoa, Italy (2008) 223.
[37] L. Monaco et al., Proc. PAC07, Albuquerque, USA, 2007, p. 2763, http://www.jacow.org
[38] G. Suberlucq, Proc. EPAC04, Lucerne, Switzerland, 2004, p. 64, http://www.jacow.org
[39] G. Suberlucq, Proc. CTF3 Review, CERN, October 2001
[40] R. Xiang et al., CARE Report-2008-029-PHIN, http://esgard.lal.in2p3.fr/Project/Activities/Current
[41] J. Teichert et al., Proc. FEL´08, Gyeongju, Korea, 2008, p. 467, http://www.jacow.org
[42] B. Aune et al., Phys. Rev. Special Topics, 3 (2000) 092001
[43] H. Buettig et al., Nucl. Instr.and Meth. in press
[44] A. Arnold et al., Nucl. Instr.and Meth. A577 (2007) 440
[45] J. Teichert et al. Proc. FEL´07, Novosibirsk, Russia, 2007, p. 449, http://www.jacow.org
[46] A. Burrill et al., Proc. PAC07, Albuquerque, USA, 2007, p. 2544, http://www.jacow.org
[47] S. Belomestnykh, "Cornell ERL Injector Linac Testing Status", ERL09, Ithaca, NY, June 2009
[48] J. Teichert, "FZD SRF Gun Development and Testing", , Ithaca, NY 2009
[49] A. Burrill, "SRF Gun Development", Proc of ERL09, Ithaca, NY 2009
[50] V. Volkov and D. Janssen, Proc. of EPAC 2000, Vienna, Austria, p 2055
[51] I. Bazarov, "SRF Gun Discussion: Operational Issues", Proc of ERL09, Ithaca, NY 2009
[52] S. Bensen, "SRF Gun Discussion: Operational Issues", Proc of ERL09, Ithaca, NY 2009
[53] Ilan Ben-Zvi, Proc. of The Second Workshop on High Average Power & High Brightness Beams, UCLA, 2009
[54] T. Kamps, Proc of The Second Workshop on High Average Power & High Brightness Beams, UCLA, 2009
[55] T. Grimm, "Niobium Gun Fabrication Issues", Proc of ERL 09, Ithaca, NY,June 2009
[56] R. Legg, et al., Proc of EPAC 08, Genoa, Italy, 2008
[57] J. Smedley, et al., Proc of PAC 2005, p 2598, Knoxville, TN, 2005
[58] A. Burrill, "SRF Gun Discussion: Power Coupling and HOM Damping", Proc of ERL09, Ithaca, NY 2009
[59] http://www.jlab.org/ehs/ehsmanual/6000.html

STATUS OF THE JEFFERSON LAB ERL FEL DC PHOTOEMISSION GUN

C. Hernandez-Garcia*, S. V. Benson, G. Biallas, J. Boyce, D. Bullard, J. Coleman, D. Douglas, P. Evtushenko, C. Gould, A. Grippo, J. Gubeli, F. Hannon, D. Hardy, M. Kelley, J. Kortze, K. Jordan, J. M. Klopf, M. Marchlik, W. Moore, G. R. Neil, T. Powers, D. Sexton, M. Shinn, C. Tennant, R. Walker, G. Williams, and S. Zhang, TJNAF, Newport News, VA 23606, USA

Abstract

The Jefferson Lab (JLab) Energy Recovery Linac 10 kW IR Upgrade Free Electron Laser (FEL) is driven by a 350kV DC un-polarized photoemission electron gun. In 2003, an upgrade version of the earlier 1 kW IR Demo FEL gun delivered over 1000 Coulombs with a single Cs:GaAs wafer in one year of operation. Between 2004 and 2007 a second wafer delivered over 7000 Coulombs and up to 9 mA CW beam for FEL operations. Both wafers suffered surface damage with total loss of quantum efficiency in several occasions during high current operations. Since then, the electron gun has been refurbished two times after suffering damage caused by excessive field emission. Although presently operating at nominal 350kV, field emission has significantly decreased the photocathode lifetime.

INTRODUCTION

The JLab 10 kW IR Upgrade FEL DC photoemission gun has been in operation since 2003 [1]. The Upgrade Gun operates at 350kV and it is a direct evolution of the earlier JLab 1 kW Demo IR FEL gun that operated at 320kV [2].

The photocathode is 3.2 cm diameter single crystal bulk GaAs wafer, 600 micron thick and Zn-doped at ~$1x10^{18}$ cm^{-3}. By retracting it inside the ball electrode, the wafer is activated in-situ into a Negative Electron Affinity (NEA) photocathode. It is illuminated with a frequency-doubled, mode-locked Nd:YLF drive laser to generate 135 pC per bunch. Each laser pulse is 50 ps FWHM at 527 nm. With a repetition rate of 75 MHz the gun delivers electron beam at 10 mA CW [1,2].

In 2003 a bulk GaAs wafer from Matek delivered over 1000 Coulombs and up to 9 mA CW. In 2004 it was replaced with a second wafer from AXT and was in service for three years, until a leak in the gun vacuum chamber opened while operating the gun at 400 kV. A field emitter developed on the support electrode even though the gun had been conditioned up to 450kV in 2004 and operated at 350kV for thousands of hours. Failure of the Machine Protection System to shut down the high voltage power supply led to a catastrophic leak when 100 μA of field emission current heated the 14-inch conflat flange Cu gasket and SF^6 leaked into the vacuum chamber.

In early 2008 the gun was rebuilt with a third wafer. During the high voltage-conditioning phase, one of the ceramic insulators suffered a puncture from excessive field emission. The insulator and the support tube electrode were replaced, the gun was re-built and in the fall of 2008 it was high-voltage conditioned again without much success, until processing with Krypton gas [3]. However, excessive field emission from the wafer prevented FEL operations. In January 2009 a new wafer was installed, and the gun had to be re-conditioned with Kr gas processing. Although the field emission, identified to be from the ball cathode, is on the order of a few micro-Amperes at 350kV, the gas desorption induced by field emitted electrons striking the chamber is sufficient to decrease the photocathode lifetime from 50 operational hours observed in 2004-2007, to only 8 operational hours. The implementation of a motorized cathode manipulator system has reduced FEL down time for quantum efficiency replenishing (re-cesiation) from 3.5 hours to 0.5 hours.

PHOTOCATHODE PERFORMANCE

The Matek GaAs wafer installed in May 2003 delivered over 1000 Coulombs in one year of service and up to 9 mA CW beam (122pC per bunch at 350 keV) [1]. The second wafer, from AXT, was anodized around the edge leaving a 1.6 cm diameter active area to reduce electron beam halo caused by drive laser scatter light. The drive laser spot on the cathode was kept at 0.8 cm diameter and at 0.4 cm off the electrostatic center to avoid the Quantum Efficiency (QE) degradation spot by back-ion bombardment. This wafer was in service for 36 months and was activated into a NEA photocathode 9 times achieving routinely 6-7% QE. The QE was replenished six times between activations by spraying fresh Cesium onto the photocathode surface. If the photocathode were re-cesiated more than six times, Cesium would accumulate on the surface leading to tens of nano-Amperes of field emission observed on a phosphor screen beam viewer downstream of the gun. Typically 96% of the previous QE was recovered with each re-cesiation. The 1/e lifetime was 550 Coulombs or 50 operational hours with 5 mA CW beam (135pC per bunch at 350 keV). The total extracted charge from that wafer was 7000 Coulombs in 900 operational hours with a beam current between 1 and 8.5 mA CW.

Both wafers, the Matek and the AXT, suffered surface damage while delivering beam in excess of 8.5 mA CW for FEL operations. Beyond that current level, the injector SRF booster suddenly tripped off on waveguide vacuum fault and the pressure in the gun vacuum chamber raised

three orders of magnitude. Notice in Figure 1 that about 10 seconds after the electron beam current had been shut off by the machine protection system, a current burst of at least 3 mA occurred while the gun was still at 350kV causing a second, larger pressure surge up to ~3x10^{-7} Torr.

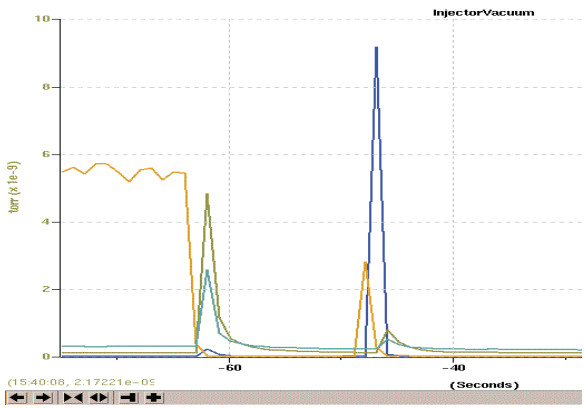

Figure 1. Strip tool showing the electron beam current (yellow, 0-10 mA), the gun vacuum (blue, 0-3x10^{-7} Torr) and downstream beam line vacuum levels. The horizontal scale is in seconds.

Despite the total loss of QE after each event, the wafer was heat-cleaned and re-activated in-situ into a NEA photocathode. The FEL operations would typically resume by the next morning. These events occurred in several occasions and on both wafers. Although bright spots were observed on the wafer with the cathode camera under CW drive laser illumination, the extent of the damage was not known until the wafers were removed from the gun and observed under a microscope. Figure 2 shows the anodized wafer before and after the surface damage.

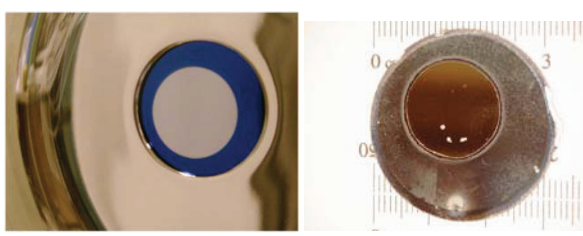

Figure 2. A) Anodized GaAs wafer mounted in the ball electrode. B) The same wafer removed from the ball cathode after three years of operation. The spots from left to right are labeled as Spot#1, Spot#2, and Spot#3.

Notice the three damage spots on the lower half of the active area (smaller circle within the wafer). The dull white color of the spots is characteristic of GaAs when it is heated beyond the congruent temperature, 632 Celsius [4,5].

SURFACE CHARACTERIZATION

Figure 3 is a Field Emission Scanning Electron Microscope (FESEM) picture of Spot #3, which seems to be comprised by craters, similar to those found in laser-induced damage at ~1 J/cm^2 observed by Huang et al. [6]. The GaAs surface remains smooth beyond the boundary of the craters.

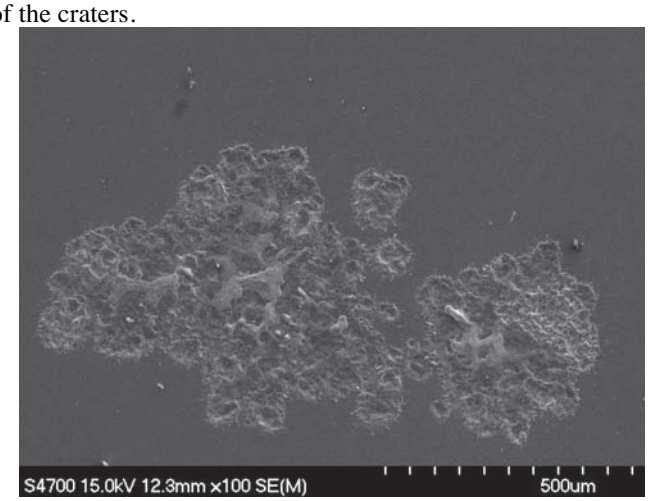

Figure 3. FESEM Picture of Spot #3.

Outside the damage spots, the wafer surface roughness increased by a factor of 30 compared to that from a fresh sample, as shown by the Atomic Force Microscopy (AFM) images in figure 9.

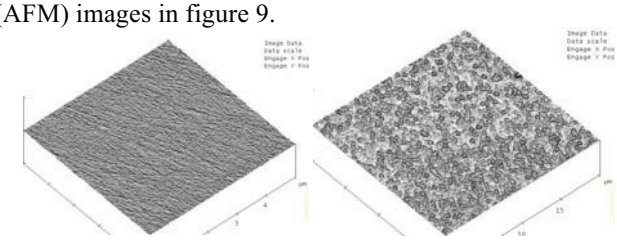

Figure 9. a) AFM from a fresh GaAs sample, surface roughness is 1 nm. b) AFM from the GaAs exposed to the gun operational environment, surface roughness 30 nm.

It has been reported that heat-cleaning results in rough crystal surface due to evaporation in equal amounts of Gallium and Arsenic up until the congruent temperature [7,4]. In a separate test vacuum chamber, a fresh GaAs wafer was heated to 550 Celsius for one hour, the typical heat cleaning procedure, and therefore never exposed to high voltage and ion-back bombardment. The AFM results show that the surface roughness was 10 nm after the heat clean, a factor of 3 lower than that of the wafer in the gun and a factor of 10 higher compared to that of the fresh sample. Chatillon and Chatain have also observed the droplets seen in Figure 9, “after a certain time the surface reaches a steady-state of vaporization with well-defined proportion of (Gallium rich) droplets” [4].

CONCLUSIONS

The damage mechanism is not laser-drive since all three spots are located outside the drive laser illumination area, but they are very close to the electrostatic center of the wafer. Figure 1 shows that the pressure peaked at a higher level in the electron gun vacuum chamber than in the downstream beam line at the time the electron beam current was turned off by the machine protection system. About 10 seconds later, with the gun still at 350kV, a current burst of at least 3 mA is accompanied by a second pressure burst initiated in the gun vacuum chamber that migrated down the beam line. Liu et al. report that the expansion velocity in laser-induced damage on GaAs approaches that of a fluid in free expansion into the vacuum when the material exceeds the melting point [8].

It is not clear if the trigger mechanism was originated in the gun vacuum chamber or in the SRF booster downstream of the electron gun. One possible scenario is that electron beam halo observed at currents beyond 5 mA CW strikes the SRF cavities causing a sudden stop of acceleration. The electrons then strike the beam line walls desorbing gas, which migrates to the gun vacuum chamber and is ionized by the still present electron beam in the photocathode-anode gap. The ions, most likely hydrogen, induce crater-like surface damage on the GaAs wafer [9], which seconds later literally arcs, possibly generating a short-lived plasma, causing the current spike followed by the second pressure burst. The spots on the wafer surface are the result of very high temperatures induced by the high current density.

The events shown in Figure 1 have not been observed below 8.5 mA CW. Efforts have been made to reduce even further the electron beam halo at high currents, but since the FEL has not been operated at that current level since 2007, there is no data to corroborate the cathode damaging mechanism presented in this work. It is important to stress that the photocathode was fully operational a few hours after each damaging event.

The wafer surface roughness induced by the heat cleaning process can be eliminated if hydrogen cleaning is used instead, which requires temperatures below 400C rather than 550C [10]. This technique cannot be performed in the present gun, however it will be implemented in the next gun design, which will incorporate a load-locked chamber.

ACKNOWLEDGMENTS

This work supported by the Office of Naval Research, the Joint Technology Office, the Air Force Research Laboratory, U.S. Night Vision Lab, the Commonwealth of Virginia, and by DOE Contract DE-AC05-060R23177. The authors wish to thank Dr. Alex Bugayev from Old Dominion University for the EDS and SEM on the Matek wafer and to Mrs. Amy Wilkerson from the College of William & Mary for the surface analysis on the AXT wafer.

REFERENCES

[1] C. Hernandez-Garcia, et al., 2005 Particle Accelerator Conference, Knoxville, TN, 3117.
[2] T. Siggins, et al., Nucl. Instrum. Methods Phys Res., Sect. A **475**, 549 (2001).
[3] C. Hernandez-Garcia, et al., SPIN-PESP proceedings 2008, in press.
[4] C. Chatillon, and D. Chatain, Journal of Crystal Growth, 151 (1995) 91-101.
[5] J. Grames, JLab-TN-04-005, 09-March-2004.
[6] A. L. Huang, et al., Applied Optics, Vol. 25, No. 21, November 1986, p. 3864.
[7] K. A. Elamrawi, and H. E. Elsayed-Ali, J. Vac. Sci. A. Vol. 17, No. 3, 1999.
[8] J. M. Liu, A. M. Malvezzi and N. Bloembergen, Appl. Phys. Lett. 49 (11), 15 September 1986, 622-624.
[9] C. K. Sinclair, Nucl. Instr. Meth. A. 557, (2006) 69-74
[10] C. K. Sinclair, et al., Phys. Rev. ST Accel. Beams 10, 023501 (2007)

3D LASER PULSE SHAPIG, MEASUREMENT, AND 3D ELECTRON BEAM PROFILE MEASUREMNT FOR PHOTOINJECTORS

Yuelin Li, ANL, Argonne, IL 60439, U.S.A.

Abstract

We propose a scheme of shaping laser pulses in 3D exploiting chromatic aberration and laser phase tailoring. We demonstrated an interferometry method of measuring 3D distribution of a laser pulse. For the electron beam diagnostics, a non interceptive time resolved laser wire scheme is proposed using a ultrafast laser pulse in a line focus to scatter from the beam under consideration. By imaging the scattered photons at different delays between the laser and the beam, the 3D distribution can be reconstructed.

INTRUDCUTION

For high brightness photoinjectors, it is critical to be able to shape the 3D form of the drive laser pulse, to understand its actual 3D distribution, and the initial electron beam in order to properly compensate the emittance growth [1, 2].

We propose a 3D pulse shaping scheme which can be potentially used to generate 3D uniform ellipsoidal beam [3]. In a proof of principle experiment [4, 5], we demonstrated that the shaping method and at the same time developed a method for measuring the 3D distribution of a laser pulse based on a crossing interferometer. We also propose to use a time-resolved laser wire to measure the 3D distribution of a low energy electron beam, e.g., one that is leaving a photoinjector, based on imaging the photons scattered from the electron beam from a ultrafast laser pulse.

3D LASER PULSE SHAPING

To shape the laser pulse in 3D, we exploit the chromatic aberration effect in an optical lens. The dependence of the refractive index upon the optical frequency gives rise to the chromatic aberration in a lens, where the change of the focal length due to a shift in frequency $\delta\omega$ is

$$\delta f = -\frac{f_0}{n_0 - 1}\chi\delta\omega, \tag{1}$$

where f_0 is the nominal focal length at ω_0. We assume a constant $\chi=dn/d\omega$ for this analysis. For a Gaussian beam, the beam size at the nominal focal plane is

$$w \approx w_0\left[1+\left(\delta f / z_R\right)^2\right]^{1/2}. \tag{2}$$

Here $w_0=N\lambda_0/\pi$ is the beam waist at the nominal wavelength λ_0, with N the numerical aperture, and $z_R=\pi w_0^2/\lambda_0$ is the Rayleigh range. It is obvious, therefore, if one can program $\delta\omega$ in time, a time-dependent beam size can be achieved. At $\delta f >> z_R$, one has $w(t) \cong |\delta f(t)|/N$, thus the phase of the laser pulse is

$$\phi(t) = \pm\int \delta\omega(\mathrm{t})dt = \pm\frac{n_0 - 1}{\chi}\frac{N}{f_0}\int w(t)dt\,. \tag{3}$$

For a desired time-dependent intensity $I(t)$, the amplitude of the laser should be

$$A(t) \propto I(t)^{1/2} w(t)\,. \tag{4}$$

As an example, to generate an ellipsoidal radial envelop with maximum radius of R and full length of $2T$, the transverse beam size as a function of time is $w(t) = R[1-(t/T)^2]^{1/2}$. Using Eq. (3), this in turn gives the phase,

$$\phi(t) = -\omega_0 t \pm \frac{\Delta\omega}{2}\left[t\left(1-\left(\frac{t}{T}\right)^2\right)^{\alpha} + T\sin^{-1}\frac{t}{T}\right], \tag{5}$$

where α=1/2, and $\Delta\omega=(n_0\text{-}1)NR/\chi f_0$ is the maximum frequency shift. To keep the laser flux $|A(t)|^2/w(t)^2$ constant over time, we have

$$A(t) = A_0\left[1-\left(\frac{t}{T}\right)^2\right]^{\eta}, \tag{6}$$

with η=1/2. Equations (4) and (5) describe a pulse that can form a spatiotemporal ellipsoid at the focus of the a lens. In particle tracking simulations, the performed of so generated ellipsoidal beam give excellent emittance performance [3, 5].

3D LASER PULSE MEASURMENT

Method

The scheme is based on the interference between the drive laser pulse and a short interrogation pulse. The schematic of the experiment is shown in Fig. 1. Assuming that the interrogation (probing) laser and the main laser pulse has a field distribution as $\boldsymbol{A}_{\mathrm{p,\,m}}(t, \boldsymbol{r})$, the interference pattern on the detector is:

$$I(\boldsymbol{r}) = I_m(\boldsymbol{r}) + I_p(\boldsymbol{r}) + 2\cos(\omega[\tau+\delta(\boldsymbol{r})])\times \int A_m(t,\boldsymbol{r})A_p(t-\delta(\boldsymbol{r})-\tau,\boldsymbol{r})\cos[\phi_m(t)-\phi_p(t-\delta(\boldsymbol{r})-\tau)]dt, \tag{7}$$

where

$$I(\boldsymbol{r}) = \int |A(t,\boldsymbol{r})|^2 dt \,, \tag{8}$$

is the integrated intensity and $\phi(t)$ is the phase of the laser beams; the subscripts m and p denote the main and probe beam, respectively; τ is the timing delay and $\delta(\boldsymbol{r})$ is the additional location dependent delay due to the angle between the two beams, respectively. The phase term in the integral, though impossible to evaluate for each location, only causes the interference fringes at the detector to shift. Therefore, if the probe pulse is much shorter than the main pulse, Eq. (7) can be reduced to

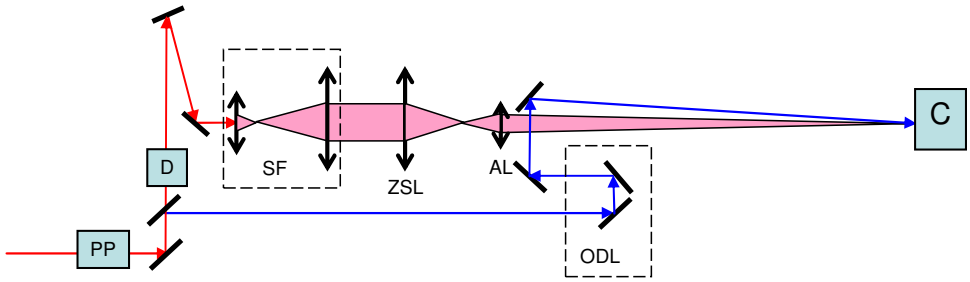

Figure 1. Schematic of the experiment for the 3D laser pulse profile measurement. Keys: PP: pulse picker; D: AOPDF; SF: achromatic spatial filter; ZSL: ZnSe lens; AL: achromatic image relay lens; ODL: optical delay line; C: camera.

$$I(\boldsymbol{r}) \approx I_m(\boldsymbol{r}) + I_p(\boldsymbol{r}) + 2\cos(\omega[\tau + \delta(\boldsymbol{r})])\sqrt{\Delta t_p i_m(\tau,\boldsymbol{r})}\sqrt{I_p(\boldsymbol{r})}. \quad (9)$$

Here Δt_p is the duration of the probe pulse, and

$$i(\tau,\boldsymbol{r}) = |A(\tau,\boldsymbol{r})|^2 \quad (10)$$

is the time-dependent intensity distribution. The second term in Eq. (9) describes the fringes as functions of delay and location, from which one can extract the contrast ratio $R(\tau, \boldsymbol{r})$, which in turn gives

$$i_m(\tau,\boldsymbol{r}) \propto R^2(\tau,\boldsymbol{r})/I_p(\boldsymbol{r}). \quad (11)$$

Experiment results

In the proof-of-principle experiment, the spatiotemporal distribution of a laser pulse shaped in 3D is measured [4, 5]. The pulse is shaped according to Eqs. (5, 6), using a combination of a lens with chromatic aberration and an acousto-optic programmable dispersive filter (AOPDF) which imposes the phase and amplitude on to the pulse. The main laser pulse has a full width of 2 ps and the probe pulse of 130 fs. The main pulse is spatially filtered to generate a Gaussian beam using a pair of achromatic lenses and a pinhole. A plano-spherical ZnSe lens (25-mm diameter, 88.9-mm radius of curvature, and 2.9-mm center thickness, Janos Technology, A1204-105) is used for its high dispersion (250 fs^2/mm at 800 nm) to form the desired spatiotemporal distribution at its focal plane. The focal plane is image-relayed by an achromatic lens onto a CCD camera to interfere with the probe beam. The interference fringes as a function of delay between the two beams are recorded on a 12-bit camera and are used to extract the spatiotemporal intensity distribution of the main beam according to Eqs. (7-11). The result of the 3D measurement is given in Fig. 2, where the measured spatiotemporal distribution is compared with that from a numerical simulation under different conditions.

The experiment shows that the method of shaping works in principle. It also shows the time resolved interferometer is very useful for measuring spatiotemporal structures of a laser pulse. The structures in the pulse are mostly due to diffraction, which is more prominent at lower beam aperture. At large apertures, these structures smooth out, as can be seen in Fig. 2, right column. Overall, the measurement shows good agreement with the Fourier optics simulation [4, 5].

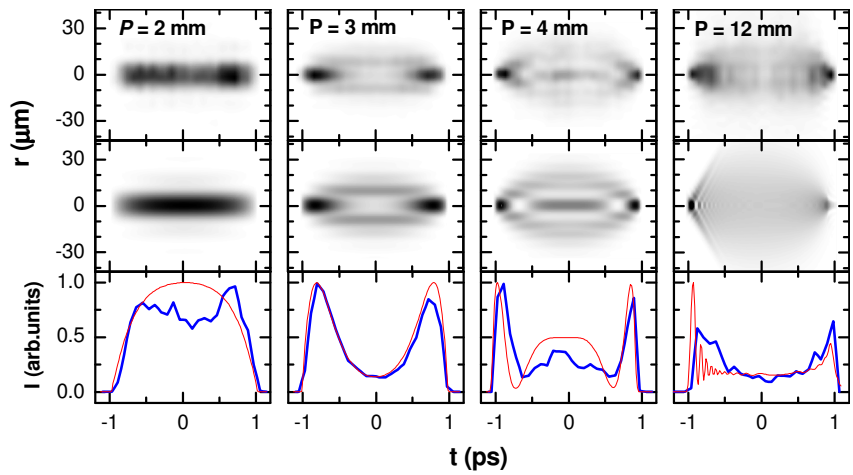

Figure 2. Measured (upper row) and simulated (middle row) spatiotemporal intensity distribution with different iris radius P using the experiment condition. The iris is located in front of the ZnSe lens in Fig. 1. The low row shows comparison of the intensity at r=0 extracted from the upper and middle rows.

METHOD FOR 3D ELECTRON BEAM PROFILE MEASUREMENT

Method

Even the laser pulse shape is fully characterized, the electron beam can still take a form different form the laser pulse shape. To measure the 3D shape of the beam, we propose a time resolved laser wire, shown in Fig. 3. A line-focused femtosecond laser pulse intersects an electron beam at 90 degree. As the laser interacts with the electrons in the beam, photons are scatter off the electrons and propagate in a cone following the electron propagation direction. The photons are collected and imaged by a proper mirror onto a 2-D area detector. As the total radiation is proportional to the local electron density, at a fixed delay, the image is a skewed time slice of the electron density distribution. By changing the delay between the laser pulse and the electron beam, a series of images are collected and can be used to reconstruct the 3D density distribution.

Assume a laser profile with a known 3 D Gaussian distribution n_p(x, y-c(t-$\bar{t}$), z) propagating the y direction,

$$n_p(x,y,z,t)=\frac{N_p}{(2\pi)^{3/2}\sigma_x\sigma_z\sigma_t}\exp\left[-\frac{x^2}{2\sigma_x^2}-\frac{z^2}{2\sigma_z^2}-\frac{(y-ct)^2}{2\sigma_t^2}\right], \tag{13}$$

where σ is the root mean square (rms) size, N_p is the total number of photons. The electron beam has energy of γ and an unknown 3-D density distribution,

$$n_e(x,y,z)=N_e f[x,y,z-v_z(\tau-t)] \tag{14}$$

propagating in the z direction at a speed of v_z, with τ the delay between the electron beam and the laser beam. Here f is the normalized density distribution function, N_e is the total number of electrons. If we set the interaction point at z=0, the number of scattered photons as a function of (x, y) at a particular τ can be expressed as,

$$n_s(x,y,\tau)=\Sigma_t N_e\iint_{t,z} f[x,y,z-v_z(\tau-t)]n_p(x,y,z,t)dtdz\cdot \tag{15}$$

Here Σ_t = 8×10^{-26} cm^2 is the Thomson scattering cross section. Set

$$\overline{f[x,y,-v_z(\tau-t)]}=\frac{1}{\delta}\int_\delta f[x,y,-v_z(\tau-t)]dt, \tag{16}$$

With

$$\delta=\sqrt{2\pi}\sqrt{\sigma_z^2+(v_z\sigma_t)^2}\cdot \tag{17}$$

The integration in Eq. (15) can be approximated by the following

$$n_s(x,y,\tau)\approx\Sigma_t N_e\overline{f\left[x,y,-v_z\left(\tau-\frac{y}{c}\right)\right]}\frac{N_p}{\sqrt{2\pi}\sigma_x}\exp\left(-\frac{x^2}{2\sigma_x^2}\right)\cdot \tag{18}$$

The term on the left hand side can be recorded on a camera via imaging optics and from which the beam distribution with a resolution in longitudinal dimension of δ can be retrieved:

$$\overline{f\left[x,y,v_z\left(\frac{y}{c}-\tau\right)\right]}\propto n_s(x,y,\tau)\exp\left(\frac{x^2}{2\sigma_x^2}\right)\cdot \tag{19}$$

Eq. (19) is a 2D electron density profile at delay τ slanted at an angle of v_z/c in the y-z plain. The 3 D profile of the beam can be reconstructed by changing the delay τ to cover the whole beam a longitudinal resolution of δ.

Technical Feasibility

To estimate the number of scattered photons, without losing generality, we assume a 3D Gaussian beam profile,

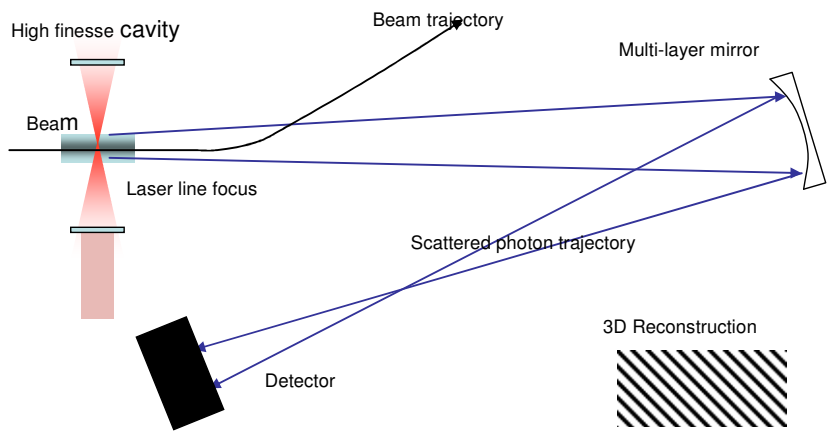

Figure 3 Top view of the schematic of the time-resolved laser wire concept. A laser pulse is stored in a high-finesse resonator cavity with a high aspect ratio elliptic beam at the center. The line focus of the laser is perpendicular to the paper. The electron beam propagates from the left and after the interaction is deflected by a bending magnet. The scatter photons are collected by a multilayer mirror and imaged on a area detector. Each image at a delay is a schewed slice of the 2 D distribution of the beam, which can be used to reconstruct the 3 D beam profile illustrated in the lower right corner, also a top view corresponding to the view of the schematic.

$$f(x,y,z)=\frac{1}{(2\pi)^{3/2}\sigma_x^2\rho_z}\exp\left[-\frac{x^2}{2\sigma_x^2}-\frac{y^2}{2\sigma_x^2}-\frac{(z-v_z t)^2}{2\rho_z^2}\right], \quad (20)$$

with a beam rms radius matched to the length of the laser line focus σ_x. Equation (18) can be now written as:

$$n_s(x,y,\tau)\approx\Sigma_t\frac{N_eN_p}{(2\pi)^2\sigma_x^3\rho_z}\exp\left[-\frac{x^2}{\sigma_x^2}-\frac{y^2}{2\sigma_x^2}-\frac{[v_z(y/c-\tau)]^2}{2\rho_z^2}\right]. \quad (21)$$

Thus the total number of scattered photon per interaction can be approximated as,

$$\begin{aligned} n_s(\tau)&=\iint_{x,y}n_s(x,y,\tau)dxdy \\ &\approx\Sigma_t\frac{N_eN_p}{2\sqrt{2}\pi\sigma_x\rho_z}\exp\left(-\frac{\tau^2}{2\rho_z^2}\right) \end{aligned}. \quad (22)$$

Here we assume that the z-variation of the distribution is small when the laser pulse propagates across the beam. With a repetition rate of the laser and beam at F and a laser accumulating cavity with a quality factor of Q, the total photon number per second at zero delay is

$$N_s(0)=QFn_s(0)\approx QF\Sigma_t\frac{N_eN_p}{2\sqrt{2}\pi\sigma_x\rho_z}. \quad (23)$$

For a typical beam condition for an ERL DC photo injector [6], let σ_x = 0.5 mm and bunch length ρ_z/v_z= 20 ps, and total charge of 100 pC, i.e., N_e=6.25×10^8, and a system repetition rate F = 100 MHz. With 5 nJ per laser pulse at 800 nm, a per pulse photon number N_p = 2×10^9 (an average power of 0.5 W, a laser of this performance is off the shelf product of many commercial vendors), we have from Eq. (22) the total scattered photon number per interaction at zero delay of 4×10^{-7}. With F= 100 MHz, this gives about 40 photons per second.

To further booster the photon number, a high-finesse passive optical cavity can be used to accumulate the laser pulse with a quality factor of Q = 10^4 by another factor of about 10^4, as has been proposed for several Thomson scattering x-ray sources [7]. This will give about 4×10^5 photons per second. In the current case, a highly elliptical beam (line focus) is needed in the resonator cavity, such asymmetric resonant cavities have been widely applied end-pumped diode laser systems where the diode pump beam is focused to line at the lasing medium [8].

To image the x-ray, it is important to be very efficient. A spherical or a paraboloidal multilayer mirror can be used to collect the light and image it onto a detector. Assuming the beam energy at about 5 MeV (γ≈10), the scattered photon energy is:

$$E=E_L\frac{2\gamma^2}{1+\gamma^2\theta^2}(1-\cos\phi) \quad (24)$$

Where ϕ= 90 degree is the crossing angle. And the differential cross section is

$$\frac{d\Sigma_t}{d\theta}\propto\frac{1+\gamma^4\theta^4}{(1+\gamma^2\theta^2)^2}\theta. \quad (25)$$

It has a maximum at $\theta\cong 0.4/\gamma$, where the photon energy is E = 1.72 γ^2 E_L. For the above beam energy γ= 10, we have the peak photon energy at E = 266 eV. This is in the soft x-ray range, where multilayer coatings with near-normal incidence reflectance of 20% has been demonstrated and higher efficiency is expected with oblique incidence angles, and with improved design and fabrication procedure [9-15]. Figure 4 is a summary of the best experiment measured reflectance for multilayer mirrors from 10 to 1000 eV.

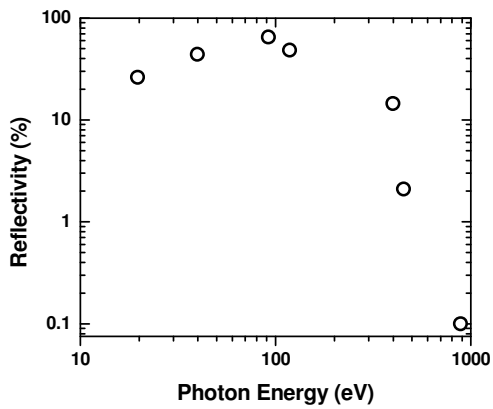

Figure 4. Best near normal incidence reflectance efficiency of multilayer mirrors as a function of photon energy. From lower to high energies, the data are adapted from refs. [9-15], respectively.

Finally, for the area detector, a back-side illuminated CCD camera, with a quantum efficiency of close to 80-90% at 266 eV [16] can be used. Using the CCD parameters in ref. [16] and the mirror efficiency, the total expected counts is about 4×10^5 per image for an integration time of one second. Of course, other high efficiency device can also be used for this purpose.

With high quality imaging system, the spatial resolution is only limited by the pixel size of the detector. The temporal resolution is limited by the line focus width of the laser and the pulse duration as expressed in Eq. (17). The temporal resolution is, in addition, also limited by the timing jitter of the between the beam and the laser, which can be well under 100 fs.

Though we limited our discussion to a low energy beam, the scheme can also be used at higher beam energy with proper imaging and detector systems. The potential difficulty as one move to high beam energy is the scaling of the scattered photon energy quickly to hard x-ray, where the efficiency of multilayer mirrors almost diminishes (see Fig. 4) although at larger off normal incidence angles the reflectance can be greatly enhanced. Although higher laser power can be part of the solution, an optimized design can take fully advance of the current advances in x-ray optics development for an efficient imaging system.

To move the scattered photon energy to lower region suitable for imaging optics, smaller crossing angle can be used as shown in Eq. (24). However, the total photon number will also be reduced by a factor of (1-cosϕ) [16].

CONCLUSION

A 3D laser pulse shaping scheme potentially useful for 3D uniform ellipsoidal beam generation is proposed and demonstrated in a proof-of principle experiment. In the experiment, a cross interferometer is developed for spatiotemporal shape measurement of the pulse. We also propose a time resolved laser wire system for 3 D electron beam profile measurement and discussed it technical feasibility.

This work is supported by the U.S. Department of Energy, Office of Science, Office of Basic Energy Sciences, under Contract No. DE-AC02-06CH11357.

REFERENCES

[1] B. E. Carlsten, Nucl. Instrum. Methods A **285**, 313 (1989);
[2] L. Serafini and J. B. Rosenzweig, Phys. Rev. E **55**, 7565 (1997).
[3] Y. Li, and J. W. Lewellen, Phys. Rev. Lett. **100**, 074801 (2008).
[4] Y. Li and S. Chemerisov, Opt. Lett. **33**, 1996 (2008).
[5] Y. Li, S. Chemerisov, and J. Lewellen, Phys. Rev. ST Accel. Beams 12, 020702 (2009).
[6] I. V. Bazarov and C. K. Sinclair, Phys. Rev. ST Accel. Beams 8, 034202 (2005)
[7] W.S. Graves, W. Brown, F.X. Kaertner and D.E. Moncton, Nucl. Instrum. Methods Phys. Research A, in press.
[8] F. Krausz, J. Zehetner, T. Brabec and E. Winter, Opt. Lett. 16, 1496 (1991); and references therein.
[9] B. Kjornrattanawanich, D. L. Windt, and J. F. Seely, Opt. Lett. 33, 965-967 (2008).
[10] T. Ejima, A. Yamazaki, T. Banse, K. Saito, Y. Kondo, S. Ichimaru, and H. Takenaka, Appl. Opt. 44, 5446-5453 (2005).
[11] C. Montcalm, R. F. Grabner, R. M. Hudyma, M. A. Schmidt, E. Spiller, C. C. Walton, M. Wedowski, and J. A. Folta, Appl. Opt. 41, 3262-3269 (2002).
[12] B. Sae-Lao and C. Montcalm, Opt. Lett. 26, 468-470 (2001).
[13] F. Eriksson, G. A. Johansson, H. M. Hertz, E. M. Gullikson, U. Kreissig, and J. Birch, Opt. Lett. 28, 2494 (2003).
[14] N. Ghafoor, P. O. Å. Persson, J. Birch, F. Eriksson, and F. Schäfers, Appl. Opt. 45, 137 (2006).
[15] D. L. Windt, E. M. Gullikson, and C. C. Walton, Opt. Lett. 27, 2212 (2002).
[16] Y. Li, Z. Huang, M. D. Borland, and S. Milton, Phys Rev ST AB 5, 044701 (2002) and references therein.

.

SRF PHOTOINJECTOR R&D AT UNIVERSITY OF WISCONSIN*

R. Legg#, M. Allen, M. Fisher, A. Hjortland, K. Kleman, University of Wisconsin, Madison, WI
T.Grimm, M. Pruitt, Niowave Inc., Lansing, MI, U.S.A.

Abstract

Next generation light sources will enable significant new science in the many disciplines including atomic and fundamental physics, condensed matter physics and materials sciences, femtochemistry, biology, and various fields of engineering. The source we propose, and the experimental methods it will spawn, will generally be qualitatively new and have high impact through ultrahigh resolution in the time and frequency domains combined with full transverse coherence for imaging and nanofabrication. Continuous wave FEL's provide the highest beam brightness[1], full temporal and transverse coherence and the potential for ultra short photon pulses at high repetition rates that the science requires. But the hardware, in particular the injector, to build such a light source has not been demonstrated yet. University of Wisconsin, in collaboration with the Naval Postgraduate School, has been engaged in a design contract with Niowave Inc to design a superconducting rf electron gun to be used for such a source. This design work and our collaboration with the Naval Postgraduate School in the construction and test of their SRF gun will allow us to produce a prototype device in a timely and cost effective manner. The design for such a development enables a User facility with the capability to explore the science in the grand challenges laid out by DOE BESAC[2] and the Science and Technology of Future Light Sources white paper[1].

BACKGROUND AND OVERVIEW

The challenges laid out in the DOE BESAC grand challenges in science and energy require new photon sources. Current accelerator technology cannot support the required goals for those sources technically. Additional accelerator research and development is required in order to enable the science in the grand challenges. The University of Wisconsin has proposed a seeded FEL, the Wisconsin Free Electron Laser (WiFEL), which is differentiated from today's synchrotron facilities or laser sources because it combines high power and coherence for the first time in the 1 to 100 nm range. The source we propose, and the experimental methods it will spawn, will generally be qualitatively new and have high impact through ultrahigh resolution in the time and frequency domains combined with full transverse coherence for imaging and nanofabrication.

The key features of the facility we envision are demanded by the scientific mission. A seeded FEL would take advantage of the flexibility, stability, and high average pulse rates available from a continuous-wave (CW) superconducting linac fed by a superconducting photoinjector. For example, a second generation seeded FEL[1] is capable of producing the very bright and short pulses required to produce the science. In order to produce beams of the highest quality, the electron beam will be seeded with high harmonics of laboratory lasers. The required electron beam requirements at the insertion devices for such a device are shown in Table 1.

Table 1: FEL Requirements

I ave, Rf power coupler limited	~ 1 mA
I peak at Undulator	1000 Amps
DI / I at Undulator	10% Max
Normalized ε Transverse	<1 mm-mrad
Bunch length, rms	70 fsec
Charge/bunch (derived)	200 pC
Gun Repetition frequency	Up to 5 MHz

The one milliamp limit for a linac based light source in the table is a function of the coupler limitations of the present generation of high gradient L-band superconducting modules. Both Tesla and Jefferson Lab 100 MeV cryomodules have couplers which can handle about 10 kW of rf power per cavity with about 10 MeV of acceleration per cavity, limiting their current handling to about 1 milliamp without energy recovery. Certain cavities such as the JLAB FEL injector quarter cryomodule and the Cornell eight cell modules can surpass this limitation, but these modules are much larger and more expensive per MeV of acceleration in both procurement and in tunnel footprint required.

The peak current required by the insertion device is about 10^3 amps with the FEL-gain proportional to the electron density in the bunch[3]. Only 10% ΔI/I modulation on the current waveform is allowed during the interaction between the seed laser and the electron bunch. These modulations produce enhanced spontaneous radiation which competes with the seed laser to modulate the rest of the electron bunch; in the worst case, the spontaneous radiation produced by the charge density fluctuations may destructively interfere with or produce sidebands around the seed laser wavelength. The User community the WiFEL is designed to serve also expect very little variation in optical power just as they would receive from a synchrotron light source. This 10% ΔI/I limitation is exacerbated by the magnetic bunching chicanes which squeeze the bunches longitudinally after the injector to reach the necessary kiloampere levels in the undulators but can also cause sharp density spikes in the compressed bunch by amplifying existing longitudinal modulations. Gain factors can reach 10^6 for a two chicane system [4], Fig 1. To mitigate this effect, weak compressors are used, increasing the peak current required from the gun.

*Work supported under NSF Award No. DMR-0537588
#rlegg@src.wisc.edu

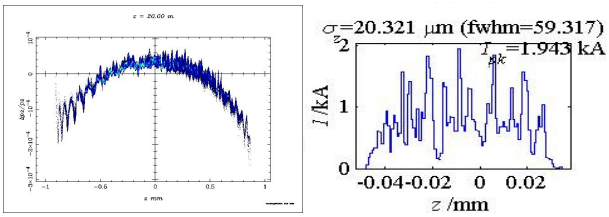

Figure 1. Non-linear energy modulation from ASTRA being converted to density distribution in LiTRACK simulation of magnetic compressors.

For a given photon energy produced by the FEL, the required electron beam emittance is inversely proportional to the beam energy, at least down to a beam energy of 50 MeV.[5] Since the beam energy is derived from the accelerator which is the largest cost in the project, the transverse emittance must be minimized to reduce the number of accelerator modules and the cost of the facility. Recent results at LCLS [6] suggest <1 mm-mrad is possible, but an emittance compensation scheme to correct all but the initial thermal emittance is mandatory and all elements in the injector need to be thoroughly tested for coupling and chromaticity.

These three requirements for a seeded FEL put tremendous demands on the accelerator's injector. They simultaneously require electron bunches with high peak current, low transverse emittance and specifically tailored longitudinal distributions. To meet those demands, we are proposing an SRF electron gun for application to a seeded FEL system. The superconducting rf gun is the newest technology with first operation of a gun at FZD in 2002[7]. It promises gradients of 40 MV/m and exit energies >4 MeV.

The superconducting rf gun we are proposing is a 200 MHz quarter wave resonator design. The University of Wisconsin has been doing extensive modeling of the electrical, rf and beam dynamics properties of the cavity for the last year and a half. The low frequency has several advantages. The device can operate at 4.2 K since the BCS losses go as the frequency squared. The accelerating gap is small compared to the rf wavelength making the device pseudo DC in performance. This minimizes the effect of phase slip as the bunch traverses the gap and produces a bunch with a flat momentum vs position profile.

DESCRIPTION OF ELECTRON GUN

The SRF electron gun design which has been developed by University of Wisconsin and Niowave is shown in Fig 2. The cavity has a number of unique design features. The cathode is warm with respect to the cavity allowing the use of an alkali stoichiometric cathode with a quantum efficiency orders of magnitude higher than a metal one. This greatly reduces the power and photon energy of the drive laser. This in turn reduces its cost and complexity, with the added advantage that the specular reflections of the drive laser from the cathode do not have enough energy to produce stray electrons from the metal surfaces in the cavity, reducing downstream halo. Critical gun parameters are shown in Table 2.

Table 2. Gun Parameters

Momentum at exit of gun	4.5 MeV/c
Peak surface magnetic field	93 mT
Peak electric field on cathode	45 MV/m
Bunch length at exit of gun	0.18 mm
Rf Power loss into Helium bath	39 Watts at 4.2 K

The design utilizes a coaxial cavity filter one half wavelength long behind the cathode with an impedance of ~22 ohms to provide an rf short circuit between the cathode and the cavity while still providing a thermal gap. The outer conductor of the coaxial cavity is niobium up to

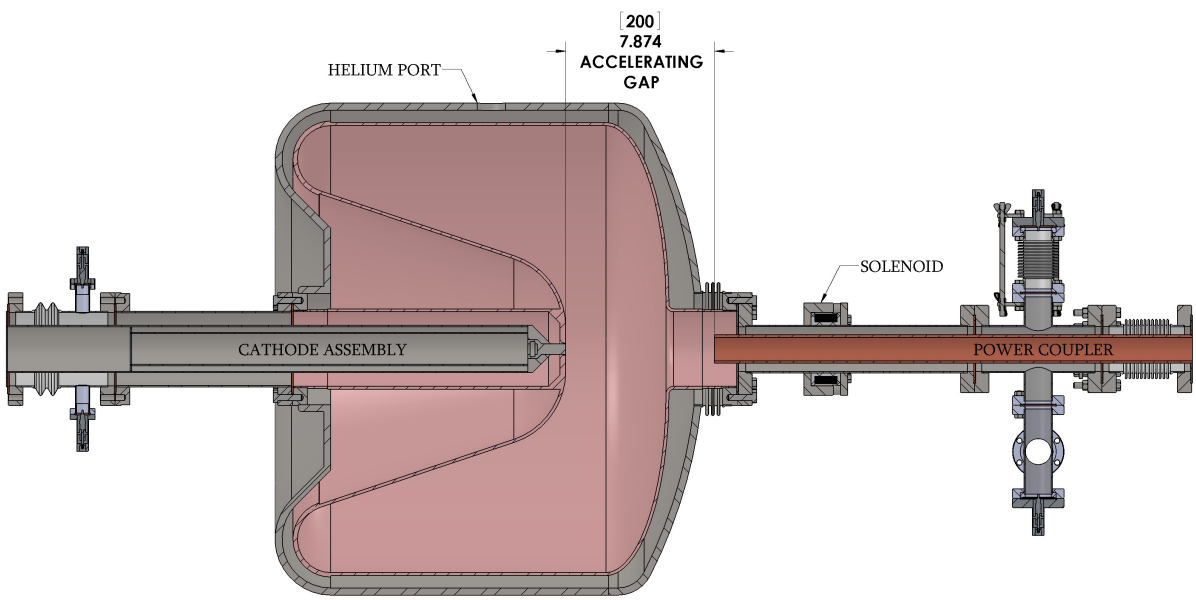

Figure 2: Quarter wave cavity design showing coaxial filter, warm cathode holder and rf power coupler.

where it mates with the stainless steel He dewar. Beyond the dewar the outer conductor becomes copper plated thin wall stainless steel which acts as the thermal break between the cold portion of the cavity filter and the room temperature portion where the rf probes, bias feed through, and alignment mount are placed. The inner conductor of the structure is made of copper plated stainless steel. It is cooled with liquid nitrogen flowing between the stainless tube and an inner liner. The LN2 reduces the radiation losses from the inner conductor of the cavity filter to the 4.2 K niobium outer conductor to less than 0.2 W; at 300 K the losses are ~30 W. The LN2 also cools the cathode holder to reduce the rf and laser heating and re-radiation into the main cavity from the cathode. The filter cavity is penetrated with rf probes to measure and provide a feedback signal for the cavity field. The fields in it are small, ranging from 60 kV/m at the shorted end to 350 kV/m at the transition into the cavity. Consequently, the rf heating in the walls in the normal conducting portions of the cavity filter calculated from Superfish are quite small, ~13.5 W, of which 10 W goes into the LN2 cooled portion of the inner conductor of the filter. The rf and laser heating in the cathode holder itself accounts for another 4 watts. This requires about 5 milliliters per second of LN2 flow to cool.

Superfish modelling indicates that in addition to the half wave coaxial cavity, a small capacitive gap is needed between the cathode holder and the cavity to minimize the radial variation of the z component of the electric field across the cathode face. This radial variation defocuses the electron beam as it leaves the cathode and degrades the downstream beam envelopes and emittance compensation. By placing a short 1 mm gap between the cathode holder and the cavity, the field is almost uniform across the face of the cathode. This desensitizes the solenoid tuning for emittance compensation.

The field map for the entire cavity is shown in Figure 3. An additional consideration was the mechanical deformation of the cavity due to vacuum loading. Finite element techniques were used to guide this process and resulted in the elliptically shaped wall on the anode end of the cavity and the thicker walled area on the cathode end of the cavity. In laying out the cavity, particular attention was paid to keeping the ratio of E peak to E cathode as low as possible and to minimizing sharp corners in the cavity which might enhance multipactoring.

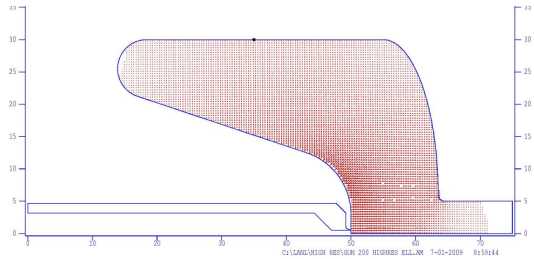

Figure 3 Electric field map from SUPERFISH for the cavity and cavity filter.

The issue of multipactor was considered for the coaxial cavity filter in a two prong manner. First simulations of the coaxial cavity were performed using FISHPACT to assess the susceptibility of the structure to multipactor. These show the cavity has no inherent problems with multipactor which might limit the field in the main cavity. We also decided to use the FZD design[8] for a cathode holder assembly which isolates the cathode electrically and allows an electrical bias to be put on it to suppress multipactor, Fig 4. This has also been suggested by BNL from their experience with SRF gun multipactor problems[9]. We also plan to use a dipole magnet on a

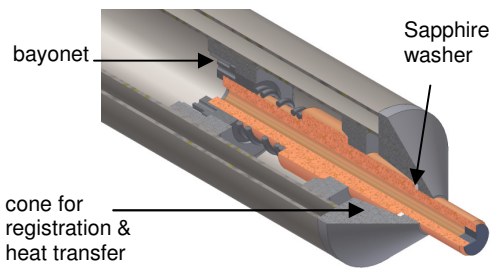

Figure 4. Cathode holder assembly

manipulator during rf conditioning, if necessary, which can be inserted into the cathode support tube behind the cathode to produce a magnetic field between the inner and outer conductor of the coaxial cavity to disrupt the orbits of potential multipactor electrons.

The gun design uses a superconducting solenoid for emittance compensation. The design has a ferrous yoke to shape the field from the superconducting coil pack. Additional mu metal shielding is also installed between the solenoid and the cavity. The solenoid has already been prototyped and tested, Fig 5.

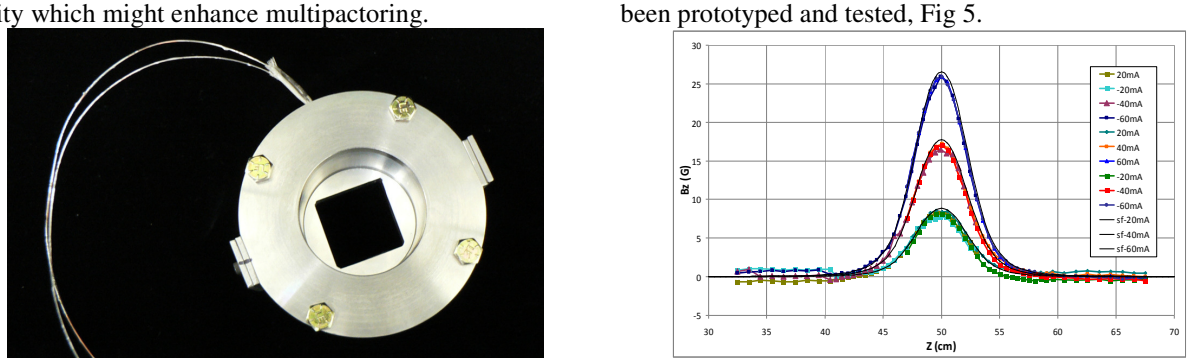

Figure 5. Photograph of SC solenoid assembly and field map

The gun uses a coaxial rf coupler as a power feed. The design can provide up to 10 kW of power to the gun based on Microwave Studio simulations, Fig 6. This is enough power for rf control with a 107 loaded Q and more than a milliamp of beam. The outer conductor of the coupler is copper plated thin wall stainless steel to supply the thermal break from the cavity to the warm rf cross. The inner conductor from the ceramic feedthrough is connected through a pressure contact to the inner conductor of the rf coupler in order to supply sufficient

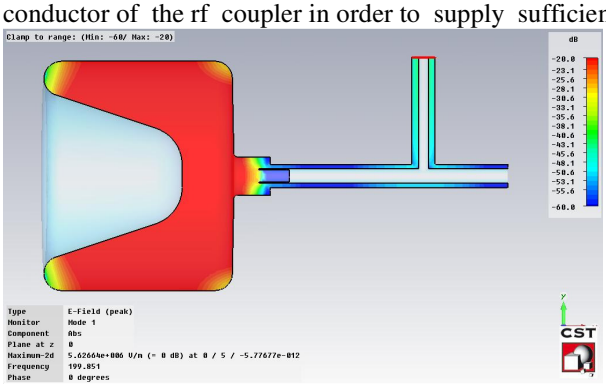

Figure 6. Microwave Studio E field map.

power to control the cavity with the desired loaded Q of 10^7. The pressure contact though allows the coupling point to be moved to vary the loaded Q of the cavity. This will allow the coupling to be varied to select the cheapest amount of rf power which can sufficiently control the cavity. The flange which mates the inner conductor of the rf coupler to the external beam pipe is actively cooled to sink the heat produced by the rf currents on the surface of the inner conductor and limit radiation losses from the coupler into the cavity to less than 1 watt. This design also exploits the inner conductor of the coupler as a beam scraper to prevent halo which originates in the high field region at the edge of the cathode holder +/-30 degrees from rf crest from propagating beyond the injector, Fig 7.

Self Inflating Bunch Formation

To meet the stringent requirements on the longitudinal distribution of the bunch produced by the gun, we propose to use self inflating (blow out mode) bunches for the FEL. Blow-out mode is a scheme in which a laser pulse much, much shorter than the final bunch length is used to create a charge pancake on the surface of the cathode which then expands under its own self space charge force to an ellipsoidal bunch with uniform charge density [10]. This technique has been successfully demonstrated at UCLA [11] and it avoids issues of laser/shaping performance or cathode emission uniformity in the production of an ellipsoidal bunch. In the 'blow out' process, many problems in the initial distribution are smoothed out, Fig 8. It also produces distributions which can be compressed and emittance compensated exceptionally well[12,13].

The downside to blow out mode is the charge density is dependant on the electric field as mentioned above and since the density in the charge pancake is very large, it requires a very high electric field on the cathode to produce the large peak currents after the bunch expands.

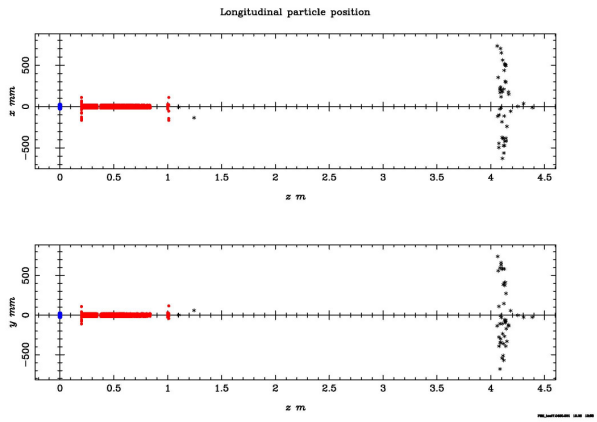

Figure 7. ASTRA[14] simulation showing lost halo particles on inner conductor of rf coupler in red. ~5 x 10^{-4} particles are transported.

The peak current can be increased by using a larger initial cathode spot, but the thermal emittance of the cathode becomes the limiting factor. The calculated limit for a peak current of 50 amps at 1 mm-mrad is 40 MV/m[15]. This is higher than can be achieved in a CW DC or NCRF electron gun and is one more reason the U of Wisconsin is proposing an SRF electron guns as a source for future FEL light sources.

The alternative to "blow out" mode is the laser shaping technique suggested by Yuelin Li[16]. This technique promises to produce ellipsoidal bunches with larger charge and lower thermal emittance than "blow out" mode can. Since the same physics is in place, charge

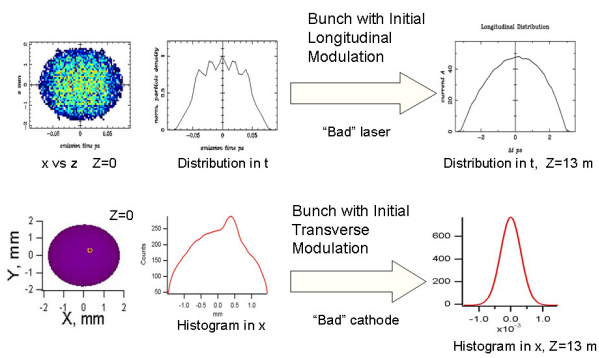

Figure 8. Blow-out mode smooths initial distribution errors

density and peak current still varies as the electric field squared using a shaped laser pulse, but the cathode spot and thermal emittance can be made smaller since the bunch charge can be produced gradually, rather than in a pancake. The SRF gun can also use this technique to produce bunches with peak currents much greater and

with lower emittance than possible with either the CW DC or NCRF gun.

ASTRA and IMPACT-T simulations of the proposed gun using 'blow out' mode show the gun can produce electron bunches which meet the requirements of a seeded FEL, Fig 9. The emittance compensation scheme[17] used is the same as LCLS is using successfully. In this scheme, the gun is followed by a high quality solenoid magnet which sets the emittance envelope going into the first linac section. 'Blow-out' mode imparts a large space charge induced dp versus z along the bunch which causes the bunch to lengthen as it moves away from the cathode. As the bunch does so, the peak current gets lower. To mitigate this process, the linac section is moved closer to the gun and the first cavity is phased to reverse the dp versus z. The gradient of the rf field must also be scaled to allow the emittance oscillation to be completed prior to the emittance being 'frozen' by the increased energy of the beam[18]. If the laser shaping technique described above can be applied, significantly better beam properties will result.

CONCLUSIONS

The University of Wisconsin has been working on the design for an SRF electron gun designed specifically to address the needs of a CW, soft x-ray, seeded FEL. The design utilizes the self inflating bunch scheme in order to produce ellipsoidal bunches with sufficiently smooth longitudinal distributions that downstream magnetic compression can be performed without longitudinal density spikes, detrimental to the User, appearing. The design includes a warm stoichiometric cathode and holder which reduces the required drive laser power, a coaxial filter to isolate the cathode holder thermally from the superconducting cavity, and a coaxial rf input coupler at the anode. The cavity is a quarter wave resonater with an accelerating gap much shorter than the rf wavelength. The injector meets the specification of a 1 mA average beam, at 50 amps peak at less than 1 micrometer-rad transverse slice emittance. By working backward from the requirements of the experimental User, through the accelerator, to the injector, the vision of the gun has been guided to this specific design. We have specifically addressed the issues of the coaxial filter, mechanical loading and thermal management of the cavity.

REFERENCES

[1] "Science and Technology of Future Light Sources – A White Paper", www.aps.anl.gov/Renewal/Science and Technology of Future Light Sources.pdf, Dec 2008

[2] "Next-Generation Photon Sources for Grand Challenges in Science and Energy", BESAC, May 2009

[3] R. Dei-Cas, Proceeding of 1992 EPAC, p 109, 1992

[4] R. A. Bosch, et al, PRST-AB, 11, 090702 (2008)

[5] C.W.Roberson and B. Hafizi, IEEE Journal of Quantum Electronics, Vol 27, No 12, Dec 1991

[6] R. Akre et al., Phys. Rev. ST-AB 11, 030703 (2008).

[7] D. Janssen et al., NIM-A, Vol. 507(2003)314

[8] V.N.Volkov, et al., Proc of RuPAC 2006, Novosibirsk, Russia (2006)

[9] A. Burrill, Proc. of ERL09, Ithaca, NY (2009)

[10] O.J. Lutein, et al., Phys. Rev. Lett., 93, 094802-1 (2004)

[11] P. Musumeci, et al., PRL 100, 244801 (2008)

[12] C. Limborg-Deprey, P. Bolton, NIM-A, 557 (2006) 106-116

[13] P. Emma, *Bunch Compression*, 17th Advanced Beam Dynamics Workshop on Future Light Sources, Argonne, Ill 1999

[14] K. Flottmann, http://www.desy.de/~mpyflo/.

[15] S.B. van der Geer, Proc of Future Light Sources 2006, DESY, Hamburg, Germany

[16] Yuelin Li, et al., PRST-AB, 12, 020702 (2009)

[17] L. Serafini and J.B. Rosenzweig, Rhys Rev E 55, 7565 (1997)

[18] R. Legg, et al., Proceedings of EPAC08, p 469, Genoa, Italy, (2008)

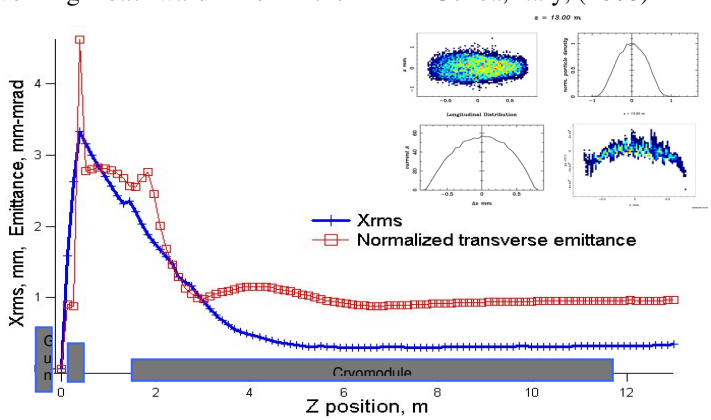

Figure 9. Beam envelopes for WiFEL injector using ASTRA

LATTICE DESIGN OF 2-LOOP COMPACT ENERGY RECOVERY LINAC

Miho Shimada[1], Yukinori Kobayashi
High Energy Accelerator Research Organization, KEK
1-1 Oho, Tsukuba, Ibaraki, 305-0801

Abstract

Compact Energy Recovery Linac (Compact ERL) is planned to construct in the KEK site as a test facility of 5GeV-ERL project. For achieving the high energy with a limited refrigeration power, the electron beam is accelerated twice by the same super-conducting cavity in a 2-loop design. At the branch of the two loops, a chicane is installed for flexibility of the ratio of the lower energy in the inner loop to higher energy in the outer loop. The angle of merger of the injection is 16 degree. The linear optics of the linear accelerator section is optimized for the two accelerator and two decelerator beams using the "dummy loop", which is used for determination of the twiss parameters of the entrance/exit of the two loops. Both inner and outer loop are designed to be an achromat and isochronous.

1. Introduction

5GeV energy recovery linac project has been promoted as the next generation light source, which is planned to be sited in KEK. For saving the building cost, site area and the refrigerating power, 2-loop scheme is a strong candidate for KEK project as well as others projects, such as Cornell Laboratory [1]. On the other side, the higher order mode (HOM), which accumulated in the superconducting cavity at lower current and the complicated beam dynamics are critical issues.

Compact ERL, which is a test facility of 5GeV-ERL, is using 2-loop scheme for achieving the higher electron energy with a limited refrigerating power. For optimization of the optical functions, the main linac section is should be careful because two accelerating and two decelerating beams pass though the same magnets. In this paper, we proposed the method of optimisation of optical functions and the simulation results for the Compact ERL.

2. Lattice layout of 2-loop Compact ERL

2.1 Main parameters and magnet layout

Figure 1 shows the schematic drawing of the layout of the Compact ERL. 500kV electron beam from DC photo cathode electron gun [2] is accelerated up to 5MeV at the injection section and lead to the main linac section at the merger section, which is composed of three bending magnets [3]. The electron beam accelerated up to 65 MeV passes though the inner loop and then is accelerated again up to 125 MeV. 125 MeV electron beam passing though the outer loop is decelerated twice at the main linac section down to 5 MeV. 5 MeV electron beam is lead to the dump with the extraction section. Total electron path length and the site area of the circulating section are 291.9 m and 47 m × 9.3 m, respectively. The lengths of the two main superconducting cavities are 8m and 10m, which contain four 9 cell-cavities in one cryostat and in two cryostats, respectively [4]. 60MeV acceleration per a turn will be upgrade to 120MeV in the future, in which the maximum electron energy is 245 MeV.

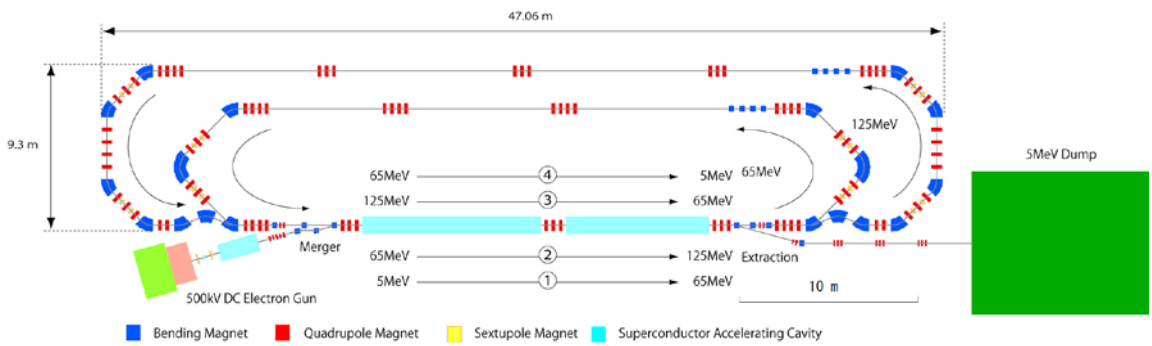

Fig. 1 : Schematic of 2-loop of compact ERL

[1] E-mail: miho.shimada@kek.jp

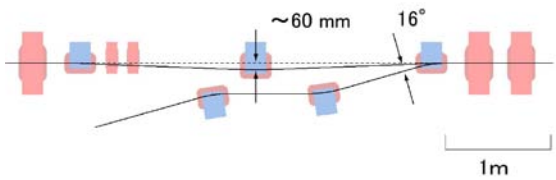

Fig.2 : Layout of merger section

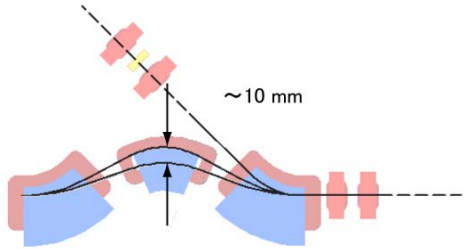

Fig.3 : Schematic drawing of energy branch chicane and the change in orbit.

2.2 Merger section

The schematic drawing of the merger section is shown in Fig.2. 5 MeV injection electron beam are merged at the chicane with three bending magnets at the angle of 16 degree. A chicane is installed for the circulating beam because to compensate the change in the orbit kicked by the merging bending magnet. The minimum electron energy of the circulating beam is 35 MeV and then the displacement of the orbit at the center of the chicane is about 60 mm.

2.3 Energy branch chicane

The energy ratio between the inner and outer loop depends on the injection and acceleration by the main linac, e.g., 65:125 and 125:245. The change in the ratio is 4%. For leading the full energy electron bean to the center orbit of the outer loop for both energy ratios, we installed the branch chicane at the entrance of the inner/outer loop. The schematic drawing of the branch chicane is shown in Fig.3, where the change in the orbit is enhanced. The change in the energy ratio, 4%, induces the orbital shift 10 mm at the center of the branch chicane.

3. Optical function of main linac

In the main linac, two cryostats of the superconducting cavity are between the three triplets, and then the two accelerator and two decelerator beams pass though the same triplets. The optical function should be designed not to be large at the last triplet just before the extraction section because the electron energy is low and the transverse emittance becomes larger at the loop sections. The focus strength of the triplets is optimized for the lowest energy beam. For the higher energy, the optical function is controlled by the twiss parameter at the boundary to the loop section because the focus strength is too small. The optical function is optimized using the SAD (Strategy Accelerator Design) and the two dummy loops, which consists of four quadrupole magnets, are inserted for calculation of the twiss parameters at the boundaries. The twiss parameters at the exit of the injector section is (βx, αx, βy, αy) = (13 m, -2, 0.7 m, 0).

Two results of the optical functions are shown in Fig.4. Figure 4 (a) is minimized the optical function at the main superconducting cavities. The optical function at the

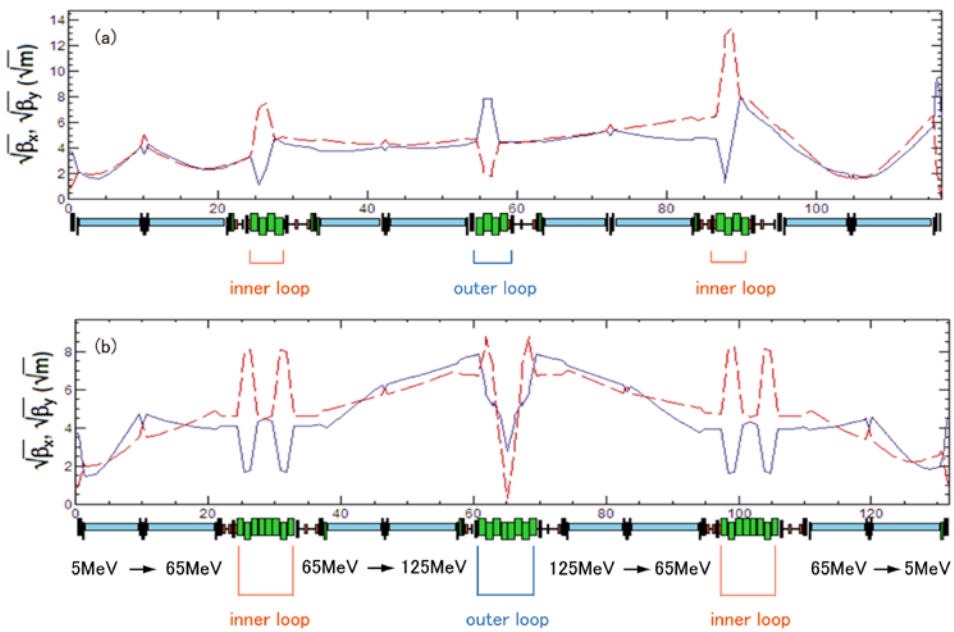

Fig.4 : Optical function of the main linac

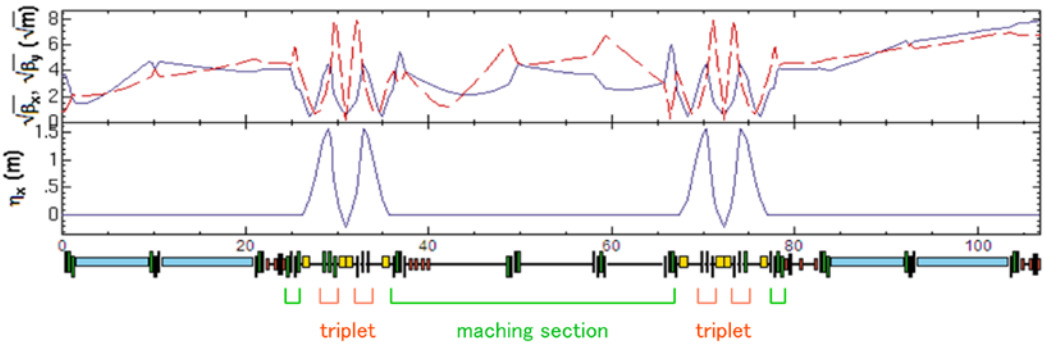

Fig.5 : Optical function of the inner loop

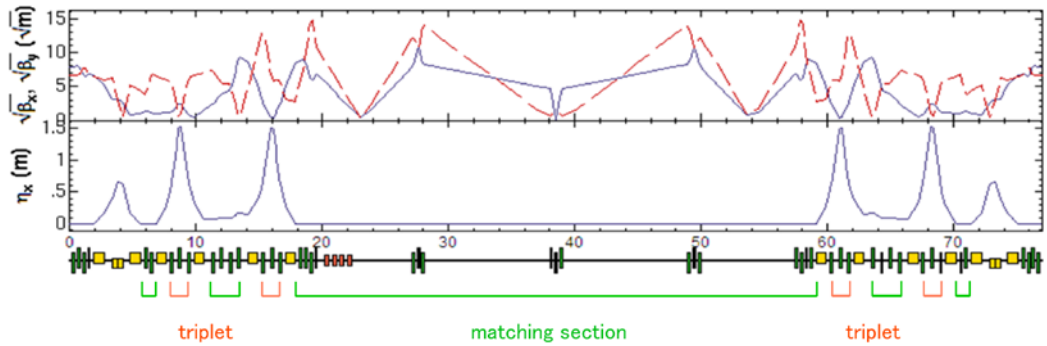

Fig.6 : Optical function of the outer loop

decelerator linac is larger than accelerator linac and the betatron function at the last triplet is over 90 m. In such a optics, the transverse beam size can be over the chamber size at the deceleration linac and extraction section. On the other side, in the symmetric optical function shown in Fig.4 (b), the betatron function is suppressed down to 20 m at the last triplet.

4. Optical function of inner and outer loops

The arc section of both inner and outer loops are designed to be an achromat and isochronous optics (R_{56} =0) for minimization of the transverse beam size and maintaining the longitudinal bunch length. The two arc sections are TBA like lattice consisting of four bending magnets with the bending angle of 45 degree in order to change R_{56} for bunch compression. The outer loop follows the branch chicane for electron beam with several energy ratios. The triplets between the bending magnets are used for the achromat and isochronous optics and the matching sections consist of several doublet and are used for matching the twiss parameter between the main linac section and arc section. For simplicity, the edges of the bending magnets are rectangle at the branch chicane and sector at the arc sections.

Examples of the optical functions of the inner and outer loop are shown in Fig.5 and Fig.6, respectively. The twiss parameters at the boundary are the same with the Fig.4 (b). The optical function has a flexibility over all and we can find several optical function.

5. Summary

We report the strategy of the liner optical function and the first optical function of the 2-loop Compact ERL. At first the optical function of the main linac is optimized by using the dummy loops. At the loops, the triplets are calculated for an achromat and isochronous optics, and finally the matching sections are used for matching between them. In ERL optics, it should be caureful to pay attention that all electron beams with different energy pass though the same magnets with a reasonable optical function. In this paper, we showed the example of the symmetric optical function with low betatron function at the last triplet.

References

[1] G. H. Hoffstaetter et al. “Cornell ERL program”, in Proceedings of ERL09, 2009
[2] N.Nishimori, et al. “ JAEA/KEK gun status” in Proceedings of ERL09, 2009
[3] T.Miyajima, et al. “Tolerances for errors in ERL linacs” in Proceedings of ERL09, 2009
[4] H.Sakai, et al. “KEK ERL cryomodule development” in Proceedings of ERL09, 2009

UNDULATOR OPTIMIZATION FOR ERL BASED LIGHT SOURCES

Robert Rossmanith, Research Center Karlsruhe, Axel Bernhard, Sandra Ehlers, Golo Fuchert, Peter Peiffer, Tilo Baumbach, University Karlsruhe, Germany

Abstract

Conventional synchrotron light sources operate with currents between 200 and 500 mA. The maximum obtainable brilliance is 10^{21} photons per sec, per 0.1 bandwidth, per mm^2 and per mrad^2. In this paper the brilliance of photon beams generated by ERL`s are compared with the brilliance produced by synchrotron radiation storage rings.

COMPARISON OF THE AVERAGE BRILLIANCE OF ERL BASED LIGHT SOURCES WITH CONVENTIONAL 3RD GENERATION SOURCES

The wavelength λ emitted from a planar undulator is

$$\lambda = \frac{\lambda_u}{2n\gamma^2}(1+\frac{K^2}{2}) \qquad (1)$$

λ_u is the period length of the undulator, γ is the beam energy divided by the electron rest energy, n is 1, 3, 5,…. and K is

$$K = 0.935.\ B[T].\ \lambda_u\ [cm] \qquad (2)$$

B is the maximum magnetic field in Tesla.

PETRA III is the synchrotron light source with the at the moment highest design brilliance of about 10^{21} photons per sec, per 0.1 bandwidth, per mm^2 and per mrad^2 (photon energy circa 10 keV). The minimum gap width of the PETRA III undulators is 9.5 mm, the period length is 23, 31.4 or 29 mm, the total length of one undulator is 2 or 5 m [1]. The design horizontal emittance is 1 nm, the design vertical emittance is 0.01 nm. The total beam current is 100 mA [2].

In ERL based sources the electron beam is produced in electron guns. In most of the designs the normalized emittance of the gun is both horizontally and vertically identical and in the order of one to several µm. Adiabatic damping reduces the emittances to 0.6 nm at 2.5 GeV and 0.085 nm at 6 GeV when it is assumed that the normalized emittances are 1 µm. Fig. 1 shows the calculated brilliance curve [3] for a 2 m long undulator. The undulator parameters are the same as before for PETRA III: the period length is 23 mm, and the assumed k-value ois 2.2. For a better comparison the current is 100 mA.

Comparing the values obtained for the model – ERL with the PETRA III parameters fig. 1 clearly shows that for the given parameters the maximum achievable brilliance in an ERL is somewhat lower than in a storage ring. This is due to the different beam cross- sections In a storage ring the horizontal emittance is significantly higher and the vertical emittance is significantly lower than in an ERL. Only at higher beam energies (6 GeV and higher) the brilliance obtained with an ERL and the brilliance obtained with a storage ring are comparable.

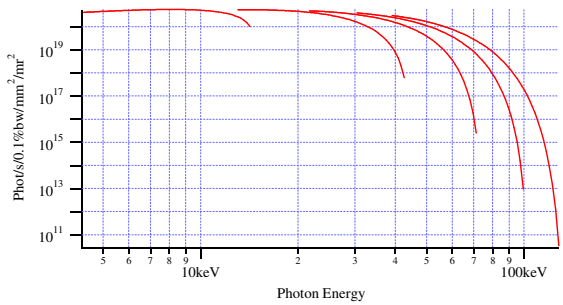

Fig. 1. Calculated brilliance of an ERL based light source. The beam current is 100 mA, the beam energy 6 GeV. The undulator length is 2 m, the period length is 23 mm and k is 2.2. Horizontal and vertical emittance are identical 0.085 nm (normalized emittance 1 µm).

The brilliance in an ERL versus beam energy is shown in fig. 2. The beam current is 100 mA and the normalized emittance is 3 µm. The undulator parameters from fig. 1 are used. At lower beam energies the beam dimension are larger and limit the brilliance. At very high energies the ERL brilliance would exceed the ERL brilliance.

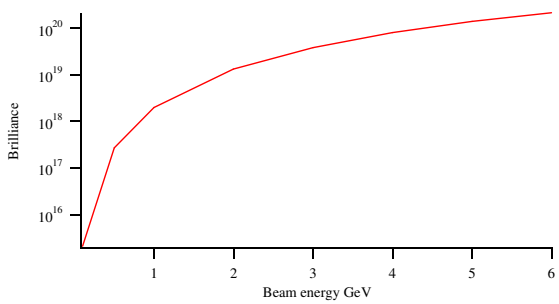

Fig. 2 Brilliance of an ERL for a 100 mA beam (photons per sec, per 0.1 % band width, per mm^2 and per mrad^2) . The gun has a normalized emittance of 3 µm, the undulator is 2 m long, the period length is 23 mm and K is 2.2.

In Fig. 2 it is assumed that a conventional undulator with a period length of 23 mm is used. The gap width is 9.5 mm and identical with the gap width of PETRA III. In the following it is investigated if special undulators tailored to the need of an ERL can increase the brilliance of an ERL at lower beam energies.

COMPARISON OF THE OBTAINABLE BRILLIANCE WITH SUPERCONDUCTIVE AND PERMANENT MAGNET UNDULATORS

As mentioned before the reference undulator for a storage ring is the PETRA III undulator, 2 m long with a period length of 23 mm and a K value of 2.2.

One big advantage of the ERL is the fact that the beam passes only once through the undulator or maximal only a few times. In the storage ring the same bunch passes the insertion device $1/\tau$ times per second, where τ is the revolution frequency of the electron beam. Therefore the gap of the undulator in an ERL can be much smaller. The following table shows at which gap width and which period length a superconducting undulator produces a K – value of 2.2 when it is assumed that the current density in the superconducting wire is 1000 A/mm^2 [4].

Table 1: Gap and period length for a superconducting undulator with K = 2.2, current density 1000 A/mm^2

Gap width [mm]	Period Length [mm]	Max. Field in Tesla
1	9.1	2.6
2	10.8	2.2
3	12.3	1.88
4	13.8	1.68
5	15.3	1.54
6	16.6	1.41
9.5	21.0	1.13

The gap defines both the maximum brilliance and the maximum photon energy. This is shown in fig. 3. In fig. 3 a beam energy of 2 GeV in an ERL is assumed. The electron source has a normalized emittance of 3 µm and the beam current is 100 mA. The brilliance is calculated for a gap width of 1, 4 and 9.5 mm. The length of the undulator is 2 m. The period length and the field values were taken from Table I. The successful operation of a superconductive undulator with a gap width of 2 mm in the Mainz Microtron MAMI was demonstrated several years ago with a beam energy of 855 MeV [5].

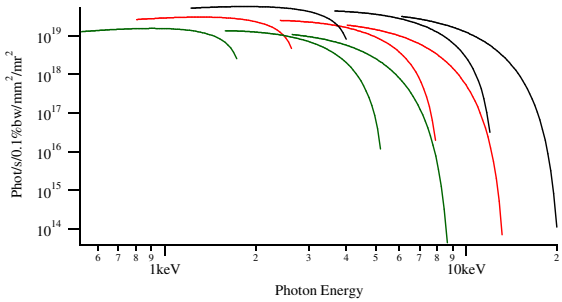

Fig.3 Brilliance curve obtained in an ERL with a 100 mA electron beam at a normalized emittance of 3 µm. The beam energy is 2 GeV. The maximum K value is for all three curves 2.2. The black curve is the brilliance for an undulator with a gap of 1 mm, the red one for a gap of 4 mm and the green one for a gap of 9.5 mm. Period length and field is taken from table I.

Fig. 3 demonstrates that small gap undulators have the advantage to increase the photon spectrum significantly. The influence on the brilliance is visible but not so significant.

This statement is further demonstrated in fig. 4. In this figure the brilliance of a 2 and 3 GeV ERL beam (100 mA) are compared. The black curve shows the brilliance produced by the 3 GeV beam with an undulator gap of 9.5 mm and the red one the brilliance produced by a 2 GeV beam with an undulator gap of 1 mm. In both cases K = 2.2. The values for the period length of the undulator and the field strength are taken from Table I. The normalized emittance is 3 µm. Both curves are almost identical demonstrating that an intelligent use of an undulator can dramatically reduce the costs of an ERL accelerator.

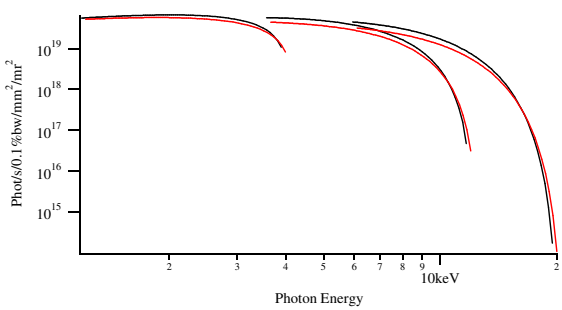

Fig. 4 Comparison of the achievable brilliances with an undulator gap of 9.5 mm at 3 GeV and an undulator gap of 1 mm at 2 GeV. The undulator parameters listed in Table I are used. Both curves are almost identical despite the significant difference in the beam energies.

UNDULATORS FOR ERL - BASED SYNCHROTRON LIGHT SOURCES

As mentioned in the previous chapter the cross-section of the beam in an ERL is round. Therefore the ideal undulator is a combination of two undulators: one with a vertical field and one with a horizontal field. The superposition of the two field components in the position of the beam can increase the field amplitude by about 40 percent. The basic idea is sketched in fig. 5 and was inspired by a similar concept developed for permanent magnet undulators [6]. The aim is to build an undulator which has a higher field for a given gap width compared to the values of the planar undulators listed in Table I. The realization of the sketched concept shown in fig. 5 is difficult from two points of view:

1.) The saturation of the iron
2.) The complex winding technique

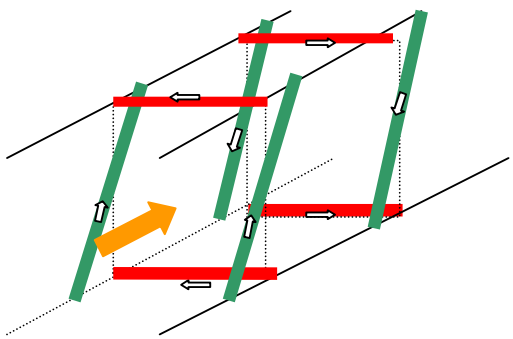

Fig. 5 Principal layout of an optimized superconducting undulator for an ERL based accelerator. The red wires produce a vertical undulator field and the green wires a horizontal undulator field. The yellow arrow marks the beam.

The basic idea is to produce a planar undulator field both in the horizontal and vertiical direction. The green wires in Fig. 5 produce a horizontal undulator field, the red wires a vertical undulator field. The green wires are tilted in order to enable the winding of the undulator.

The field in a superconducting undulator is defined by the magnetic material. The field produced by the superconductive wires saturate the poles of the undulator. One problem is that under certain circumstances the horizontal field can influence the vertical field and vice versa.

The second problem is that the simple winding schemes developed for superconducting undulators cannot be applied any more for such devices.

In order to solve these problems several technical solutions are at the moment under investigation.

THE USE OF LONG UNDULATORS FOR ERL - BASED SYNCHROTRON LIGHT SOURCES

One of the most demanding tasks is to build long undulators with 1000 and more periods. The line width of an undulator scales with 1/N where N is the number of periods. In order to obtain a line width of 10^{-3} 1000 periods are requires. Again this is only possible when the period is short (see Table I).

Different to FELs the radiation in an ERL driven undulator the wavelength of the radiation should be tuneable over a wide range. The tune ability requires that the field error of a superconducting undulator is low for all undulator currents. The measure for the field error is the so-called phase error. In a perfect undulator the electron trajectory and the photons are perfectly in phase and the coherent superposition of photons is perfect. Field errors change the phase relationship between electrons and photons leading to not – perfect at the superposition of photons. The consequence is a reduction of intensity. This is especially the case at higher harmonics (n = 5 and higher in equation (1)). Even if the phase error for the first harmonics is only several degrees the phase error for the nth harmonics is n times higher. Assuming for instance a phase error of 3 degrees for the first harmonics the phase error of the 5 th harmonics is already 25 degrees and leads to a significant reduction of photon intensity. In order to reduce the phase error in general the undulators have to be shimmed, which means that the phase errors are minimized.

Permanent magnet undulators are shimmed mechanically [7] by adjusting the poles. For a long time the shimming of superconducting undulators was difficult since the undulators have to be cooled to 4 degree Kelvin to measure the field. Afterwards the undulators have to be warmed up, shimmed, cooled down again and measured.

As a result the advantage that the superconducting undulator has shorter period lengths was compensated by the fact, that the shimming process was difficult. At the moment an attempt is made to simplify this process.

The new idea is based on Faraday`s law of induction. The principle is explained with the help of fig. 6.

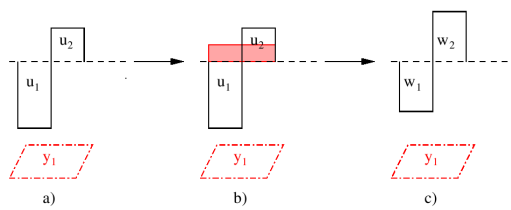

Fig. 6 The principle of induction shimming. The explanation is given in the text [8]

u_1 and u_2 are two neighbouring poles of the undulator. The sinusoidal field in one pole is approximated by a rectangular shape for the sake of simplicity. The integrated field is symbolized in the fig. 6 by a rectangle.

For the compensation of the field error a loop of superconductive material is attached in the gap at the surface of the undulator. The preferred material for the loop is a high temperature superconductor material like YBCO. The thickness of the YBCO material can be as low as 330 nm.

The way how the field compensation acts is explained in the following. Before the undulator is powered (zero undulator current) the current in the YBCO loop is zero (fig. 6 a). It is now assumed that the integrated field in the first loop is different to the integrated field of the second loop (fig. 6 b) when the undulator current is switched on. The non-zero integral field of the two poles leads to a current in the attached loop. Faraday`s law of induction requires that the induced current in this loop compensates the field difference.

In order to compensate the field error of the whole undulator the undulator surface is covered with overlapping loops as shown in fig. 7.

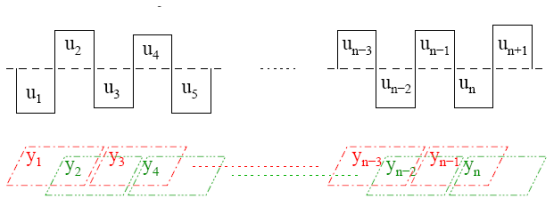

Fig.7 The array of overlapping superconductive loops attached to the undulator surface reduces the phase error for all periods without any mechanical shimming.

The basic idea of the induction shimming is that the high temperature superconductive loops can be fabricated by using lithography techniques and can therefore be produced with very high accuracy.

In a first demonstration experiment the concept of this idea was verified [9]. At the moment experiments are prepared to optimize this simple technique and to convert it into a technical concept.

SUMMARY

ERL and synchrotrons have the potential to produce photon beams with similar values for the brilliance at beam energies of 6 GeV and higher. At lower beam energies ERL based light sources suffer from the fact that in an ERL both the horizontal and the vertical emittance is identical and the emittance reduction due to adiabatic damping scales with $1/\gamma$. In a storage ring in general the vertical emittance is very small.

In order to increase the brilliance at lower beam energies undulators with high magnetic field and short period length can compensate this effect. This is possible with superconductive undulators using both the higher fields and the smaller gaps of this type of undulators. Since the electron beam only passes in an ERL once or at maximum only several times through the undulator a small gap does not affect the beam quality. The beam life time in synchrotrons is very sensitive to small gaps.

A further possibility to increase the brilliance is to build undulators with a combined horizontal and vertical field tailored to round cross section of ERL beams. These undulators are still in an early design phase.

ERLs can be operated with long superconductive undulator in order to increase the brilliance. One problem with long undulators operating at higher harmonics is the compensation of field errors. Recently a new technique was developed to shim the superconductive undulators in a passive way by an array of superconductive HTSC loops. First experiments showed that this is a very promising idea.

REFERENCES

[1] M. Bathelmess et al., Status of the PETRA III insertion devices, Proc. EPAC08, Genova, http://accelconf.web.cern.ch/accelconf/

[2] K. Balewski et al., Status of PETRA III, Proc. EPAC08, Genova, http://accelconf.web.cern.ch/accelconf/

[3] O. Chubar, P. Elleaume, Accurate And Efficient Computation Of Synchrotron Radiation In The Near Field Region, Proc. EPAC98 Sitges, http://accelconf.web.cern.ch/accelconf/

[4] H. O. Moser, R. Rossmanith, Magnetic field of superconductive undulators in comparison with permanent magnet undulators, Nucl. Instr. Meth. A490 (2002) 403

[5] M. Fritz et al., First experiments with a 100 period superconductive undulator with a period length of 3.8 mm, Proc. EPAC98, Stockholm http://accelconf.web.cern.ch/accelconf/

[6] G. Hofstaetter, these proceedings

[7] J. Pflüger, H. Lu and T. Teichmann, Field fine tune by pole height adjustment for the undulator of the TTF-FEL, Nucl. Instr. Meth., A 429:368-391, 1999

[8] D. Wollmann, A. Bernhard, P. Peiffer, T. Baumbach and R. Rossmanith, Induction Shimming: A new shimming concept for superconductive undulators, Phys. Rev. STAB 11, 1000702 (2008)

[9] D. Wollmann, A. Bernhard, R. Rossmanith, A. Grau, E. Mashkina, P. Peiffer, T. Baumbach, First experimental verification of the inductive shimming concept in superconductive undulators, Phys. Rev. STAB 12, 040702 (2009)

KEK ERL CRYOMODULE DEVELOPMENT

H. Sakai*, T. Furuya, E. Kako, S. Noguchi, M. Sato, S. Sakanaka, T. Shishido, T. Takahashi,
K. Umemori, K. Watanabe and Y. Yamamoto
KEK, 1-1, Oho, Tsukuba, Ibaraki, 305-0801, Japan

M. Sawamura
Japan Atomic Energy Agency (JAEA), Tokai, Naka, Ibaraki 319-1195, Japan

K. Shinoe
Institute for Solid State Physics (ISSP), University of Tokyo, Kashiwa, Chiba 277-8581, Japan

Abstract

Development of a SC Cavity Injector Cryomodule and Main linac Cryomodule for the compact ERL (cERL) [1] is being continued at KEK since 2006. Design of an injector cryomodule containing three 2-cell 1.3-GHz cavities for Injector Cryomodule and two 9-cell 1.3-GHz cavities for Main linac Cryomodule are almost completed. Status of R&D and design details are reported.

INJECTOR FOR CERL

An injector for cERL is required to accelerate a CW electron beam of 100mA to 10MeV. In this application, critical hardware components are not cavities but RF input couplers and HOM dampers. Several combinations of number of cavity and cells per cavity were examined, and a three 2-cell cavity system was chosen for cERL. Each cavity is drove by two input couplers to reduce required power handling capacity and also to compensate coupler kick. HOM coupler scheme was chosen for HOM damping, and 5 HOM couplers are put on beam pipes of each cavity. Because of simplicity cavities are cooled by jacket scheme. Basic parameters of the cavity are summarized in Table 1.

Table 1: Basic Cavity Parameters of injector

Frequency	1.3	GHz
Number of cell	2	
R / Q	205	Ω
Operating Gradient	14.5	MV / m
Number of Input Coupler	2	
Coupler Power	167	kW
Coupler Coupling Q	3.3×10^5	
Number of HOM coupler	5	
Operating Temperature	2	k

cavity

A 2-cell cavity is shown in Figure 1. It has a TESLA-like cell shape and larger beam pipe aperture of 88mm. Two fully equipped prototype cavities were fabricated, and the first cold test in a vertical cryostat was done in the last March. The cavity gradient reached 30MV/m with small electron loading (Figure 2). The reason of low Q value is due to losses at beam pipe flanges made of stainless steel. During the test, we observed some thermal instability (blue dots in Fig. 2), where both Q and gradient decrease slowly. It is well known due to the heating of pick-up antennae of HOM couplers. Heating of one HOM coupler was detected by thermometer at around 16 MV/m, but finally we could keep 16 MV/m for 6 hours.

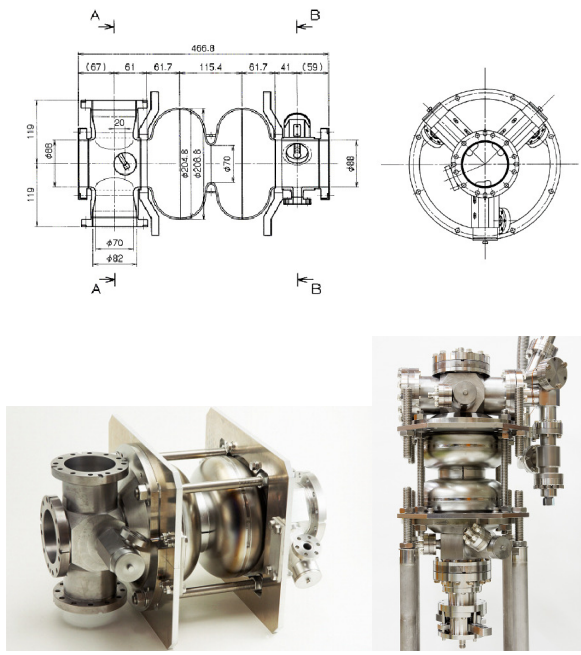

Figure 1: 2-cell Cavity

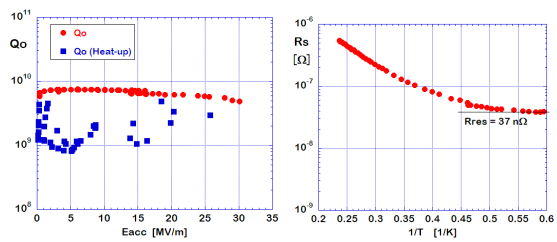

Figure 2: Vertical Test Results.

Input Coupler

RF input coupler is the most critical component in the high power application of the superconducting cavity. The most powerful CW coupler under operation is the KEK-B couplers, which has a coaxial disk type window

* sakai.hiroshi@kek.jp

developed for TRISTAN SC cavities [2]. We made scaled models to 1.3 GHz, as shown in Fig. 3 and 4. Impedance of coaxial part is 41Ω, and the outer diameter is 82 mm.

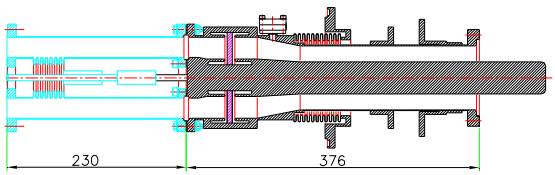

Figure 3: Input Coupler for Injector Cavities.

Couplers will be assembled to cavity in the clean-room before installation to a cryostat, so it should be short as possible. Then thermal intercept becomes difficult, and requires the 5k and 80k anchors at outer conductors. Inner conductors and the windows are cooled by water. High power test is scheduled in September.

Figure 4: Prototype Input Coupler

HOM Coupler

We decided to use HOM couplers instead of beam pipe HOM absorbers to damp HOMs, because absorbers are not well established in cold and they need extra drift space. Major HOMs are summarized in Table 2.

Table 2: Major HOMs

Mode	Frequency	R / Q	Measured Q_L
TE111	1.57GHz	0.59 Ω/cm^2	400
	1.63GHz	1.8 Ω/cm^2	350
TM110	1.80GHz	4.0 Ω/cm^2	1000
	1.88GHz	1.9 Ω/cm^2	900
TM011	2.28GHz	64 Ω	2000
	2.31GHz	12 Ω	1600
TM020	2.67GHz	0.4 Ω	
	2.69GHz	31 Ω	

TESLA HOM couplers are considered as the best choice, but it is well known that thermal instability appears above 10 MV/m in the CW operation. It is also well known that heating happens at pick-up antennae of HOM couplers, but it is not yet understood why niobium antenna becomes normal conducting. One may expect that if the current density at antennae is reduced, the threshold gradient increases. TESLA HOM couplers are modified by introducing second stub and a boss as can be seen in Fig.5 [3].

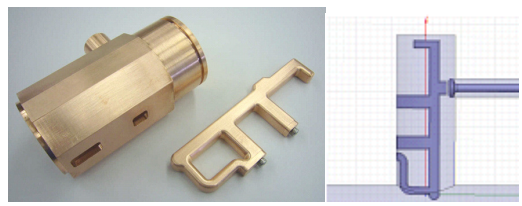

Figure 5: Two Stub HOM Coupler

Fig. 6 shows the H field distribution of the modified HOM coupler, the H field is reduced by a half, to 2000 A/m at 15 MV/m. The first cold test was performed with these HOM couplers. After some processing, we could rise the gradient to 30 MV/m. Heating appeared in one HOM coupler, but we could keep the gradient of 16 MV/m for 6 hours.

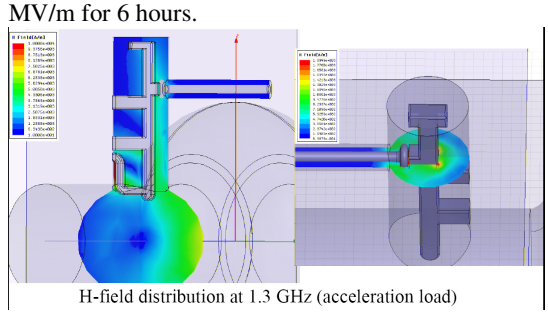

Figure 6: H-Field Distribution

Frequency Tuner

We will use Slide Jack tuners [4, 5] which are used in STF cavities as is shown in Fig. 7. Two pairs of wedge are set on both side of jacket cylinder flanges and driven by one shaft from outside of a cryostat. One piezo system is put in series with a slide jack tuner, and will be replaceable from a cryostat opening. Stroke of the tuner is listed in Table 3.

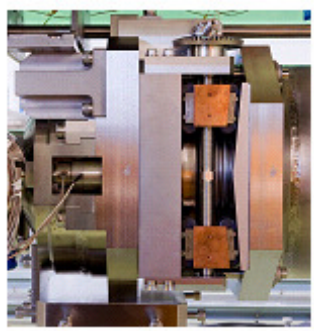

Figure 7: Slide Jack Tuner

Table 3:

	Type	Stroke	Δf
Mechanical Tuner	Slide Jack	1mm	1.3MHz
Fine Tuner	Piezo	4μm	2.6kHz

Cryostat

Fig. 8 and 9 show a cryostat containing three 2-cell cavities. All the cross section may become square. Cavities are dressed with He vessel made of Titanium, and magnetic shields are put inside of He vessel. The estimated cryogenic load in 100mA and 10MV operation is summarized in Table 4. As is seen from this table, it is critical to take dynamic load of input couplers and HOM extraction cables. They will be anchored to 4.5k reservoir panels put on both side of cavities, which works as a thermal shield as well. Because of this difficulty the operating gradient may be lowered.

Table 4: Cryogenic Load per Cavity

	2k		4.5k	
	Static	Dynamic	Static	Dynamic
Cavity	0	6W	0	0
Input Coupler	2W	4W	8W	16W
HOM Cable	1W	7W	5W	14W
Beam Pipe	1W	0	2W	0
Others	5W	0	10W	0
Total	9W	17W	25W	30W

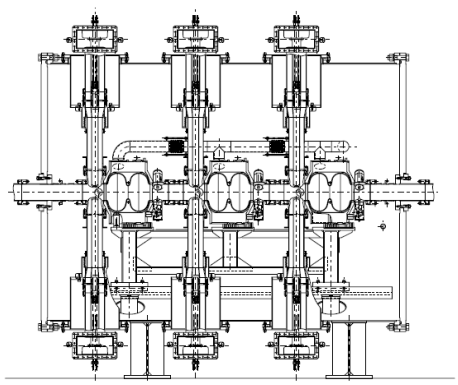

Figure 8: Injector Cryomodule

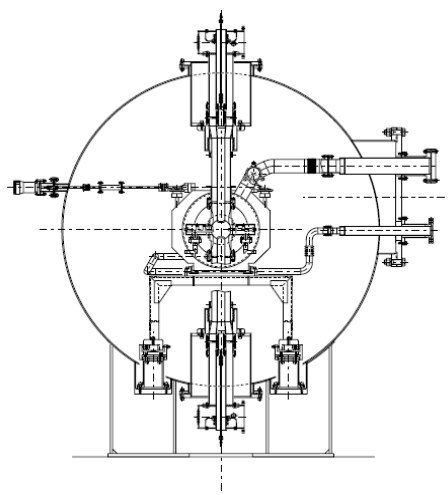

Figure 9: Injector Cryomodule

MAIN LINAC FOR CERL

Nine-cell SC cavities used for the main linac are under development to achieve a stable accelerating gradient of 15 - 20 MV/m under the beam of 100 mA. These cavities were designed [11] so that harmful higher-order-modes (HOMs) can be extracted through large beam pipes to the absorbers set on the 80K temperature. Thanks to the principle of the energy recovery, we can reduce the input power down to 20kW for each cavity. The cavity is cooled down to 2K by using jacket. Basic parameters of the cavity are summarized in Table 5. Because the heat load of HOM absorber is high, the sophisticated cooling is needed for main linac cryomodule.

Table 5: Basic Cavity Parameters of main linac

Frequency	1.3	GHz
Number of cell	9	
R / Q	897	Ω
Operating Gradient	15-20	MV / m
Unloaded Q	>1 x 10^{10}	
Coupler Power	20 (max)	kW
Coupler Coupling Q	0.5-2 x 10^{7}	
HOM load per HOM absorber	>100	W
Operating Temperature	2	K

cavity

Fig. 10 shows a conceptual view of the KEK-ERL model-2 cavity [6-8], which has been designed for cERL. The TESLA 9-cell cavity was modified to meet our requirements. Its features are the following.

- Cell shape is optimized and large iris diameter of 80 mm is chosen to suppress HOMs.
- Eccentric-fluted beampipe is adopted to suppress quadrupole HOMs.
- HOMs propagate through the large beampipes and are absorbed by HOM absorbers mounted on both sides of the cavity; one is 120mm as Large Beam Pipe (LBP) and the other 100mm as Small Beam Pipe (SBP) .

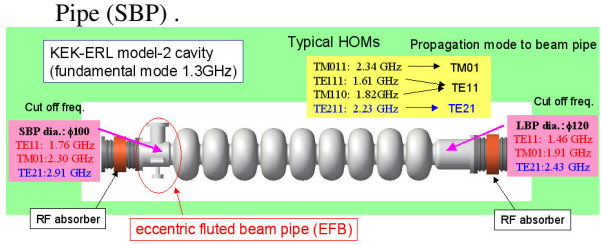

Figure 10: A conceptual view of the KEK-ERL model-2 cavity for the main linac. HOM absorbers are on the both sides.

In order to validate the cavity shape of KEK-ERL model-2, fabrication and surface treatment processes were tested on two single-cell Nb cavities, C-single and E-single, which are shown in the left figures of Fig. 11. C-single has the same cell shape as that of the central cell of the 9-cell structure. E-single has the shape of the end cell equipped with both beam pipes of the 9-cell cavity.

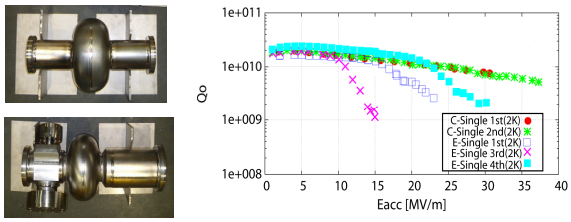

Figure 11: (left)two single-cell cavity one is C-single (top) and another is E-single cavity (bottom). (right) results of the vertical tests of single-cell cavities.

We have first fabricated two Nb single-cell cavities and tested them successfully [9]. The result of vertical tests shows the right figure in Fig.11. C-single and E-single finally satisfied the specification of 20 MV/m with the unloaded-Q of 1×10^{10}. Then, we fabricated a prototype 9-cell cavity, and carried out its vertical tests. The result of vertical tests is shown in Fig. 12. We successfully tested the prototype cavity up to a field gradient of 15 MV/m at 2K, and achieved an unloaded-Q of higher than 10^{10} at 10 MV/m in five vertical measurements. We also observed that the Q-value decreased due to field emissions above the field gradient of 10 MV/m.

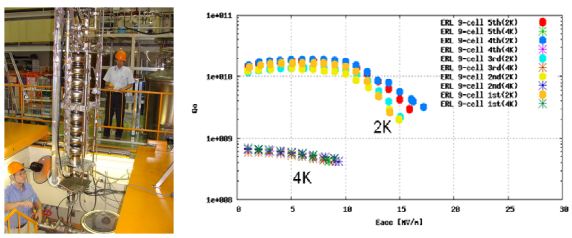

Figure 12: (Left) preparation for the vertical testing the 9-cell cavity. (Right) the first result of the vertical tests.

In order to investigate the cause of this problem in detail, we prepared cavity diagnostics by using rotating mapping system after 4th measurements; one is carbon resistor for measuring heat spot and another is Si PIN diode for measuring X-ray radiation map. Fig.13 shows one of the results of X-ray radiation mapping at 4th vertical measurement. We have strong radiation peak on 8-9 iris around 330° and also see the broad radiation traces on 1-6 irises on 4th and 5th vertical measurements.

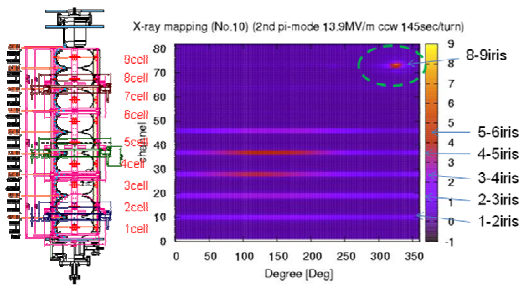

Figure 13: (Left) schematic view of the roating mapping system (Right) the result of radiation mapping.

After 4th and 5th vertical test, we investigate the inner surface by using the optical inspection camera [10]. We found the large tip on 8-9 iris around 150° as shown in Fig.14, which is just opposite side of 330° of the strong radiation point of green dotted circle of Fig.13. From these results, we thing tip of the iris point is one of the radiation sources and it is needed for recovering from field emission to grind this tip.

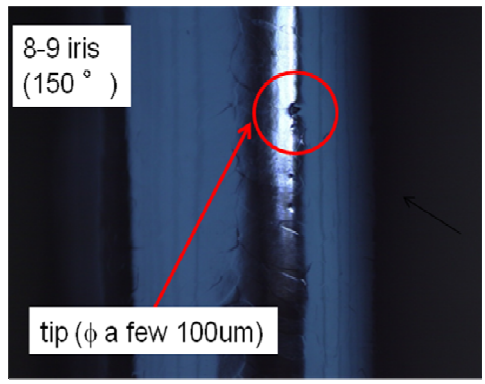

Figure 14: picture of the inner surface on 8-9 iris around 150° by using the optical inspection camera.

Input coupler

Minimum input power is restricted by the cavity detuning due to the microphonics from the cryomodule. We start to consider that the maximum detuning frequency is 50Hz caused by the microphonics. From these results, we determine that the maximum input power is 20kW and loaded Q is 2×10^{7} [8].

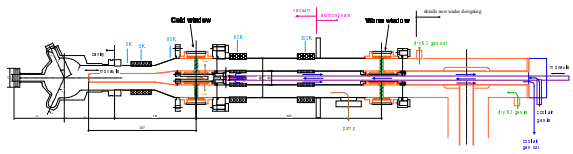

Figure 15: schematic view of input coupler for main linac.

Fig. 15 shows the schematic view of input coupler for main linac. The STF-BL input coupler was modified to meet our requirements [11]. Its features are the following.

- Change the impedance from 50Ω to 60Ω to reduce the heat load of inner conductor. Furthermore forced air cooling was applied to inner conductor.
- Purity of ceramic material was changed from 95%to 99.7% to reduce the heat load of ceramic.
- Cold ceramic size is same as warm one.
- Variable coupling was applied from $Q_L = 5\times10^{6}$ to 2×10^{7} for the short pulse conditioning of input power coupler in commissioning.

In order to check the heat load and temperature of input coupler by feeding the high power, first we made the test stand for testing the components of the input power couplers, especially ceramic windows and bellows, by delivering the maximum 30 kW CW average power from an IOT as shown in Fig. 16.

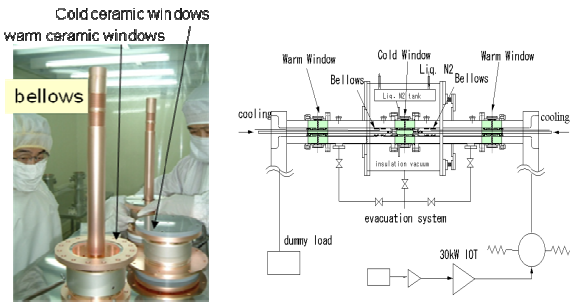

Figure 16: (Left) ceramic windows of input coupler with bellows. (Right) schematic diagram of coupler test stand.

In test stand, warm window with bellows sandwiches the cold window and power go through the 2 warm windows and one cold window. Temperatures of bellows and ceramic windows were monitored. In high power test, the sudden temperature rise was observed when the power increases up to 8kW and finally the cold ceramic window was broken as shown in Fig. 17. In low level test of cold window, we see the sharp resonance peak of 1.305GHz on the S_{21} measurement. And we found this peak is shifted to lower frequency side when temperature is increased. We also found that this frequency is same as the calculation of the unexpected dipole mode which stands on the choke of the ceramic window. From these results, this peak will induce the sudden temperature rise. In order to escape this dipole mode, we plan to modify the ceramic window by changing the thickness of ceramic.

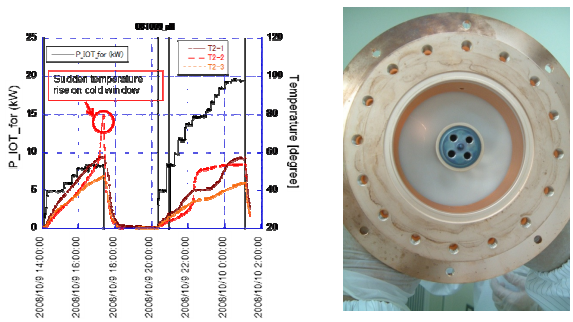

Figure 17: (Left) the measurement of temperature rise of warm ceramic windows (brown, orange line) and cold window (red line) corresponding to the input power (black line). (Right) broken ceramic cold window

HOM absorber

The HOM damper is also important for the ERL. HOM heat load is expected to be more than 100W. Therefore, HOM absorber material is set in the large beam pipes at the temperature of 80K. In order to investigate the enough absorption for high frequency at 80K, we measure the properties of absorption of the 8 kinds of ferrite and one ceramic. The detailed results will be shown in Ref.[12]. After the measurement, we decide to use new-type of IB004, which was used to the HOM absorber of KEKB, for the first prototype of HOM absorber for ERL. Fig.18 shows the design of the prototype of HOM absorber. Its features are the following.

- HIP bonding between ferrite and copper are applied to keep the strong connection
- Comb-type RF bridge is set to suppress the HOM come from the bellows
- Two kinds of thermal anchor at 80K and 5K were applied to absorb the heat load and reduce the static loss from HOM absorber to the cavity.

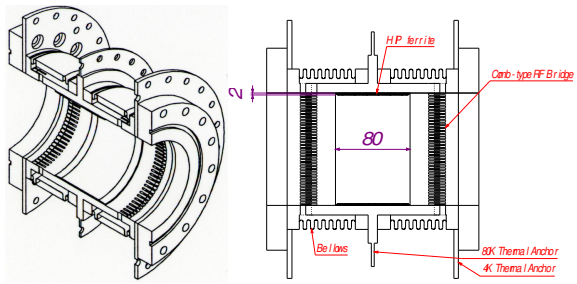

Figure 18: schematic view of HOM absorber

We plan the heat removal test by using this prototype,

Cryostat

Fig. 19 shows the design of the main linac cryomodule containing. Two cavities are set on one cryostat. Cavities are dressed with He vessel made of Titanium, and magnetic shields are put inside of He vessel. We also apply the enlarged jacket size (dia. 300mm) of cavity for smooth pumping of 2K by considering the heat load of 40-50W per cavity. One coupler feeds the RF power to one cavity. Three HOM absorbers set on the cryostat. The dynamic loss come from input coupler and HOM absorber is mainly absorbed 80K thermal anchor and by adding the 5K thermal anchor the static loss is reduced to below 1W to cavities at 2K. We also use the slide tuner to our cavity.

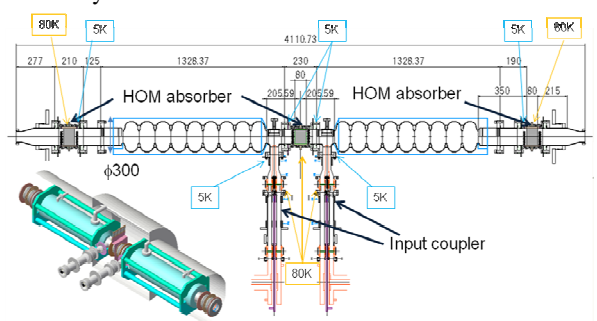

Figure 19: The design of main linac cryomodule.

SUMMARY

Development of Injector and main linac cryomodule are in progress. Assembly of cryomodule is scheduled from 2011 to 2012.

REFERENCES

[1] S. Sakanaka, et al., proc of PAC09, TU5PFP081.
[2] S. Noguchi, et al., "Couplers-Experience at KEK", Proceedings of 4-th SRF Workshop, KEK, 1989, KEK Report 89-21,1990, p.397-p.412.
[3] K. Watanabe, et al., "New HOM coupler Design for ERL Injector at KEK", Proceedings of 13-th SRF Workshop, Peking University, Beijing, China, (2007).
[4] E. Kako, et al., proc. of PAC09, TU3RAI04.
[5] Y. Yamamoto, et al., PAC09, TU5PFP075.
[6] K. Umemori *et al*., APAC2007, p.570.
[7] M. Sawamura *et al*., PAC'07, p.1022.
[8] H. Sakai *et al.*, Proc. ERL2007 ,p56
[9] K.Umemori *et al*., EPAC2008, p.925.
[10] Y. Iwashita et al., Phys. Rev. ST Accel. Beams 11, 093501 (2008).
[11] E.Kako *et al.*,Proc. of the 3rd Annual Meeting Particle Accelerator Society of Japan, Sendai, Japan, 2006, p136.
[12] M.Sawamura *et al.*. in these proceedings of ERL'09

ERL HOM ABSORBER DEVELOPMENT IN JAPAN

M. Sawamura #, JAEA, Tokai, Ibaraki, Japan
T. Furuya, H. Sakai, K. Umemori, KEK, Tsukuba, Ibaraki, Japan
K. Shinoe, ISSP, Univ. of Tokyo, Kashiwa, Chiba, Japan

Abstract

A superconducting main cavity for ERL has been designed and fabricated to reduce the HOM problem for the high current operation [1]. HOM power propagating along the beam pipe is damped at a HOM absorber installed between the cavities. The HOM absorber is cooled down to liquid nitrogen temperature in a cryo-module. The RF absorber material used for the HOM absorber is required to have good frequency and temperature properties. The frequency and temperature dependences of permittivity and permeability are measured for some ferrites and ceramics with a cold test stand consisting of a GM refrigerator. The parameters of the HOM absorber such as length, thickness and position are optimized by calculation of microwave simulation codes. Test models of the HOM absorber are being designed and fabricated to test the RF, mechanical, cooling and temperature properties.

PROPERTIES OF RF ABSORBER MATERIAL

Frequency and temperature properties of permittivity and permeability for several RF absorber materials were measured. Nicolson-Ross method [2] was used to measure the permittivity and permeability. The procedure of this method is followings.

1) Manufacture material samples to a coaxial shape to set in the 7mm-connector type sample holder.
2) Measure s-parameters of reflection and transmission for the sample with a network analyzer.
3) Calculate the complex permittivity and permeability from the reflection and transmission coefficients.

The samples must be cooled to measure the temperature property. A cold test stand with a GM refrigerator was used to cool the samples from room temperature to 40 K. This cold test stand consists of a GM refrigerator, a compressor, a vacuum chamber, a vacuum pump, and a temperature controller as shown in Fig.1. The GM refrigerator adiabatically expands the helium gas by a piston motion of a displacer. The compressor supplies the compressed helium gas to the GM refrigerator. The vacuum chamber prevents the sample from ice-up due to cooling with the GM refrigerator. The vacuum pump evacuates the air in the vacuum chamber. The temperature controller keeps the sample temperature constant

Figure 2 shows the inside of the vacuum chamber. The cold stage is connected to the cold head of the GM refrigerator and holds on the sample. The heater cable is winded around the cold stage and the heater power is adjusted to keep the temperature of the cold stage constant. The heater power is controlled by the temperature controller. The resistance-temperature detector measures the temperature of the cold stage and is used for the temperature control.

The cold stage is screened by the cylindrical cover wrapped with a super-insulator to prevent the radiation heat from the vacuum chamber.

Calibration of the network analyzer was done at each temperature of measurement. The procedure of the temperature property measurement is following.

1) Connect the calibration kit to the line from each port of the network analyzer and set on the cold stage..
2) Measure the s-parameters of the temperature dependence by cooling with the cold test stand.

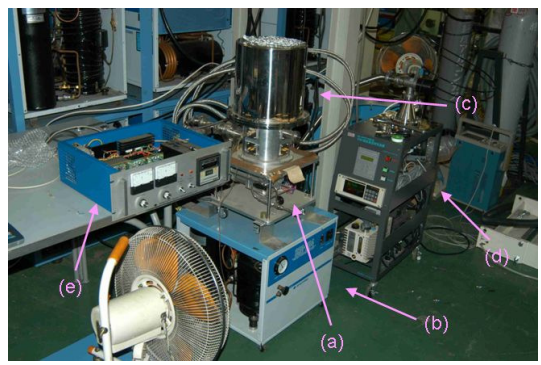

Fig.1 The cold test stand; (a) GM refrigerator, (b) Compressor, (c) Vacuum chamber, (d) Vacuum pump, and (e) Temperature controller.

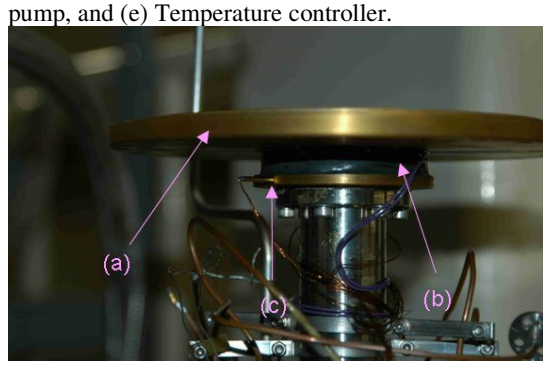

Fig.2 Inside of the vacuum chamber; (a) Cold stage, (b) Heater, and (c) Resistive-temperature detector.

#sawamura.masaru@jaea.go.jp

Table 1 List of ferrite and ceramic samples

Type	Supplier	Product
Ferrite	TDK Corporation	old-type IB004
		new-type IB004
	Trans-tech Inc	Co2Z
		Ferrite50
		TT2-111
		TT2-4000
		TT86-6000
	Nikko Co.	
Ceramic		SiC

3) Change the calibration kit to the open, short, load and through terminations and repeat above.
4) Calculate the calibration coefficients for each temperature with the measured s-parameters [3].
5) Measure the s-parameters of the sample at each temperature.
6) Calibrate the sample s-parameters with the calculated calibration coefficients.
7) Calculate the complex permittivity and permeability with the calibrated sample s-parameters.

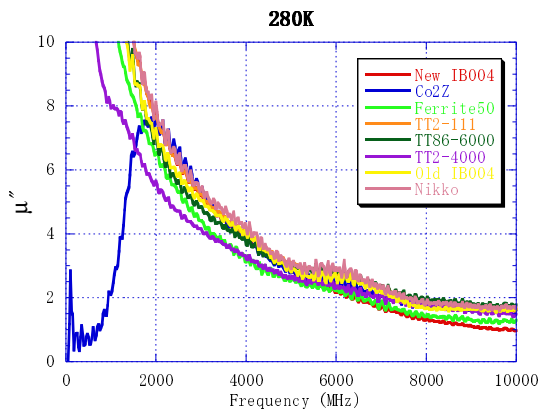

Fig.3 Permeability of ferrites as a function of frequency at 280K

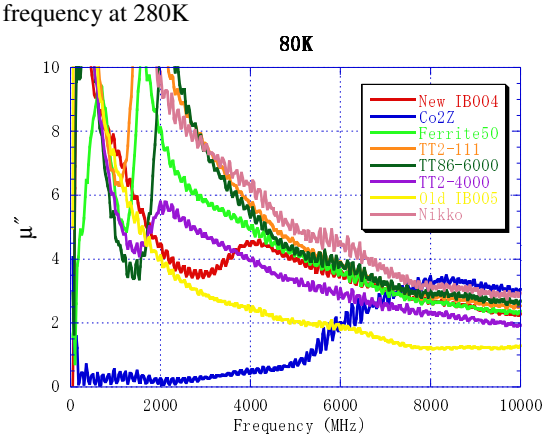

Fig.4 Permeability of ferrites as a function of frequency at 80K

The eight ferrite and one ceramic samples are measured as shown in Table 1. Figure 3 and 4 show the measurement results of ferrites at 280K and 80 K. The old-type IB004 supplied by TDK Corporation has been used for KEKB. The new-type IB004 is ridded of lead from the old-type IB004 to satisfy the RoHS criteria and adjusted to keep the property equivalent.

The temperature dependence of the new-type IB004 permeability is shown in Fig.5. The permeability is almost constant from room temperature to 150 K and decreases as the temperature becomes low.

Figure 6 shows the frequency dependence of permittivity of ceramic at 280K and 80K. At 280 K the permittivity decreases as the frequency increases and vanishes at high frequency. At 80 K the permittivity vanishes even at the low frequency. This means that the ceramic of SiC can not work as absorber at 80 K.

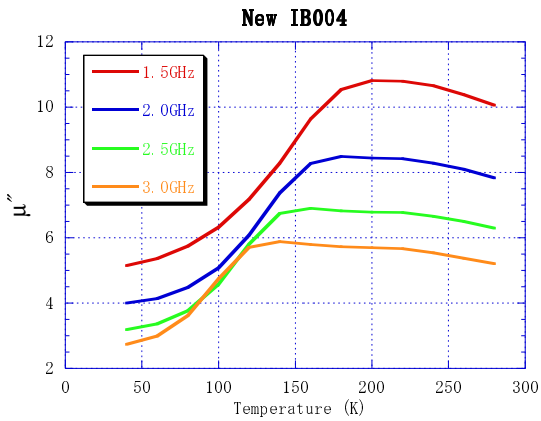

Fig.5 Temperature dependence of permeability of new IB004.

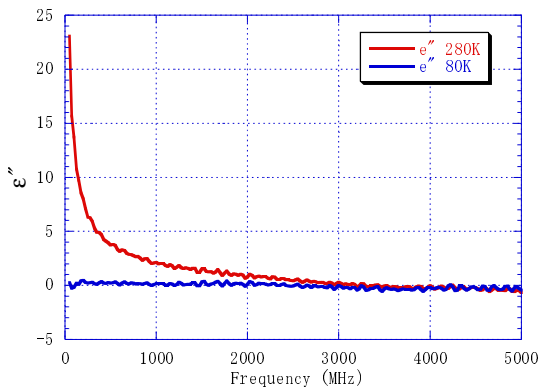

Fig.6 Permittivity of SiC as a function of frequency at 280K and 80 K

OPTIMIZATION OF HOM ABSORBER SHAPE

The HOM absorber shape was optimized to achieve the HOM loss as much as possible. The Q-value of the ferrite was defined to evaluate the HOM loss at the ferrite in a similar way of the cavity Q-value.

$$Q_{cavity} = \frac{\omega \times (Stored\ Energy)}{Cavity\ Wall\ Loss}$$

$$Q_{ferrite} = \frac{\omega \times (Stored\ Energy)}{Ferrite\ Loss}$$

When the ferrite Q-values are calculated with ferrite loss of CFISH calculation, they vary with the beam pipe length even though the ferrite condition is fixed.

The end of beam pipe determines the boundary condition of the standing wave. When the electro-magnetic wave transmits through the ferrite due to the insufficient absorption, the wave is reflected at the end of the beam pipe and passes through the ferrite again. The phases of the first and the second incident waves vary and the nodes of the standing wave shift with the beam pipe length. In our calculation the maximum Q-value is chosen as the ferrite Q-value while changing the beam pipe length with the fixed condition of the ferrite. The actual ferrite Q-value is expected to be lower than the calculated one at the worst condition of the beam pipe.

TM011 mode was used to calculate the ferrite loss with CFISH. The beam pipe length was varied up to 20 cm apart from the ferrite end by 1 cm step. The ferrite permittivity and permeability is ε_r=10.34-0.0046 j and μ_r=0.188-5.5 j of old-type IB004 at 2.2 GHz.

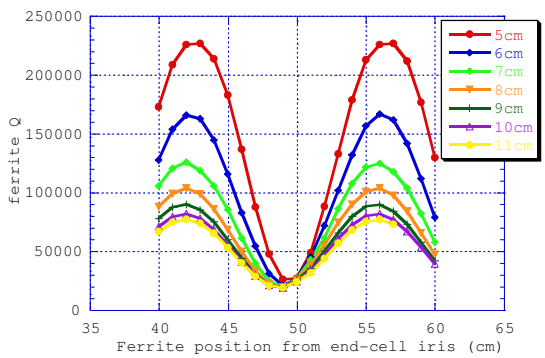

Fig.7 Ferrite length dependence of ferrite Q-value.

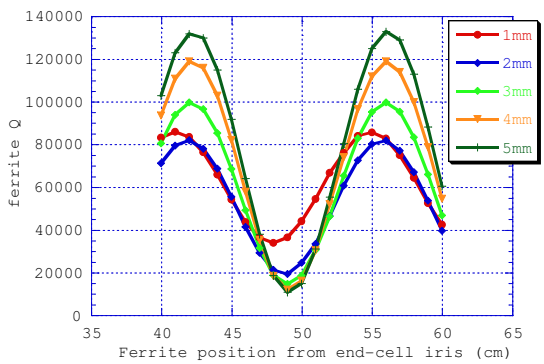

Fig.8 Ferrite thickness dependence of ferrite Q-value.

Figure 7 shows the ferrite Q-value as a function of the ferrite length. The ferrite Q-value decreases as the ferrite length increases. The minimum value and the ferrite length at this value are almost same. As the ferrite becomes longer, the difference between the maximum and the minimum gets smaller. The difference becomes less than 30 % over the ferrite length of 8 cm.

Figure 8 shows the dependence of the ferrite thickness. Though the thicker ferrite makes the minimum of the ferrite Q-value smaller, the difference between the maximum and the minimum becomes larger. This means that the thicker ferrite realizes the large absorption in good condition and small absorption in bad condition. The thicker ferrite increases the mismatch of the propagating HOM and reflection at the ferrite. This results in decrease of the ferrite loss.

Q-VALUE MEASUREMENT OF 9-CELL NIOBIUM CAVITY

The Q-values were measured to check the validity of calculation with 9-cell niobium cavity at room temperature. To search the optimum position of ferrite, the beam pipes were expanded and a ferrite sheet was installed inside the beam pipe. The loaded Q-values were measured by changing the position of the ferrite sheet. Figure 9 shows the measured and calculated loaded Q-values for the three modes of TM011 mode. While the position of the minimum Q-value is different for each mode, the position of the calculated minimum ferrite Q-value is almost same with the measured loaded Q-value.

The external Q-values can be calculated with the loaded Q-values [4]. The external Q-values for the TE111, TM110 and TM011 modes are shown in Fig. 10. The loaded Q-values were measured with four ferrite sheets of different length. The measured Q-values are similar regardless of the ferrite sheet length and almost agree with the calculated ones.

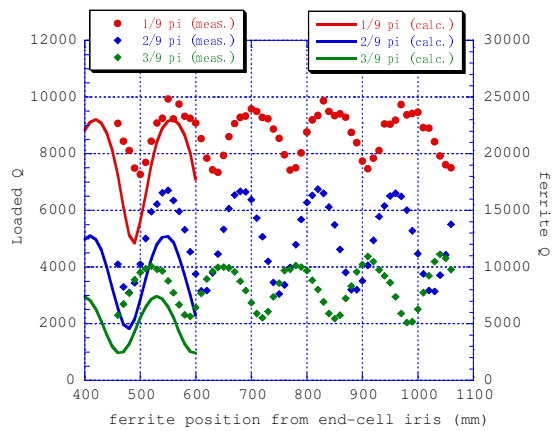

Fig.9 Measured load Q-values (dot) and calculated ferrite Q-values (line) as a function of ferrite sheet as a function of ferrite sheet.

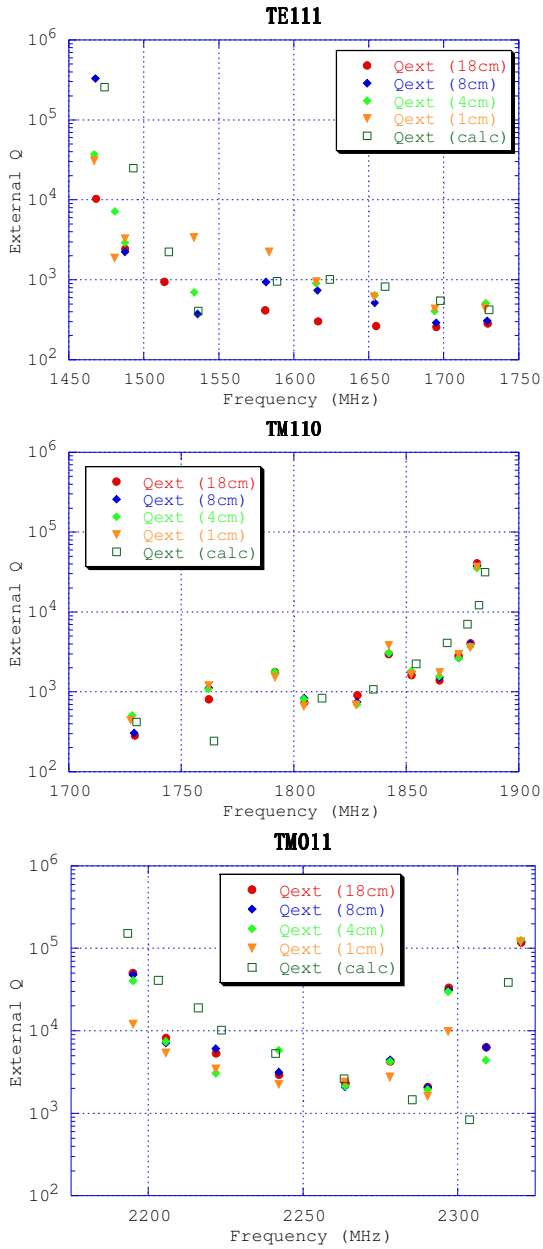

Fig.10 Measured and calculated external Q-values for TE111, TM110, and TM011 modes.

MODEL OF HOM ABSORBER

The model of the HOM absorber is under design and fabrication with the results of the above measurement and calculation. HIP (Hot Isostatic Press) can bond the ferrite and the copper base firmly. This HIP process is adopted to prevent from the ferrite falling off from the HOM absorber. The bellows are used to increase allowance of the flange connection and the heat shrink. The comb-type RF bridge is adopted at the beam pipe connected with the bellows [5]. This comb-type RF bridge has advantages of low impedance and small heat conductance compared with the finger-type RF connector. The layout of the HOM absorber is shown in Fig.11.

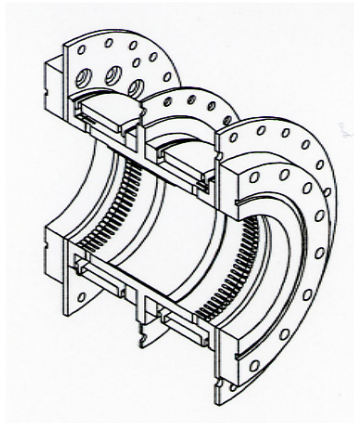

Fig.11 Layout of HOM absorber model

CONCLUSION

The frequency and temperature dependence of the RF absorber were measured. The new-type IB004 is chosen for our HOM absorber material due to good property at low temperature.

The calculation of the ferrite loss shows that 8 cm length and 2 mm thickness is enough to achieve large ferrite loss.

The frequency and temperature property of HIPped ferrite is going to measure. The HOM absorber models without and with ferrite are under fabrication. The HOM absorber without ferrite will be used for the test of cooling capability. The HOM absorber with ferrite will be used for the test of HOM damping property and ferrite mechanical tolerance for low temperature and heat cycle from room temperature to 80 K.

REFERENCES

[1] K.Umemori et al., Proc. APAC2007, 570-572, 2007
[2] A. M. Nicolson and G. F. Ross, IEEE Transactions and Instrumentation and Measurement, Vol. IM-19, pp.377-382, Nov., 1970
[3] Agilent AN 1287-3, “Applying Error Correction to Network Analyzer Measurements”
http://cp.literature.agilent.com/litweb/pdf/5965-709E.pdf
[4] M.Sawamura et al., Proc. PAC07, Albuquerque, New Mexico, USA, pp.1022-1024
[5] Y.Suetsugu, et al., Proceedings of the 5th Annual Meeting of Particle Accelerator Society of Japan and the 33rd Linear Accelerator Meeting in Japan, August 6-8, 2008, pp. 200-202 (in Japanese)

FAST FERROELECTRIC PHASE SHIFTER DESIGN FOR ERLs *

S.Yu.Kazakov,[a,b] S.V.Shchelkunov,[c] V.P.Yakovlev,[a,d] A.Kanareykin,[e]
E.Nenasheva,[f] J.L.Hirshfield[a,c]

[a]*Omega-p,Inc., 199 Whitney Ave., New Haven, CT 06511, USA*
[b]*High Energy Accelerator Research Organization, KEK, Tsukuba, Ibaraki 305-0801, Japan*
[c]*Beam Physics Laboratory, Yale University, 272 Whitney Avenue, New Haven, CT 06511, USA*
[d]*Fermi National Accelerator Laboratory, Batavia, IL 60510, USA*
[e]*Euclid Concept LLC, Solon, Ohio 44139, USA*
[f]*Ceramics Ltd., St. Petersburg, 194223, Russia*

Abstract

Fast phase shifters are described that use a novel BST ceramic that can rapidly change its dielectric constant as an external bias voltage is changed. These phase shifters promise to reduce by ~10 times the power requirements for the RF-source needed to drive an energy recovery linac (ERL). Such phase shifters will be coupled with SRF cavities so as to tune them to compensate for phase instabilities, whether beam-driven or those caused by microphonics. The most promising design is presented, which was successfully cold-tested and demonstrated a switching speed of ~30 ns for 77 deg, corresponding to <0.5 ns per deg of RF phase. Other crucial issues (losses, phase shift values, etc) are discussed.

INTRODUCTION

In ERLs there are several factors which significantly affect the required wall-plug power. With small beam loading, RF power requirements are determined by Ohmic wall losses, imbalance between beam currents, and microphonics. Compensation for the latter two typically requires a rapid change in coupling between the cavity and feeding line, and attendant high bandwidth, leading to need for significant additional RF power. If beam loading is not small, there are beam-driven phase instabilities for which compensation will also demand additional power.

Compensation can be either by changing the cavity geometry to offset detuning caused by phase instabilities and/or microphonics [1,2], and/or to apply a corrective phase shift to the reflected RF wave that is reintroduced to the cavity so as to cancel phase instabilities [3,4]. The first strategy is accomplished by internal or external motors, or fast internal mechanical piezoelectric tuners. The second approach utilizes fast ferrite or ferroelectric phase shifters that are external to the cryomodules, whereas piezoelectric and other mechanical tuners require operation at cryogenic temperatures and thus permit only limited access in the event of a failure. Further, piezoelectric devices have mechanical resonances which may interfere with control system performance if their own resonance frequency overlaps with the microphonics excitation to be controlled [5]. It is unknown if piezo-electric tuners are efficient enough at high frequencies.

*Work supported by DoE, Office of High Energy Physics.

Ferrite phase shifters [6,7,8] are presently limited in their response time to ~30 μs, while the required response time may be only a few μs. The limitation comes mainly from the eddy currents in the ferrite material [7].

Need for μs response time is dictated by the phase and amplitude stability requirements of ~ 0.06 deg and 3e-4, as cited for the Cornell ERL [9]; requirements are similar for the electron cooler project at BNL [10]. The gain in the control feedback loop should be high enough, and its bandwidth wide enough, to insure this high degree of stability. This translates to a bandwidth of about 1 MHz, and rules out contemporary ferrite tuners.

The authors have studied several designs for a fast electrically-controlled ferroelectric phase shifter for ERL applications. The device is to allow changing the RF-coupling during the cavity filling process in order to effect significant power savings, and also to provide rapid compensation for beam imbalance and allow for fast stabilization against phase fluctuations caused by microphonics and beam-driven instabilities. This capability should allow a reduction by about an order-of-magnitude in the required power from the RF source.

POSSIBLE RF POWER SAVINGS

The RF power P_g required to maintain an accelerating voltage V is given by [11]

$$P_g = \frac{V^2(1+\beta)^2}{4\beta Q_0(r/Q)}\left(\left(1+\frac{I_{\mathrm{Re}}(r/Q)Q_0}{V(1+\beta)}\right)^2 + \left(\frac{Q_0}{1+\beta}\left(\frac{\omega_0}{\omega}-\frac{\omega}{\omega_0}\right)-\frac{I_{\mathrm{Im}}(r/Q)Q_0}{V(1+\beta)}\right)^2\right),$$

where ω_0 is the cavity resonance frequency; Q_0 is it's unloaded quality factor; β is the coupling factor, for SC cavity $\beta >> 1$; r/Q is the cavity impedance; $I_{Re} = I(\cos\delta\varphi_a - \cos\delta\varphi_d)$, $I_{Im} = I(\sin\delta\varphi_a - \sin\delta\varphi_d)$, $\delta\varphi_a$ and $\delta\varphi_d$ are the average phases of the accelerating and decelerating beams compared with the RF phase; and I is the beam current. The value $\delta\omega = \omega_0 - \omega$ is determined by the amplitude of uncontrolled noise.

In [10,12], an example is given for a cooler linac having two cavities with $Q_0 \approx 4.5\times10^{10}$ at 2°K and $r/Q \approx$ 400 Ohms/cavity, I = 50mA×2 = 100 mA and $V \approx$25 MV.

(The beams go through the linac twice.) The intrinsic RF power required for is, for parameters listed above,

$$P_{\text{int}} = \frac{V^2}{Q_0 (r/Q)} = 9\,\text{W}.$$

If the accelerated and decelerated beams are well balanced, and the beams are in phase with the RF field, the required power is determined by the peak frequency variations caused by microphonics [2], namely

$$P_g = \frac{V^2}{4Q_l (r/Q)} \left[1 + \left(2Q_l \frac{\delta\omega}{\omega} \right)^2 \right],$$

where Q_l is loaded quality factor, $Q_l = Q_0/(1+\beta)$. One finds the optimal value of the loaded quality factor, $Q_{opt} = \omega/2\delta\omega$, and the minimum required power is proportional the peak cavity detuning, namely

$$P_g = \frac{V^2}{(r/Q)} \frac{\delta\omega}{\omega} = 0.55\text{kW} \times df\,[\text{Hz}],$$

where $\delta f = \delta\omega/2\pi$ is the peak microphonic cavity detuning in Hz. If, for example, the peak cavity detuning is reduced to 30 Hz (a typical value), the required input power would be ~17 kW for four 5-cell cavities.

While beam loss within reasonable limits gives no significant increase in required power, the phase error $\delta\varphi$ of the beams does, because in this case the beam introduces an additional reactance proportional to $\delta\varphi$, as can be seen from (1). The required power in this case is

$$P_g = \frac{V^2}{(r/Q)} \left(\frac{\delta\omega}{\omega} + \frac{(r/Q) I \delta\varphi}{2V} \right) = 0.55\text{kW} \times df\,[\text{Hz}] + 22kW \times \delta\varphi[^\circ].$$

With, for example, $\delta\varphi = 1^\circ$ and $\delta f = 30$ Hz, the required power would be about 40 kW. Obviously, it is crucial to provide means for compensation of phase instabilities to keep the RF-power requirements to a minimum.

FERRO-ELECTRIC MATERIAL AS BASIS OF THE PROPOSED DEVICE

Recently, ferroelectric (FE) devices for fast switching applications have received close attention, and are already used up to 100 kW peak in military systems [13], phased-array radars [14], and communication systems [15]. FE's have a dielectric permittivity $\varepsilon(\mathbf{E})$ that depends on electric field **E**, and can be rapidly altered by application of an external bias-voltage pulse. The response time would be limited by that of the external bias circuit. The minimum intrinsic switching time demonstrated is less than 1 ns [15]. Modern bulk ferroelectrics, e.g. $Ba_xSr_{1-x}TiO_3$ (barium strontium titanate or BST) with ε ~ 500, have sufficiently high electric-breakdown strength (100-200 kV/cm) and require an acceptable bias electric field (~20-50 kV/cm) to effect a 20-30% change in ε. Loss tangent for commercially-available samples is about ~1.5×10^{-3} at 1 GHz [14].

Euclid Concepts LLC recently developed and tested a modified bulk FE [16] based on a composition of BST ceramics, magnesium compounds, and rare-earth metal oxides. The availability of this FE already allows one to create a high-power RF phase shifter with the peak power required for ERL.

Properties of modified BST FE ceramic are in Table1.

Table 1

dielectric constant, ε	~460
tunability, $\varepsilon\partial/\partial E_{bias}$	> 2/(kV/cm)
intrinsic response time	< 10 ns
loss tangent at 1.3-1.4 GHz, $tg(\delta)$	2×10^{-3}
loss tangent at 700-900 MHz, $tg(\delta)$	1.1×10^{-3}
breakdown limit	200 kV/cm
thermal conductivity, K	7.02 W/m· ºK
specific heat, C	0.605 kJ/kg· ºK
density, ρ	4.86 g/cm^3
coefficient of thermal expansion	10.1×10^{-6} /ºK
temperature tolerance, $\partial\varepsilon\partial T$	3 /ºK

For the proposed devices, the FE ceramic is manufactured in the form of rings [Fig.1.a] or bars [Fig.1.b]. To measure the loss-tangent for ring-like samples, the setup shown in Fig. 2 was used [17]. Measurements on the bars were done with the bars suspended along the axis in a long metal pipe.

Figure 1a. FE ceramic ring Ø106 ×2.8×22 mm.

Figure 1b. FE ceramic bars (6 ×5×108 mm).

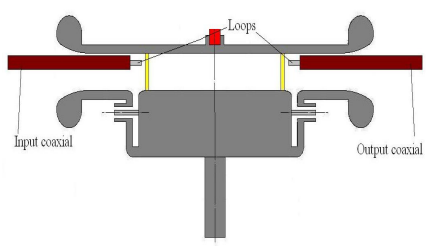

Figure 2. Setup to measure FE ring loss tangent.

Fig. 3 presents results of tunability measurements. The lower portion of the curve indicates low tunability at lower applied voltages. Presently, efforts are underway to reduce the loss tangent at 1.3 GHz, without undue sacrifice of tunability.

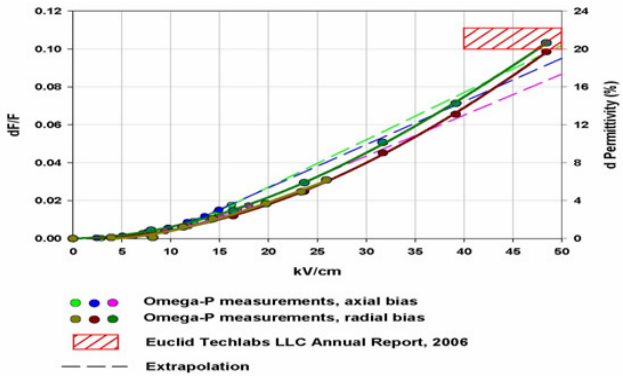

Figure 3. Tunability measurements on modified BST ring.

PHASE SHIFTER DESIGN

Three configurations have been considered: coaxial, planar/coaxial hybrid, and sandwich-in-waveguide; all for 500 kW pulse and 4-5 kW average powers, figures dictated by ILC parameters that we have chosen as the base line. Below we describe the last of these which was successfully built, and cold-tested.

The sandwich-in-waveguide configuration employs standard WR650 waveguide as a host for three sets of two narrow FE bars and two matching ceramic slabs (ε ~ 21), as shown in Fig. 4a. Each set rests on a metal plate, with a second metal plate above, as seen in Fig. 4b.

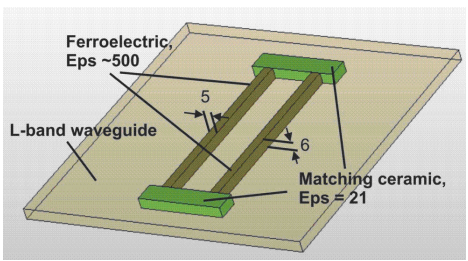

Figure 4a. Arrangement for one set of FE bars (grey) and ceramic slabs (green). Dimensions are in mm.

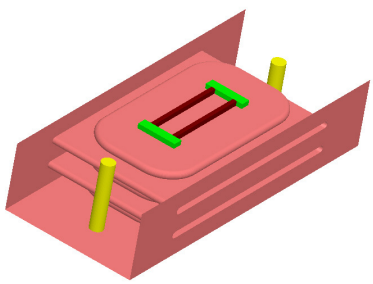

Figure 4b. WR650 waveguide with top removed to show three sandwiches and matching rod.

Alternate plates are joined to a feed-thru to provide the desired bias, while other plates are grounded. When assembled, dimensions are 8.2 × 16.5 × 30 cm. The mode spectrum is sparse, and can be controlled by changing the geometry. For matching to the structure, dielectric rods (alumina with ε ~9.8) are placed before and after the sandwiches. Frequency response is shown in Fig. 5.

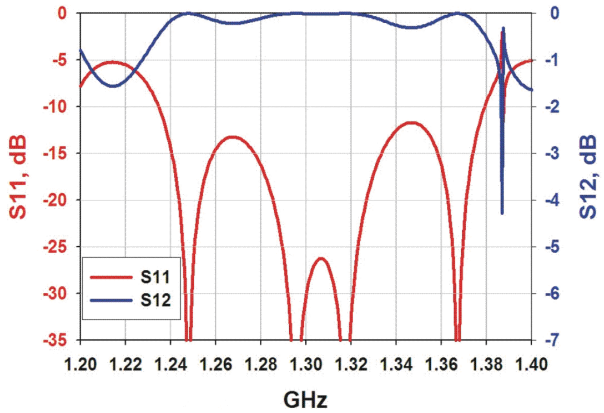

Figure 5. Frequency response for sandwich geometry with ε ~ 470; it is nearly the same for 470 < ε < 500.

Table 2 lists design parameters of the phase shifter for 500 kW of pulsed and 4 kW of average power.

Table 2

FE permittivity ε at V_{bias} = 0,	460
∂(phase)/$\partial\varepsilon$, deg	4
max. DC electric field, kV/cm giving Δ(phase) = 120 deg	15
total loss, %	$2.8 + 6\times10^{3}\tan\delta$
max. E-field in FE, kV/cm	3
max. E-field in ceramic, kV/cm	5.9
max. E-field in air, kV/cm	6.1
phase shift, deg, at 15 kV/cm bias	120
FE pulse heating with loss tan 5×10^{-4}	0.2 °K, for $\Delta\varepsilon$ = 0.6
FE av. heating with loss-tan 5×10^{-4}	0.9 °K for $\Delta\varepsilon$ = 2.7
FE pulse heating with loss-tan 2×10^{-3}	~0.4 °K for $\Delta\varepsilon$ = 0.6
FE av. heating with loss-tan 2×10^{-3}	~3.5 °K for $\Delta\varepsilon$ = 2.7

LOSS, PHASE SHIFT, AND SWITCHING SPEED MEASUREMENTS

Low-power RF measurements were made using only one of the three sandwiches in a waveguide that has the same width as WR650, but tapered to one-third the standard height, as shown in Fig. 6. The center electrode can be biased electrically.

Figure 6. A cross-sectional side-view of the one-third structure used for tests. Green lines represent matching slabs. FE rods are not seen in this cross-section.

The loss tangent of ferroelectric bars is measured for the uncoated bars (manufactured from the same batch used to make the bars coated with gold, as used in the 1/3 model. The value of loss tangent is determined to be ~2×10^{-3}, suggesting that the 1/3 scaled tuner model may suffer a transmission loss no better than ~0.7 dB. In actuality, the measured transmission is worse. The best value obtains only when one uses either freshly applied liquid indium-gallium or soldered the bars to the waveguide walls using In. However, we were not able to apply more than 4 kV to the soldered configurations; hence we discuss below

only the structures assembled with liquid Ia-Ga. It is found that in the configurations with fixed structure height, when the top and bottom walls are tethered by bolting to the side walls, transmission drops when the voltage increases [see Fig. 7a]. However, in a configuration where the top wall is resting without tethering on the ceramic bars under 200-400 lbs load, the transmission does not change much at all as shown in Fig 7b (in some cases, it becomes even higher). However, in general, the transmission level is lower because of leakage radiation through the gaps formed between unbolted walls. This suggests the presence of piezoelectric effects that shrink the bars and degrade the quality of the bar-wall surfaces contacts.

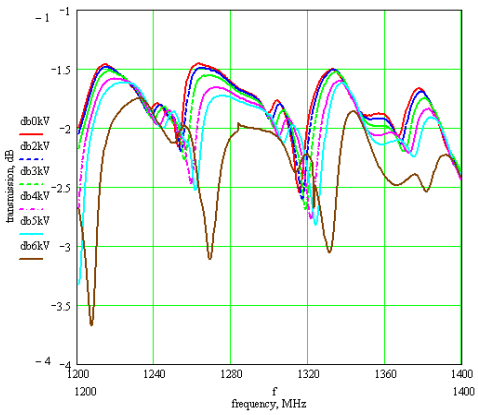

Figure 7.a. The transmission drops when the voltage grows in the configurations with fixed structure height [see the magnitude change at 1,3GHz]

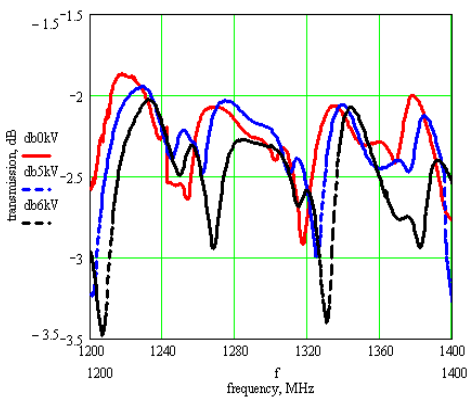

Figure 7.b. At 1,3GHz (middle of the plot), the transmission does not change so much (sometimes get higher) if top wall is resting under 200-400 lbs load on the ceramic bars, and thus the structure height is not fixed

It is anticipated that successful brazing of the ferroelectric and matching dielectric bars will eliminate losses beyond those in the bulk ceramics and metallic walls, as well as to lead to transmission being independent of applied voltage. As of now, several brazing attempts have revealed that the gold coating of the bar surfaces suffers badly when subjected to rapidly rising temperature and, in addition, the brazing atmosphere must be thoroughly controlled to avoid traces of oxygen. Tests were made with gold-plated ferroelectric bars and matching slabs; contact to copper walls was provided by liquid In-Ga alloy or In solder. Results of measurements of phase shift are presented in Fig. 8; these are seen to be in good agreement with simulations. Hysteresis is evident.

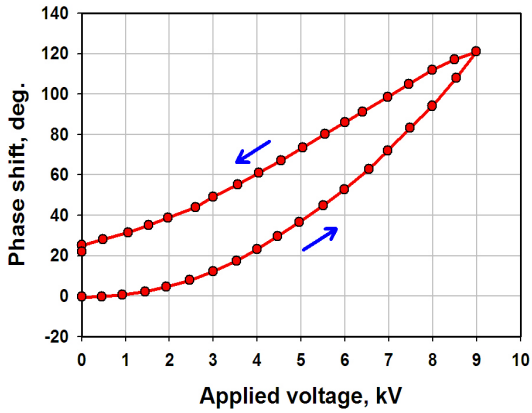

Figure 8. Measured phase shift of RF signal transmitted through one-third section *vs.* applied bias voltage.

A vital property of any tuner is its response time, which for many accelerator applications should be less than 100 ns. Measurements of response time were made using the arrangement shown in Fig. 9. The high voltage rise/fall times from the available pulse generator were in the range of ~100 ns (measured as the time difference from 5% to 95% of the voltage maximum). Switching speed measurements (each averaged over 16 shots) were processed by subtracting data with RF off from data taken with RF on, and are shown in Fig. 10.

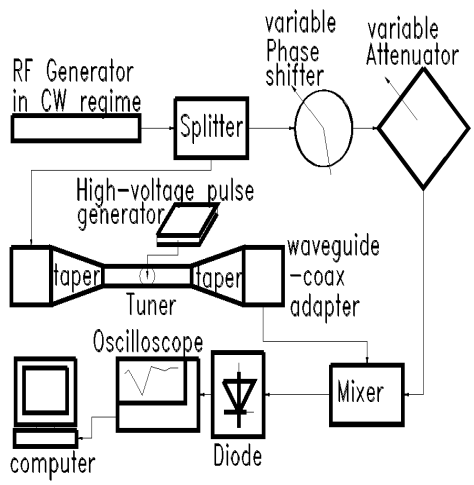

Figure 9. The signal from the RF generator at 1,290 MHz is split in two. One portion is directed through a phase shifter and attenuator directly to a mixer, while the second portion is fed through the tuner input port, passes through the tuner, picked up at the tuner output port, and then is fed to the mixer. The resulting signal from the mixer is detected by a diode and monitored at an oscilloscope, and also captured by a computer for further signal processing (mainly FFT).

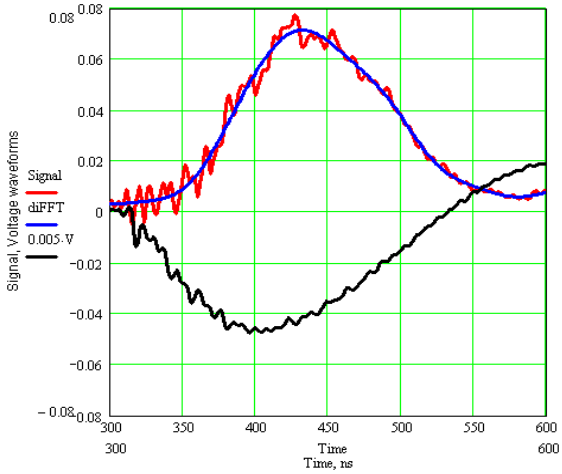

Figure 10. Time-response of phase shifter. Red curve (convex) is the difference between data with RF off and RF on. Blue curve is FFT/IFFT processed signal. Black curve (concave) is the high-voltage pulse with its peak value of ~9.7 kV. It is seen that the time delay between the peak voltage and the peak variation in phase is 28 ns. This value excludes delays in cables. The difference signal of 67 mV from the mixer corresponds to a phase change of 77º. (One horizontal division is 50 ns)

The difference signal of 67 mV from the mixer corresponds to a phase change of 77º. From these data, where the response time of the phase shifter is dominated by the 90 ns rise time of the voltage pulse, one can infer that the response time to a step function voltage would be equal to or less than the delay time, namely approximately 30 ns. This could be interpreted to correspond to an average switching rate of less than 0.5 ns for each degree of RF phase.

CONCLUSIONS AND PLANS

An RF-wave phase shifter based on a novel BST FE ceramic has been shown capable of delivering rapid phase switching (perhaps < 100 ns for shifts of ~180 degrees), while being suitable for high-power applications. That makes it an attractive candidate to externally tune the SRF-cavities for ERLs to reduce (at least by an order of magnitude) the RF-power requirements that arise because of phase instabilities of different origin, including microphoncs as one of many.

The conducted research has revealed that several material issues must be addressed, including brazing, provisions to limit breakdowns at high bias voltages, and re-designing the FE ceramic for L-band with low losses.

The planned work also includes: 1) further developing the design for planar-coax geometry because it promises simplicity (relative to other designs) and thus low cost; and 2) proceeding with high-power tests. These efforts are underway.

Lastly, we note that the tuner has been already connected to a 1.3 GHz cavity [that is a mock-up of the superconducting RF-gun cavity designed to be used in the electron cooling project at BNL, see [2] and confirmed the capability of tuning of its resonance frequency.

ACKNOWLEDGEMENTS

This work was supported by the Office of High Energy Physics, US Department of Energy. We also acknowledge the help of Timergali Khabiboulline (FNAL), Harald Hahn (BNL) and E.M. Choi (formerly of BNL).

REFERENCES

1. S. Simrock., et al., “First Demonstration of Microphonic Control of a Superconducting Cavity with a Fast Piezoelectric Tuner”, PAC2003, Portland, May 11-16, 2003, p.470.
2. M. Liepe and S. Belomestnykh, “Microphonics Detuning in the 500 MHz Supercondicting CESR Cavities,” PAC2003, Portland, May 11-16, 2003, pp.1326-1328.
3. Y. Kang, et al., “Reactive RF Tuning for Compensation of a Detuned Accelerating Cavity,” Linac 2002, Gyeongju, Korea, 2002, pp.733-735.
4. Martin Dohlus, DESY, Feb. 2004
5. T. Zwart, et al., “Optimal RF System For Lightly Loaded Superconducting Structures”, Proceedings of the 2004 FEL Conference, pp. 542-545
6. D. Valuch, et al., “First Results With A Fast Phase And Amplitude Modulator For High Power RF Applications,” EPAC2004, pp. 959-961.
7. D. Horan, et al., “Fast-Ferrite Tuner Operation On A 352-MHz Single-Cell RF Cavity At The Advanced Photon Source,” PAC2003, pp. 1177-1179.
8. B. Foster, et al., “High Power Phase Shifter,” PAC2005, PAC2005, Knoxville, May 16-20, 2005, p. 3123-3125.
9. V.P. Yakovlev, et al., “1.3 GHz Electrically-Controlled Fast Ferroelectric Tuner,” EPAC2006, Edinburgh, June 26-30, 2006, pp. 487-489.
10. I. Ben-Zvi, “The ERL High-Energy Cooler for RHIC”, EPAC2006, Edinburgh, 2006, pp. 940-944. *See also* R. Calaga, “SRF Cavities for High Current ERLs,” BNL, January 23, 2006
11. O.A. Nezhevenko, V.P. Yakovlev, “Cumulative Interaction in the Deflection Cavities of a High-Power Magnicon Amplifier,” *IEEE Transactions On Plasma Science*, vol. 28, No. 3, June, 2000, pp 542-549.
12. D. Wang, et al., “Design of a Superconducting Linac Cavity for High-Current Energy Recovery Linac Operation,” PAC2003, Portland, May 11-16, 2003, pp. 1300-1302.
13. L.C. Sengupta, “Bulk Ceramic Ferroelectrics and Composites: Manufacture, Microwave Properties and Applications,” IMS2000.
14. D. Webb, “Applications of Ferroelectrics in Military Systems,” IMS2000.
15. A.B. Kozyrev et al. Technical Physics Letters, v. 24, pp.19-25, (1998).
16. A. Kanareykin, et al., “Low-Loss Ferroelectrics for Accelerator Application,” EPAC2006, Edinburgh, June 26-30, 2006, pp. 3251-3253.
17. S.Yu. Kazakov, et al.,“First Measurements of RF Properties of Large Ferroelectric Rings for RF Switches and Phase Shifters,” PAC2007, Albuquerque, June 25-29, 2007.

Production of Thermal Positrons at ERL

Alexander Mikhailichenko
Cornell U., Ithaca NY 14853

Abstract. For generation of slow positrons at ERL, we are suggesting the usage of helical ~10T wiggler installed at 5 GeV route for generation of hard gammas. Despite the critical photon energy of radiation is about 170 keV only, the flux in hard part of spectra with photon energy $\hbar\omega > 2mc^2$ generated by 100 *mA* 5 *GeV* beam is big enough for generation of polarized thermal positrons with the rate ~10^{11} e^+ /sec.

OVERVIEW

ERL oriented generally for generation of electromagnetic radiation (SR/X-rays) for further usage this radiation for investigation in different sciences. One more application of ERL might be in creation of positrons by these radiations and usage of positrons instead of photons may open new possibilities in sciences.

Slow (thermal) positrons are a powerful instrument for investigation of properties of materials [1]-[7] due to their negative affinity to the media. Typically slow positron energy lies within <1 *keV*. Broad usage of positrons for this business slowed down by absence of intense source of low energy positrons with appropriate flux.

What for slow positrons could be used is described well in the references mentioned above. Among them are:

- Transmission and scanning microscopy; mostly promising emerges the possibility to switch between electrons/positrons for better resolution.
- Probing the surface by measuring the energy loss, diffraction and re-emission.
- Defects searching. As positrons could be trapped easily in volume defects even by single missed atom defect, theirs annihilation could be identified by measuring to point of creation of gammas created by annihilation process.
- Probing the Fermi-surface. Pair annihilation and following two-photon emission rate is proportional to the local electron density. The point of creation of two (or rarely three) photons could be resolved with adequate resolution ~nm^3 by measuring Doppler shifts in each photon and deflection from straight line.
- Positron holography.
- Some others, see [1] and references in there.

One way in use for positron creation is a beta decay of isotopes ^{22}Na(2.6 year half life time) or ^{58}Co (71day). The isotopes of ^{64}Cu (12.7 hour), ^{18}F (110 min), ^{11}C(20 min) are in use for these purposes also.

There is basically other practical way for getting the positrons in vast amounts: via electron-positron pair creation by gamma quanta (photon) of appropriate energy and flux in a field of nuclei. The photons in its turn could be generated either by beamstrahlung of electrons in the field of nuclei or by synchrotron or undulator radiation (SR or UR). SR or UR radiation to be effective must create the quantas of appropriate energy $E_\gamma \geq 2mc^2 \cong 1.22\,MeV$. Typically to be

effective, the energy of the primary beam must be high if *K*-factor is low, $K = eH\lambda_u / 2\pi mc^2$, (which corresponds to operation at low, even single harmonic) or the magnetic field value in wiggler must be high (operation at high harmonics) so the critical energy of SR $\hbar\omega_c = \frac{3}{2}\hbar c\gamma^3 / \rho \approx mc^2$ (where ρ stands for the local bending radius). Typically smaller the aperture of magnet-easier the required value of magnetic field could be achieved.

Typically insertion devices in damping ring have wiggler either with movable poles or SC wigglers with relatively large aperture. The last circumstance is a limiting factor for maximal field achievable in a wiggler. ERL (as well as any FEL) has one undoubted advantage over traditional storage ring: the insertion devices could have very small aperture, as there is no necessity for any kind of damping of betatron amplitude of injected beam. Although the same result could be achieved with usage of booster (pre-damping) rings, or injectors with very small emittance, ERL solves the problem with insertion devices mostly natural way.

THE CONCEPT

The concept we are suggesting is in line with our proposal [9]. The positrons generated by photons created in helical wiggler by energetic electron beam. In [10] the idea was developed to use strong planar wiggler installed in a damping ring for generation of hard photons, inspired by [9].

So basically we review this old idea for possible implementation at ERL. As the energy of beam is not as high as originally suggested in [9], the only way to get hard energy photons is to operate at high harmonics of UR. Spectrum of radiation becomes pretty much the same as for planar magnet, however. Although we are not interesting much in polarization of positrons, the overall polarization of the positron beam could reach ~30% if no special measures applied. As we are suggesting using collimator for the photons, polarization of gammas might reach 100% theoretically, but as we are not selecting these positrons in narrow energy margins, further enhancement of polarization is possible only by reduction of intensity.

SPECTRUM AND ENERGY SPREAD

Any wiggler installed to the beam line yields to the growth of energy spread and emittance. However if it is installed and the end of high energy branch, before entering the recuperation linac, the only important issue remains is the energy spread. We will see that emittance growth remains within acceptance of transporting optics. Let we calculate all this in more detail.

Cyclotron frequency for reference field is

$$\omega_0 = \frac{c}{\rho} = \frac{eB}{m\gamma} \tag{1}$$

Which for 10T comes to $\omega_0 = \frac{eB}{m\gamma} \cong 1.758 \cdot 10^{11} rad \cdot s^{-1} \cdot T^{-1} \cdot 10\,T \cdot 10^{-4} \cong 1.76 \cdot 10^8 rad \cdot s^{-1}$.

Local radius of curvature comes to $\rho \cong \frac{mc\gamma}{eB}$. Energy of quanta at first harmonic is $\hbar\omega_0 \cong 6.58 \cdot 10^{-22} \cdot 1.76 \cdot 10^8 \cong 1.16 \cdot 10^{-13} MeV$. Intensity of radiation could be expressed as

$$I = \tfrac{2}{3} mc^2 \frac{r_0 c \gamma^4}{\rho^2} = \tfrac{2}{3} \frac{e^2 r_0 c \gamma^2 B^2}{m}, \tag{2}$$

while the spectrum is [6]

$$\frac{dI}{d\omega} = \tfrac{2}{3} mc^2 \frac{r_0 c \gamma^4}{\rho^2} \frac{9\sqrt{3}}{8\pi} \frac{\omega}{\omega_c^2} \int_{\omega/\omega_c}^{\infty} K_{5/3}(x)dx = I \frac{9\sqrt{3}}{8\pi} \frac{\omega}{\omega_c^2} \int_{\omega/\omega_c}^{\infty} K_{5/3}(x)dx \tag{3}$$

As integral of spectral density over all frequency interval must be equal to full intensity, i.e. $\int_0^{\infty} \frac{dI}{d\omega} d\omega = I$, the $P(\omega) = \frac{9\sqrt{3}}{8\pi} \frac{\omega}{\omega_c^2} \int_{\omega/\omega_c}^{\infty} K_{5/3}(x)dx$ could be treated as the probability of radiation of photon with frequency ω, i.e. with energy $E_\gamma = \hbar\omega$. Expanding Bessel function for the argument values of our interest $x \equiv \omega/\omega_c >> 1$ as $K_{5/3}(x) \cong \sqrt{\frac{\pi}{2x}} e^{-x}$ spectral distribution of intensity (3) could be transformed to

$$\frac{dI}{d\omega} = I \frac{9\sqrt{3}}{8\sqrt{\pi}} \frac{\omega}{\omega_c^2} \int_{\omega/\omega_c}^{\infty} \frac{e^{-x}}{\sqrt{x}} dx \cong I \frac{9\sqrt{3}}{8\sqrt{2\pi}} \frac{1}{\omega_c} \sqrt{\frac{\omega}{\omega_c}} \exp(-\frac{\omega}{\omega_c}) \tag{4}$$

Photon SR spectrum represented in Fig.1.

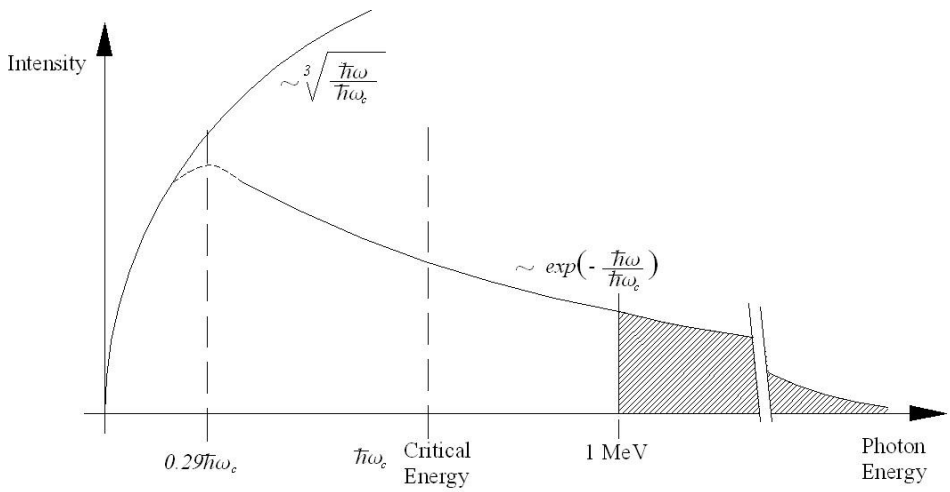

Figure 1: SR spectrum. Hatched area corresponds to the photon flux able to create positrons.

Spectral distribution of the photon flux could be obtained from (4) by dividing it by the energy of the photon ($\hbar = 6.58 \cdot 10^{-22} MeV \cdot s$)

$$\frac{d\dot{N}_\gamma}{d\omega} = \frac{dI}{\hbar\omega \cdot d\omega} \cong I \frac{9\sqrt{3}}{8\sqrt{2\pi}} \frac{1}{\hbar\omega} \frac{1}{\omega_c} \sqrt{\frac{\omega}{\omega_c}} \exp(-\frac{\omega}{\omega_c}). \tag{6}$$

By introducing a variable $y = \omega/\omega_c$ this expression could be rewritten as ($y>>1$)

$$\frac{d\dot{N}_\gamma}{dy} \cong I \frac{9\sqrt{3}}{8\sqrt{2\pi}} \frac{1}{\hbar\omega_c} \frac{\exp(-y)}{\sqrt{y}}. \tag{7}$$

Threshold value of variable y comes to $y \geq y_c = 2mc^2/\hbar\omega_c$ (in our case $y_c \cong 5.8$) . So the total number of photons radiated per one second, which energy is enough to create a pair coming to

$$\dot{N}_\gamma \cong I \frac{9\sqrt{3}}{8\sqrt{2\pi}} \frac{1}{\hbar\omega_c} \int_{y_c}^{\infty} \frac{\exp(-y)}{\sqrt{y}} dy \cong I \frac{9\sqrt{3}}{8\sqrt{2}} \frac{1}{\hbar\omega_c} Erfc[\sqrt{y_c}] \tag{8}$$

Graph of function $Erfc[y_c]$ is represented in Fig. 2.

Let us evaluate the photon flux. First the local bending radius in (2) for $10T$ (=$100kG$) field comes to $\rho = mc^2\gamma/eB \cong 167$ *cm.* As $r_0 = e^2/mc^2 \cong 2.8\cdot10^{-13}cm$, $\gamma \cong 10^4$, total energy carried out by all photons while the particle passes the wiggler having length L=100 *cm* comes to

$$I \cdot \frac{L_w}{c} \cong \tfrac{2}{3} mc^2 \frac{r_0 c\gamma^4}{\rho^2} \frac{L_w}{c} \cong 1.022MeV \frac{2.8\cdot10^{-13}\cdot3\cdot10^{10}\cdot10^{16}}{3\cdot2.8\cdot10^4} \frac{100}{3\cdot10^{10}} \cong 3.66[MeV] \tag{9}$$

So the number of photons with their energy >1.022 MeV, radiated by each electron per one pass according to (8) comes to

$$\Delta N_\gamma \cong 3.66[MeV]\cdot1.37\cdot10^{-3}\cdot10^{-3}/0.17[MeV\cdot\sec] \cong 3.2\cdot10^{-5}[Photons/pass]$$

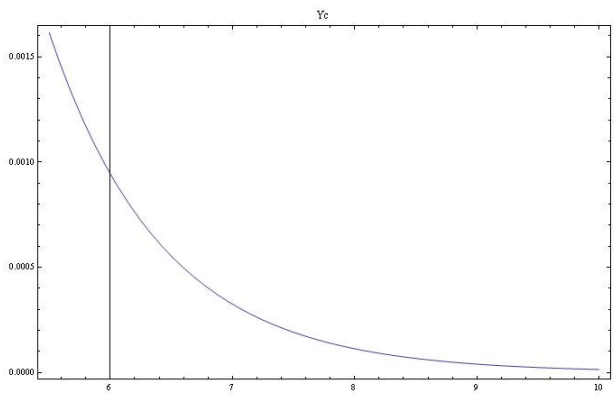

Figure 2. Function $Erfc[y_c]$.

As the number of electrons in ERL corresponds to average current $I = eN_b f \cong 0.1[A]$, where f=1.3GHz, then the number of "useful" photons (which energy >1.022 MeV) per second comes to

$$\dot{N}_\gamma \cong \Delta N_\gamma N_b f = \Delta N_\gamma I/e \cong 3.2\cdot10^{-5}\cdot0.1/1.6\cdot10^{-19} \cong 2\cdot10^{13}[Photons/\sec] \tag{10}$$

Of cause not all of these photons are equally effective for positron production, as the threshold cross section of pair production is rather sensitive to the energy, $\sigma_{\gamma\to e^-e^+} \cong \frac{\pi}{12} Z^2\alpha\, r_0^2 (\frac{\hbar\omega - 2mc^2}{mc^2})^3$ [12].

For calculation of ***energy spread*** in the beam generated after passage the wiggler field, the number of photons with critical energy is important. The number of photons with critical energy radiated by high energy beam with $\gamma = E/mc^2$ bending with angle φ

$$N_\gamma \cong \alpha\gamma\varphi ,$$

where $\alpha = e^2/\hbar c$. So for 5 GeV beam, $\varphi \cong \lambda_w/\rho \cong \frac{3}{2}\cdot 30/167 \cong 0.27$ (per $1m$) each electron radiates $N_\gamma \cong 19.7$ per one pass. We expect that these will be a ~0.17-MeV gammas (magnetic field chosen so it is), so the energy loosen by each particle per one pass is

$$\hbar\omega N_\gamma \cong 0.17MeV \cdot 19.7 \cong 3.35MeV ,$$

which is in good agreement with (9). The energy spread comes to

$$\Delta E \cong \hbar\omega\sqrt{N_\gamma} \cong 0.17MeV \cdot 4.4 \cong 0.75MeV , \quad (5)$$

i.e. relative spread about $\delta E \equiv \Delta E/E \cong 1.6\cdot 10^{-4}$. We would like to underline here that this absolute energy spread remains constant down to the collector. So it will be necessary slightly increase of dump energy (which is ~15 *MeV* now) by this value (5).

Looks, that method [9] is feasible for ERL. Slight difference between [10] and present proposal: helical wiggler instead of planar with period 30 *cm* and with axial field up to 8-10*T*.

As the harmonics number for critical energy is $n_c = \frac{3}{2}\gamma^3 \cong 1.5\cdot 10^{12}$, the critical energy value comes to $\hbar\omega_c \cong n_c \cdot \hbar\omega_0 \cong 0.174\cdot$MeV. Radiation with energy ~ 1MeV corresponds to the number of harmonic

$$n_{c\gamma} \cong n_c \cdot \frac{2mc^2}{\hbar\omega_c} = \frac{2mc^2}{\hbar\omega_0} = \frac{2m^2c^2\gamma}{\hbar eB} \cong 10^{13}$$

Angle of radiation is a conic one with opening $\vartheta \cong K/\gamma$ which is $\vartheta \cong 10^{-2}$ in our case, so at the distance of L=5 m the radius of gamma beam will be $r = L\vartheta = KL/\gamma \cong 5cm$. The gamma beam will be hollow, however, so the trace of the gamma beam on the target will be a ring-like line with characteristic thickness ~0.5*mm*.

Emittance growth could be calculated on the basis

$$\frac{d\varepsilon_x}{ds} \cong \left\langle \left(H_x + \frac{\beta_x}{\gamma^2} \right) \frac{d(\Delta E/E)^2_{tot}}{ds} \right\rangle - 2\alpha_x\varepsilon_x , \quad (6)$$

with similar equation for vertical motion, where defined

$$H_{x,y} = \frac{1}{\beta_{x,y}} \left(\eta^2_{x,y} + (\beta_{x,y}\eta'_{x,y} - \frac{1}{2}\beta'_{x,y}\eta_{x,y})^2 \right), \quad (7)$$

$\eta_{x,y}$ –are dispersion functions in wiggler. As outside values of dispersion could be chosen so they are to be about zero, the dispersion in (7) is the one generated bu wiggler itself. Partial decrements $\alpha_{x,y,s}$ are defined as $\alpha_i = J_i/2l_s$, where $J_x \cong 1, J_y = 1, J_s \cong 2,\ J_x + J_s = 3$. Partial decrement for energy spread is the same as the one for emittance. If dispersion generated by wiggler itself, then

$$\eta_x = \frac{K_x \lambda\!\!\!^{-}}{\gamma} Sin\frac{s}{\lambda\!\!\!^{-}} = \frac{\lambda\!\!\!^{-2}}{\rho_x} Sin\frac{s}{\lambda\!\!\!^{-}} , \quad (8)$$

where $\lambda\!\!\!^{-} \equiv \lambda_w / 2\pi$, $\rho_x = \lambda\!\!\!^{-}\gamma / K_x$, λ_w stands for the wiggler period (and the same for other coordinate). So change of emittance comes to

$$\Delta\varepsilon_x \cong \frac{1}{2}\frac{K^2\overline{\beta}_x}{\gamma^4}\Delta(\frac{\Delta E}{E})^2_{tot} - 2\alpha_x\varepsilon_x L \tag{9}$$

Estimating the first term (source of heating) one can obtain

$$\Delta\varepsilon_x \cong \frac{1}{2}\frac{K^2\overline{\beta}_x}{\gamma^4}\Delta(\frac{\Delta E}{E})^2_{tot} \cong \frac{1}{2}\frac{250^2\cdot 10}{10^{16}}10^{-6} \sim 3\cdot 10^{-17} m\cdot rad \ ,$$

i.e. a negligible value.

HELICAL WIGGLER

Difference from [10] is in a wiggler: we suggesting *helical* wiggler with period 30 cm and with axial field up to 8-10T. Basically design of helical wiggler is similar to high field dipole magnet. The necessary twist with period 30 is big compared with aperture, which is 2*a*~30*mm*. Field distribution inside aperture is shown in Figs. 3-4 calculated with numerical code MERMAID.

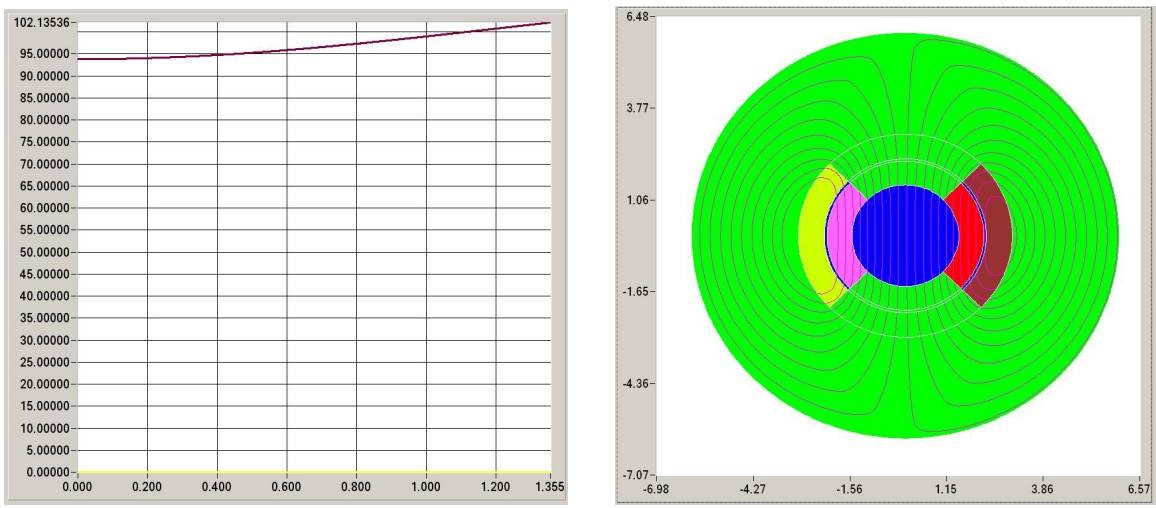

Figure 3: Field across aperture, at the left. Lines of magnetic field, at the right.

Coil is sectioned in two separate ones. The inner one carries total current ~80kA having area ~2cm^2. Outer coil carries has ~450 kA with area~3cm^2. So the current density runs 39.3 and 149.07 kA/cm^2 respectively.

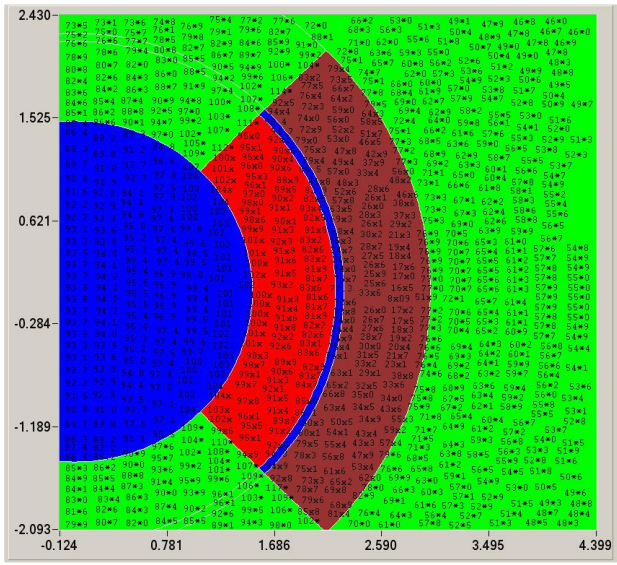

Figure 4: Numerical values of the field in helical magnet.

Trajectory of particle in a wiggler looks like a helix having radius $r = \lambda K / \gamma \cong 1mm$. Some set of end correction coils required to keep the first and the second field integrals around zero values.

TARGET AND MODERATOR

Positrons have negative affinity to the solid state media, see Fig.5 . So finally all positrons must came out if not trapped into defects and if not annihilated with electrons riding between atoms. That is why the purity of moderator plays important role here.

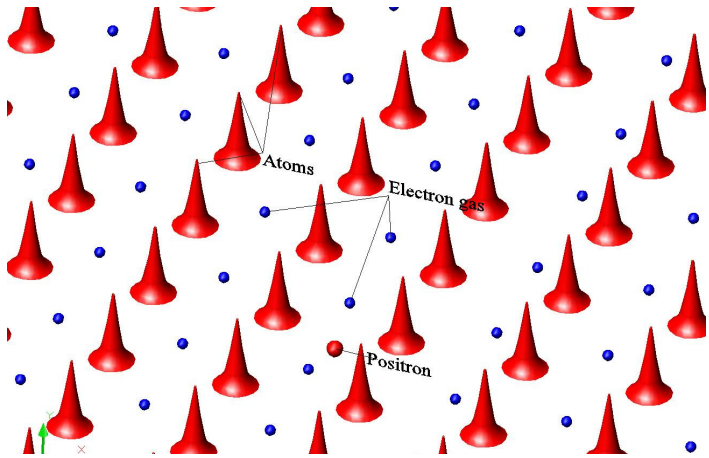

Figure 5: Schematics of potential well for positrons.

Positrons are under repulsive force from nucleus, Fig.5, the only valence electrons acting with positrons, yield annihilation finally.

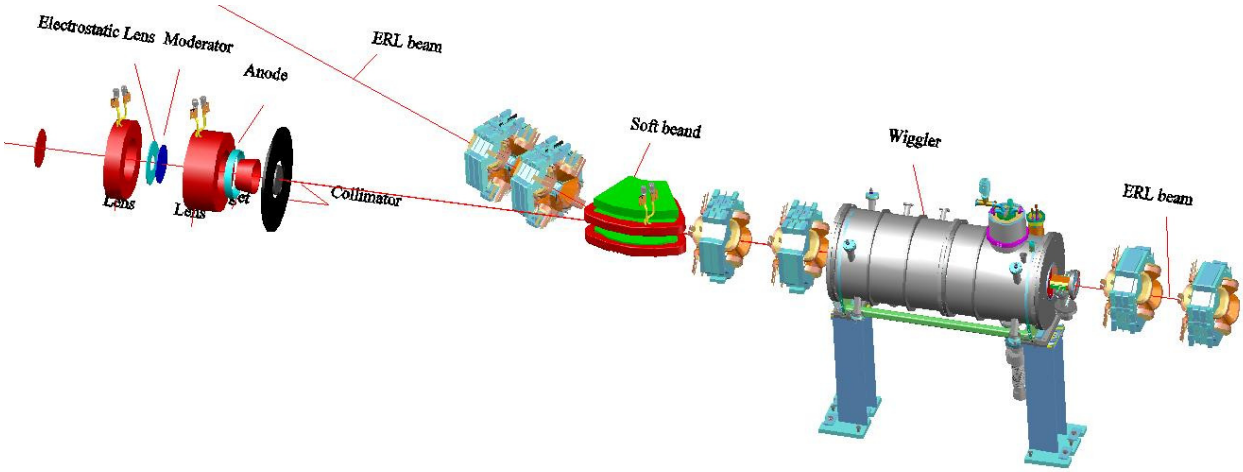

Figure 6: 3D view on the installation. ERL beam coming from the right.

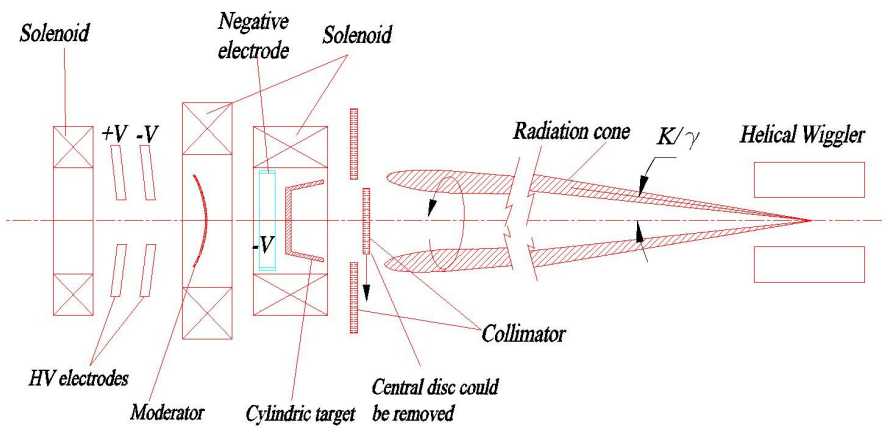

Figure 7: Positron conversion system schematics. Radiation cone has opening ~ K/γ.

Positron target in Fig.6 Fig.7 is a pot-like one. The side conical wall has some small angle and thickness, but effective thickness of the target in longitudinal direction is ~few X_0, where $X_0^{-1} \cong 4r_0^2 \alpha \frac{N_0}{A}(Z+1)Z \cdot \ln(\frac{183}{Z^{1/3}})[cm^2/g]$ stands for the Radiation length ($\alpha \cong 1/137$ –fine structure constant, N_0 –Avogadro number, A-is the atomic weight, Z–is the atomic number). Positrons created in a target can escape easily in transverse direction. The positrons from outer side only could be collected for further usage. So basically this positron target resembles a type of magnetron electron gun serving for generation of hollow beam.

So the probability of positron creation in this target ~100%, but we estimate that only 15% could be transformed into positrons which could be collected.

Moderator made from single crystal foil (sheet) with spherical profile. Together with electrostatic electrode kept at negative potential, it serves for better collection and focusing of positrons. Presence of electric field helps positrons to leave the surface of moderator. Tungsten, Copper could serve as materials for moderator; what is important-absence of defects in crystal structure. Yield between 10^{-2} -10^{-4} could be expected here.

As the energy loss per one pass is ~3.66 *MeV*, then for current 100 *mA* the total power radiated comes to ~366 *kW*, distributed on a ring of 5cm in diameter. We estimate that at least 60% of this power will be accepted by collimator. Absorption of ~100kW of power illuminating the target itself will be not a problem as the power density remains low.

SUMMARY

For generation of thermal positrons we revisited old idea about positron production from gammas. The gammas generated by the high-energy electron beam by Wiggler/Synchrotron Radiation in magnetic field. This might be a planar of helical wiggler installed in ERL. One important peculiarity of ERL is that the beam is small at all times, so the aperture of such wiggler might be small. In its turn this allows high magnetic field value. Recuperation of energy is also very important item here as the primary electron current must be high to support the positron yield of interest. Perturbation of emittance and introduced energy spread remains within acceptable for further recuperation.

More detailed calculation could be done if necessary, as all phenomena is well developed topics.

By itself, the method of generation of hard radiation might be interesting for research carrying with high energy photons (above 1 MeV).

Table 1. Basic parameters of system

Parameter	Value
Energy of the beam	5 GeV
Current	100 mA
Magnetic field	~9T
Period	~0.3m
Number of periods	3
K factor	~250
Emittance grows	negligible
Energy spread grows	~0.75 *MeV**
Positron flux	10^{8}-10^{11}/sec
Polarization	>30%

***** depends on positron flux required.

REFERENCES

[1] K.G.Lynn, M.H.Weber," *Positrons for Applied Science*", a talk at JPOS09-International Workshop on Positrons at Jefferson Lab, Newport News, VA, March 25-27, 2009.

[2] A.Uedonot et al, "*Positron Annihilation in Silicon in Thermal Equilibrium at High Temperature*", Phys.: Condensed Matter **12** (2000) 719-728.

[3] P.X.Gan, et al., "*Introduction to Beam-Based Positron Spectroscopy Techniques*", Physics 152A: Condensed Matter Physics, March 2, 2004.

[4] A.G.Zaluzhnyi et al., "*Thermalization of Positronium Atoms in Ionic Crystals*", ISSN 1027-4510, Journal of Surface Investigation, X-ray, Synchrotron and Neutron Techniques, 2008, Vol.2 pp.92-97.

[5] F.Komori, " *Thermalized-Positron Induced Ion Deposition from Surfaces*", Current Option in Solid State and Material Science 6(2002) 163-167.

[6] A.Dupasuier, A.P.Millsjr, editors." *Positron Spectroscopy of Solids*", Amsterdam, Oxford, Tokyo, Washington DC:IOS Press; 1995.
[7] Terry L. Dull, "*Probing Low-k Dielectric Films with Depth-Profiled Positronium Annihilation Lifetime Spectroscopy*." Workshop on Positron Studies of Semiconductor Defects (PSSD-99), McMaster University, ON, Canada, July 21 - 23, 1999. http://www.obrien-dull.com/profpages/talks.html .
[8] G.A.Schott, "*Electromagnetic Radiation and the Mechanical Reactions Arising from It*", Cambridge: at the University Press (1912), 327pp.
[9] V.Balakin, A.Mikhailichenko,"*The Conversion System for Obtaining High Polarized Electrons and Positrons*", Budker Institute of Nuclear Physics, BINP 79-85 (1979).
[10] A.Ando, V.Belyaev, S.Daté, H.Kamitsubo, A.Kiselev, G.Kulipanov, N.Kumagai, N.Mezentsev, Y.Miyahara, T.Nakamura, A.Skrinsky, K.Soutome, M.Takao, I.Voronchev, "*Production of Intense Low-Energy Positron Beams with Synchrotron Radiation*", J. Synchrotron Rad. (1996), **3**, 201-206.
[11] P.Stefazzo, "*Slow positrons and Thermal Ps Production Using Thin Foils*", Appl. Phys. A 36, 93-95 (1985).
[12] V.Berestetsky, E.Lifshits, L.Pitaevsky,"*Quantum Electrodynamics*", §94.

RECENT PROGRESS ON BEAM-BREAKUP CALCULATIONS FOR THE CORNELL X-RAY ERL

J. A. Crittenden, * G.H. Hoffstaetter, M. Liepe, C.E. Mayes, and D.C. Sagan
CLASSE, Cornell University, Ithaca, NY 14853-8001

Abstract

Beam-breakup calculation algorithms have been developed in the general framework of the Cornell X-ray ERL design software, enabling their extension to multi-pass optics design for ERLs. A status report of this work is presented, together with initial results comparing the instability thresholds calculated for single- and two-turn optics with recently developed RF cavity designs.

INTRODUCTION

The potential for excellent quality of X-ray beams from low-emittance electron beams produced by a 5-GeV superconducting energy-recovery linac (ERL) is motivating an extensive development study at Cornell. Figure 1 shows the present status of the design layout on the Cornell campus.

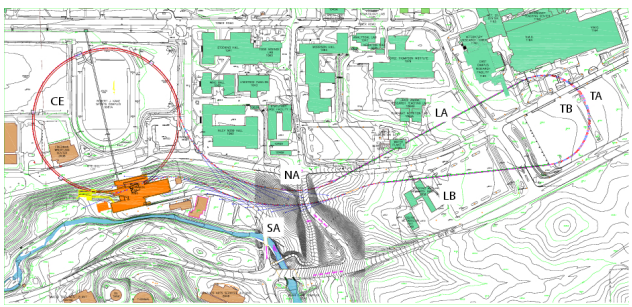

Figure 1: Layout of the Cornell X-ray ERL.

The 10 MeV electron beam produced by the injector is accelerated to 2.8 GeV in the first linac (LA), transported to the second linac (LB) by the high-energy turnaround (TA), where it is accelerated to 5 GeV. The south arc (SA) provides X-ray beamlines, the present CESR ring (CE) is used to transport the beam to the North Arc (NA) beamlines, then the first linac decelerates the 5 GeV beam to 2.2 GeV, and the inner turnaround (TB) transports the beam to the second linac where it is decelerated to 10 MeV and stopped.

Beam-breakup (BBU) instabilities arising from the excitation of higher-order modes in the superconducting RF cavities in the main linacs are important contributions to the operational current limit [1]. The original quantitative estimates of the instability threshold limits in the case of continuous wave recirculators have been extended to energy-recovery linacs [5] and generalized to coupled optics and polarized higher-order modes (HOMs) [6]. More recently, detailed numerical estimates for the Cornell one-turn ERL design have been obtained [7]. This paper reports on the implementation of such calculations in Bmad, the lattice analysis and design software package developed at Cornell for the ERL, CESR and other projects [3]. Primary motivation for this work is the extension to multi-pass ERLs.

BEAM-BREAKUP CALCULATIONS IN THE CORNELL ACCELERATOR-DESIGN SOFTWARE BMAD

Beam-breakup instabilities arising from higher-order-mode (HOM) power induced in the linac RF cavities have been modeled using Bmad tracking calculations by choosing an initial beam current with all RF buckets filled, tracking an off-axis beam to load HOM power, then testing for the time dependence of the highest HOM amplitude over a predetermined number of turns. A binary search for the threshold current then provides the instability limit to any chosen accuracy.

Solutions for the threshold current can be accurately approximated by simple formulas for the case of a single HOM in a single cavity where the HOM decay time is short or long relative to the return time [5]. Figure 2 shows the comparison of the Bmad tracking calculation to the analytic approximation of the threshold current for the toy model described in Ref. [5]. The HOM parameters are $R/Q = 100\ \Omega$, $f_\lambda = 2.0$ GHz, and $Q_\lambda = 10^4$. For the purposes of validating the model, the return time to the cavity was scanned through the period of the BBU sensitivity determined by the HOM parameters and the bunch spacing. The result for the threshold current as a function of the ratio of the return time t_r to the time between bunches t_b (0.77 ns for the 1.3 GHz cavities) is compared to the analytic approximation.

Having demonstrated the accuracy of the BBU thresholds in the short-return-time limit, we apply the model to the full Cornell ERL optics with the same single HOM parameters modeled in a single cavity. This case exemplifies the limit of return times much greater than the HOM decay time. Figure 3 shows the result of the scan, demonstrating that the Bmad tracking reproduces the analytic approximation. The higher order mode parameters employed for this study are those of the first HOM of Ref. [6]: $R/Q = 71\ \Omega$, $f_\lambda = 1.861$ GHz, and $Q_\lambda = 4968$.

* crittenden@cornell.edu

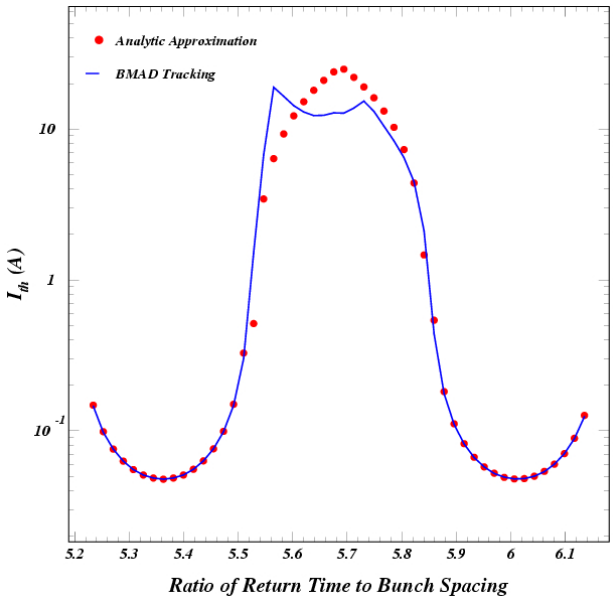

Figure 2: Comparison of the Bmad tracking result for the BBU instability threshold current for the case where of a single HOM in a single cavity where the return time is much less than the HOM decay time. The result is compared to the analytic approximation for this case.

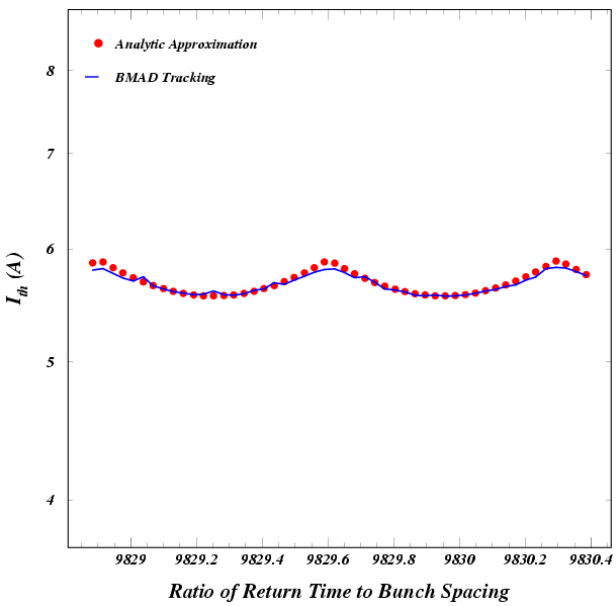

Figure 3: Comparison of the Bmad tracking result for the BBU instability threshold current for the full Cornell X-ray ERL optics with a single HOM in a single cavity, where the return time is much greater than the HOM decay time.

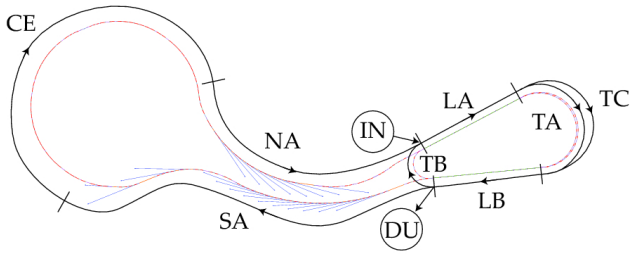

Figure 4: Layout of the two-turn ERL design.

TWO-TURN ERL DEVELOPMENT

Figure 4 shows the layout of the two-turn ERL for which optics has been designed. The linacs are half as long and a third turnaround (TC) has been added to provide the first of two accelerating turns through the linacs.

Figure 5 compares the BBU threshold calculation for the

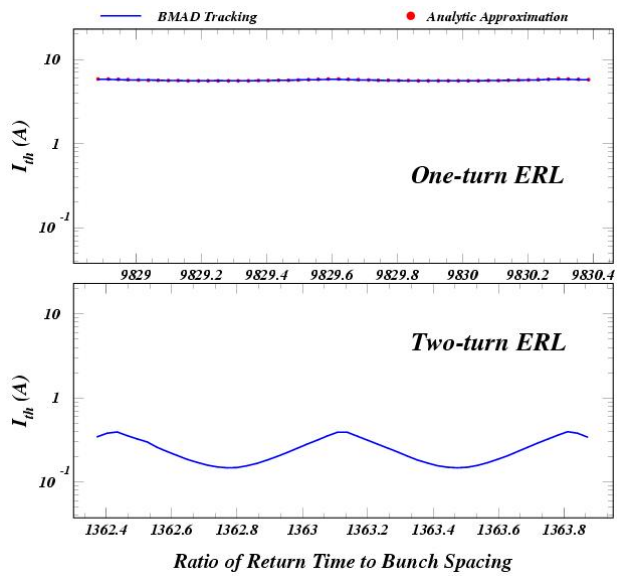

Figure 5: Comparison of the Bmad BBU threshold calculation for the simple HOM parameters in the one-turn optics to the result for the two-turn optics.

one-turn optics shown in Fig. 3 with the result for the same HOM parameters in the two-turn optics. The worst-case threshold for the two-turn ERL is about 100 mA, about a factor of 50 lower than that for the one-turn optics in this simplified case. A full calculation is expected to yield a threshold for the two-turn optics which is about a factor of six smaller [5]. The Bmad BBU threshold calculation algorithm remains under active development.

CAVITY DESIGN OPTIMIZATION

We are currently in the process of optimizing the cell shape of two main linac cavity designs with differences in the cavity end sections: a 7-cell cavity with a 39-mm radius beam tube end section on one end and a 55 mm beam tube

end section on the other end, and a 7-cell cavity with 55-mm radius beam tubes on both ends [4]. The cavity designs use the same center-cell shape, which has been optimized to minimize dynamic cryogenic losses for a given iris radius of 35-mm, a maximum wall angle of 85°, and limiting the ratio of peak electric field to accelerating field to a maximum value of 2. In each case, the end cell shapes are optimized to minimize the BBU HOM factor $(R/Q)Q/f$ of the worst higher order mode(s). The worst case HOM in these designs has a value of $(R/Q)Q/f \approx 3 \cdot 10^4$. Future optimization is likely to reduce this value.

BBU tracking results for a one-turn ERL with cavities based on the design with 55 mm beam tubes on both ends are summarized in Table 1. In addition, results obtained for the same ERL lattice, but with cavity HOM parameters as given in [7] are shown. BBU threshold currents have been calculated with and without HOM frequency spread from cavity to cavity for a given type of HOM.

	Cavity parameters from [7]			55-55 mm cavity parameters		
HOM	f [MHz]	Q	(R/Q) [Ω/cm^2]	f [MHz]	Q	(R/Q) [Ω/cm^2]
1	1861.37	4968	5.4403	2512.896	8867	2.1180
2	1873.94	20912	8.4409	2513.556	1472	7.6777
3	1881.73	13186	2.1629	2514.671	8557	8.1083
4	2579.66	1434	15.7821	3068.192	186198	0.0632
5				3073.245	64567	0.3971
Turns	No frequency spread					
1		12 mA			36 mA	
2		6 mA			8 mA	
	$\sigma_f/f = 0.4\%$					
1		235 mA			307 mA	
2		53 mA			87 mA	

Table 1: BBU tracking results for 7-cell cavity designs. In each case, the HOMs with highest values of $(R/Q)Q/f$ have been included in the Bmad tracking calculations, as listed below.

These results provide a first estimate of the improvement in the BBU instability threshold provided by the cavity redesign. They also give an early indication of the reduced thresholds in a two-turn optics. However, a more systematic study including the effects of varying HOM parameters and mitigation techniques such as HOM polarization will be required before conclusions can be drawn. Note also that the spread over many recalculations in the calculated threshold values for the case of HOM frequency spread is about 20% [7].

SUMMARY

Beam-breakup instability calculation algorithms have been implemented in the framework of the accelerator design software tool Bmad, enabling their extension to multi-pass ERLs. They have been validated by comparison to analytic approximations and to prior numerical estimates. These calculations will serve an important purpose in the further development of the Cornell X-ray source design. The design of the lattice optics and that of the superconducting RF cavities are interdependent. First results on the threshold currents for two cavity designs for one-turn and two-turn optics have been obtained. Further work on mitigating considerations such as HOM frequency spread and coupling with HOM polarization will be necessary.

REFERENCES

[1] G.A. Krafft, J.J. Bisognano, and S. Laubach, *Calculating Beam-Breakup in Superconducting Linear Accelerators*, reissued as JLAB-01-011-1 (2009)
G.A. Krafft and J.J. Bisognano, *Two Dimensional Simulations of Multipass Beam Breakup*, proceedings of PAC87
G.A. Krafft and J.J. Bisognano and R.L. Gluckstern, *Multipass Beam Breakup in Recirculating Linacs*, proceedings of PAC87

[2] C.E. Mayes, Ph.D. Dissertation, Cornell University (2009)

[3] D. Sagan, *Bmad: A Relativistic Charged Particle Simulation Library*, Nuc. Instrum. & Methods **A558**, 356 (2006). The Bmad manual can be obtained at `http://www.lepp.cornell.edu/~dcs`

[4] M. Liepe, these proceedings

[5] G.H. Hoffstaetter, I.V. Bazarov, *Beam-Breakup Instability Theory for Energy Recovery Linacs*, Phys. Rev. ST-AB **7**, 054401 (2004)

[6] G.H. Hoffstaetter, I.V. Bazarov, C. Song, *Recirculating Beam-Breakup Thresholds for Polarized Higher-Order Modes with Optical Coupling*, Phys. Rev. ST-AB **10**, 044401 (2007)

[7] C. Song, G.H. Hoffstaetter, *Transverse Recirculating-BBU Threshold Current in the Cornell X-Ray ERL*, Report Cornell-ERL-06-01 (2006)

EFFECTS OF LONGITUDINAL AND TRANSVERSE RESISTIVE-WALL WAKEFIELDS ON ERLS

N. Nakamura#
Institute for Solid State Physics(ISSP), University of Tokyo
5-1-5 Kashiwanoha, Kashiwa, Chiba 277-8581, Japan.

Abstract

Exact expressions of longitudinal and transverse resistive-wall impedances for a round pipe with a finite thickness were analytically obtained to accurately evaluate effects of resistive-wall wakefields on energy recovery linacs(ERLs). Parasitic loss in an ERL vacuum chamber due to the longitudinal impedance was evaluated and found to be serious compared with 3rd generation SR sources because of the shorter bunch length. It was also shown by the calculation result of longitudinal resistive-wall impedance of a two-layer round pipe that copper coating is effective for reducing the parasitic loss of a stainless steel(SS) chamber. Transverse resistive-wall wake functions of round pipes were numerically calculated using the exact impedance expression to simulate transverse multi-bunch beam motions due to resistive-wall wakefields in ERLs. Possibility of resistive-wall beam breakup(BBU) in the compact ERL and in a long undulator chamber of a 5-GeV ERL was discussed based on simulation results.

INTRODUCTION

In ERL-based synchrotron radiation(SR) sources, high-current and short-bunch beams are circulated. Such a beam can generate strong wakefields in resistive-wall ERL components and the wakefields seriously affect the components and the beam itself. Transverse multi-bunch beam breakup due to the resistive-wall wake was already studied with analytical and simulation approaches using the conventional expression of the resistive-wall wake function[1][2]. Although the study results implied that the beam position displacement due to the resistive-wall wake infinitely increases with time, it was also pointed out that the conventional expression of the resistive-wall wake function is valid only in a limited time range[2]. In this paper, exact expressions of the longitudinal and transverse impedances are derived to correctly estimate the resistive-wall impedances and their effects on ERLs. Transverse multi-bunch beam motions are simulated with the exact wake functions. Furthermore parasitic loss in a vacuum chamber due to the longitudinal resistive-wall wakefields is also evaluated.

EXACT EXPRESSIONS FOR RESISTIVE-WALL IMPEDANCES

Longitudinal Impedance

An exact expression of the longitudinal resistive-wall impedance (per unit length) of a round pipe with an inner radius b and a thickness d was analytically derived as follows:

$$Z_{//}(\omega)=\frac{-i}{2\pi\varepsilon_0 bc\left\{\left(\frac{\omega}{\lambda c}+\frac{\lambda c}{\omega}\right)\alpha_l-\frac{b\omega}{2c}\right\}} \quad (1)$$

$$\alpha_l=\frac{J_1(\lambda b)N_0(\lambda(b+d))-N_1(\lambda b)J_0(\lambda(b+d))}{J_0(\lambda b)N_0(\lambda(b+d))-N_0(\lambda b)J_0(\lambda(b+d))}$$

$$\lambda=\frac{i+sgn(\omega)}{\delta}\quad\left(\delta=\sqrt{\frac{2}{\sigma\mu_0|\omega|}}\right)$$

Here σ, ε_0, μ_0, c, i, ω, and δ are the electric conductivity of the pipe, the permittivity and permeability of vacuum, the velocity of light, the imaginary unit, the angular frequency and the skin depth of the pipe, and J_0, J_1, N_0 and N_1 are the 0th-order and 1st-order Bessel functions of the 1st and 2nd kinds, respectively. The permittivity and permeability of the pipe are assumed to be equal to or approximated by those of vacuum. The $sgn(\omega)$ means the sign of ω. If the pipe thickness becomes infinity, the expression is rewritten as Eq. (2) with the 0th-order and 1st-order Hankel functions of the 1st kind, $H_0^{(1)}$ and $H_1^{(1)}$.

$$Z_{//}(\omega)=\frac{-i}{2\pi\varepsilon_0 bc\left\{\left(\frac{\omega}{\lambda c}+\frac{\lambda c}{\omega}\right)\frac{H_1^{(1)}(\lambda b)}{H_0^{(1)}(\lambda b)}-\frac{b\omega}{2c}\right\}} \quad (2)$$

If one considers the frequency range satisfying the conditions of $|\lambda|b>>1$, $|\lambda|>>|\omega/c|$, $|\lambda|>>b\omega^2/c^2$, the conventional impedance expression of Eq. (3) is derived from Eq. (2).

$$Z_{//}(\omega)=\frac{\omega Z_0\delta}{4\pi bc}\{sgn(\omega)-i\}\quad\left(Z_0=\sqrt{\frac{\mu_0}{\varepsilon_0}}\right) \quad (3)$$

Here Z_0 is the impedance of vacuum.

Figure 1 shows the real parts of the resistive-wall impedances of stainless steel(SS) pipes with b=8 mm and σ=1.4×10^6 Ω^{-1}m^{-1} calculated from Eqs. (1) and (2). For comparison, the conventional expression of Eq. (3) is shown in the figure. The real parts of the exact impedances have two kinds of cut-offs, low and high frequency cut-offs. The high-frequency cut-off depends on only the pipe radius. On the other hand, the low-frequency cut-off depends on both pipe radius and thickness. Only in the intermediate frequency range, the impedances are approximated by Eq. (3) as shown in Fig. 1.

#nakamura@issp.u-tokyo.ac.jp

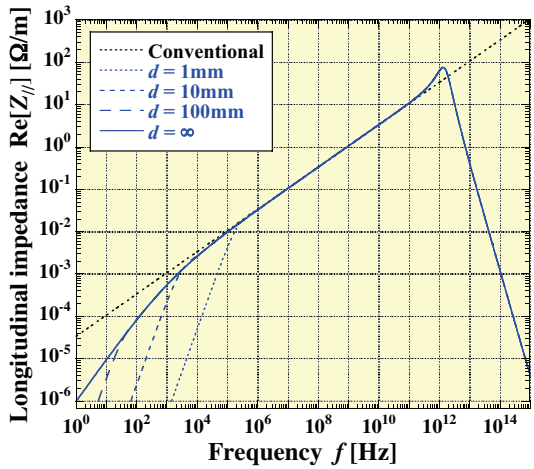

Figure 1: Longitudinal resistive-wall impedances of round pipes with an inner radius of 8 mm and thicknesses of 1, 10, 100 mm and infinity. The conventional impedance expression is also plotted by a black dotted line.

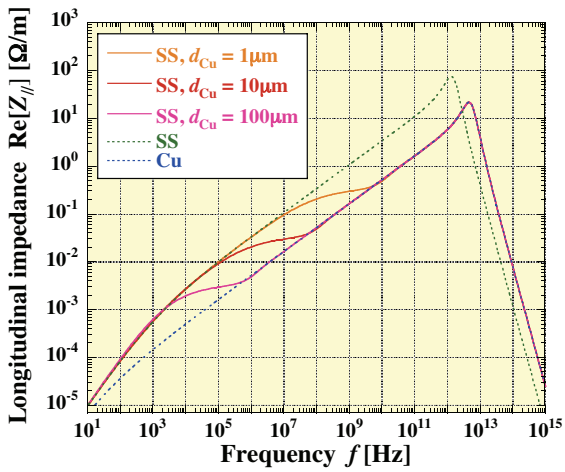

Figure 2: Longitudinal resistive-wall impedances of Cu-coated stainless steel(SS) pipes with an inner radius of 8 mm and Cu-coating thicknesses of 1, 10, 100 μm. The impedances of pure Cu and SS pipes are also plotted by blue and green dotted lines.

Longitudinal resistive-wall impedance of a two-layer round pipe was also derived as Eq. (4).

$$Z_{//}(\omega) = \frac{-i}{2\pi\varepsilon_0 bc\left\{\left(\frac{\omega}{\lambda_1 c}+\frac{\lambda_1 c}{\omega}\right)\alpha_{l2}-\frac{b\omega}{2c}\right\}} \qquad (4)$$

$$\alpha_{l2} = \frac{J_1(\lambda_1 b)+\kappa N_1(\lambda_1 b)}{J_0(\lambda_1 b)+\kappa N_0(\lambda_1 b)}$$

$$\lambda_{1,2} = \frac{i+sgn(\omega)}{\delta_{1,2}}, \quad \delta_{1,2} = \sqrt{\frac{2}{\sigma_{1,2}\mu_0|\omega|}}$$

$$\kappa = \frac{\left(\frac{\omega}{\lambda_1 c}+\frac{\lambda_1 c}{\omega}\right)H_0^{(1)}(\lambda_2(b+d))J_1(\lambda_1(b+d))-\left(\frac{\omega}{\lambda_2 c}+\frac{\lambda_2 c}{\omega}\right)H_1^{(1)}(\lambda_2(b+d))J_0(\lambda_1(b+d))}{\left(\frac{\omega}{\lambda_2 c}+\frac{\lambda_2 c}{\omega}\right)H_1^{(1)}(\lambda_2(b+d))N_0(\lambda_1(b+d))-\left(\frac{\omega}{\lambda_1 c}+\frac{\lambda_1 c}{\omega}\right)H_0^{(1)}(\lambda_2(b+d))N_1(\lambda_1(b+d))}$$

Here b, d, $\sigma_{1,2}$, $\delta_{1,2}$ are the inner radius of the pipe, the thickness of the inner layer, the electric conductivities and the skin depths of the inner and outer layers. The thickness of the outer layer is assumed to be infinite. Definitions of the other parameters are the same as those of the one-layer pipe in Eq. (1).

Figure 2 shows the real parts of the resistive-wall impedances of copper(Cu)-coated SS pipes with an inner radius of 8 mm and Cu-coating thicknesses of 1, 10 and 100 μm calculated from Eq. (4). The Cu coating corresponds to the inner layer of the two-layer pipe and the electric conductivity of Cu is 5.9×10^7 $\Omega^{-1}m^{-1}$. For comparison, the impedances of pure Cu and SS pipes with the same inner radius are shown in the same figure. As found in Fig. 2, the impedances of Cu-coated SS pipes agree with that of the pure SS pipe at low frequencies and the pure Cu pipe at high frequencies. The frequency where the transition from the SS to Cu impedance occurs depends on the Cu-coating thickness.

Transverse Impedance

An exact expression of the transverse resistive-wall impedance of a round pipe with an inner radius b and a thickness d was derived as

$$Z_{\perp}(\omega) = \frac{-i}{\pi\varepsilon_0 b^3\omega\left\{\left(\frac{2\omega}{\lambda c}+\frac{\lambda c}{\omega}\right)\alpha_t-\frac{b\omega}{2c}\right\}} \qquad (5)$$

$$\alpha_t = \frac{J_2(\lambda b)N_1(\lambda(b+d))-N_2(\lambda b)J_1(\lambda(b+d))}{J_1(\lambda b)N_1(\lambda(b+d))-N_1(\lambda b)J_1(\lambda(b+d))}$$

Parameter definitions are the same as described for Eq. (1). J_2 and N_2 are 2nd-order Bessel functions of the 1st and 2nd kinds, respectively. If the pipe thickness becomes infinity, the expression is rewritten as Eq. (6) with the 1st-order and 2nd-order Hankel functions of the 1st kind, $H_1^{(1)}$ and $H_2^{(1)}$.

$$Z_{\perp}(\omega) = \frac{-i}{\pi\varepsilon_0 b^3\omega\left\{\left(\frac{2\omega}{\lambda c}+\frac{\lambda c}{\omega}\right)\frac{H_2^{(1)}(\lambda b)}{H_1^{(1)}(\lambda b)}-\frac{b\omega}{2c}\right\}} \qquad (6)$$

The conventional expression is derived from Eq. (6) on the conditions of $|\lambda|b >> 1$, $|\lambda| >> |\omega/c|$, $|\lambda| >> b\omega^2/c^2$ as follows:

$$Z_{\perp}(\omega) = \frac{Z_0\delta}{2\pi b^3}\{sgn(\omega)-i\} \qquad (7)$$

Figure 3 shows the real parts of the transverse resistive-wall impedances of SS pipes with b=25 mm calculated from Eqs. (5) and (6). For comparison, the conventional expression of Eq. (7) is shown in the figure. The real parts of the transverse impedances also have low and high frequency cut-offs, each of which has a very similar dependency on pipe radius and thickness to that of the longitudinal one. It should be noted that, as the frequency decreases, the real parts of the exact resistive-wall impedances go down to zero, while that of the conventional expression continues to increase.

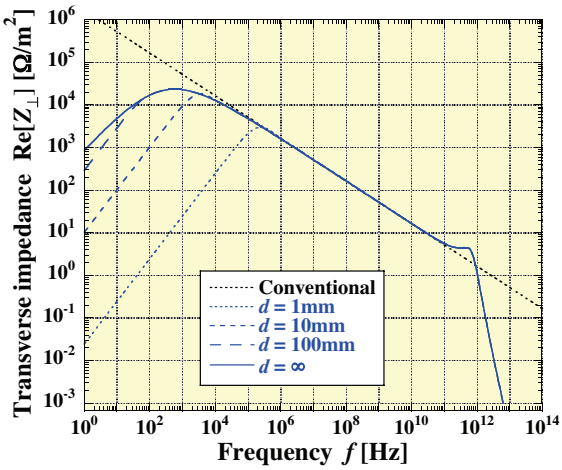

Figure 3: Transverse resistive-wall impedances of round pipes with an inner radius of 25 mm and thicknesses of 1, 10, 100 mm and infinity. The conventional impedance expression is also plotted by a black dotted line.

PARASITIC LOSS DUE TO LONGITUDINAL WAKEFIELDS

Loss Factor and Parasitic Loss

Loss factor of the resistive-wall pipe is expressed as Eq. (8) with the longitudinal impedance and the bunch length σ_t when the electron distribution of the bunch is Gaussian.

$$k = \frac{1}{\pi}\int_0^\infty Re\{Z_{//}(\omega)\}\exp\left\{-(\sigma_t\omega)^2\right\}d\omega \qquad (8)$$

If the bunch length becomes shorter, the high-frequency cut-off caused by the exponential term in Eq. (8) shifts to higher frequency and as a result the loss factor becomes higher. Since ERL-based SR sources have much shorter bunches than the storage-ring based SR sources, they have much higher loss factors.

Parasitic loss in a round pipe with the length L is expressed with the loss factor as

$$P_{RW} = kQ_b^2 f_b L = kI^2 L/f_b \qquad (9)$$

Here Q_b, f_b, and I are the bunch charge and the repetition frequency of bunches and the average beam current. The loss factor and parasitic loss per unit length in each of SS pipes with radii of 8 and 3 mm are calculated from Eqs. (8) and (9) for a typical ERL-based SR source (σ_t=1ps, I=100mA, f_b=1.3GHz):

k = 2.73(7.11) [V/pC/m] (b = 8(3)mm)

P_{RW}/L = 21.0(54.7) [W/m] (b = 8(3)mm)

The loss factor and the parasitic loss are also calculated for SPring-8 (σ_t=13ps, I=100mA, f_b=0.045GHz) as

k = 0.0562(0.150) [V/pC/m] (b = 8(3)mm)

P_{RW}/L = 13.3(35.3) [W/m] (b = 8(3)mm)

The typical ERL-based SR source has higher parasitic loss than SPring-8 (and than most of the existing 3rd generation SR sources) because of the higher loss factor.

Reduction of Parasitic Loss by Copper Coating

If a vacuum chamber is made of a very good electric conductor such as Cu for reducing the loss factor, eddy currents of the chamber can be considerable when the magnetic field of a magnet or insertion device is changed there. Cu coating is expected to reduce the loss factor of a SS vacuum chamber without significantly increasing effects of the eddy currents. As shown in Fig. 2, only 1-μm Cu coating can suppress the dominant high frequency component in the longitudinal impedance of the SS pipe. The loss factor and parasitic loss of the Cu-coated pipe are numerically calculated from Eqs. (8) and (9) as

k = 0.404(1.07) [V/pC/m] (b = 8(3)mm)

P_{RW}/L = 3.11(8.26) [W/m] (b = 8(3)mm)

The obtained parasitic loss is about one seventh of that of the pure SS pipe and equal to that of the pure Cu pipe. This calculation result confirms the effectiveness of Cu coating in reducing the parasitic loss of a SS vacuum chamber.

BEAM BREAKUP DUE TO TRANSVERSE WAKEFIELDS

Wake Function

The transverse wake function is expressed with the transverse impedance as in Eq. (10).

$$\begin{aligned} W_\perp(t) &= \frac{-i}{2\pi}\int_{-\infty}^{\infty} Z_\perp(\omega)e^{-i\omega t}d\omega \\ &= -\frac{2}{\pi}\int_{-\infty}^{\infty} Re\{Z_\perp(\omega)\}\sin(\omega t)d\omega \end{aligned} \qquad (10)$$

If Eq. (7) is used in Eq. (10) as the impedance, the conventional expression for the transverse wake function of a round pipe is obtained as Eq. (11), which is valid only for the condition of (12).

$$W_\perp(t) = -\frac{1}{\pi b^3 t^{1/2}}\sqrt{\frac{cZ_0}{\pi\sigma}} \qquad (11)$$

$$2\pi\sqrt[3]{b^2/\sigma Z_0}\,/c << t << 2\pi\mu_0\sigma b^2, t << 2\pi\mu_0\sigma d^2 \qquad (12)$$

Exact wake functions were numerically calculated from Eqs. (5) and (10). Red solid lines in Figs. 2(a) and 2(b) show the calculated exact wake functions for two different SS pipes with inner radii of 25-mm and 3-mm radius and a thickness of 1 mm. A black dotted line and a blue solid line in each figure show the conventional wake function of Eq. (11) and the ratio of the exact to the conventional wake function, respectively. As clearly shown by the ratio of the exact to the conventional wake function, each exact wake function more quickly and substantially decreases compared with the conventional wake function.

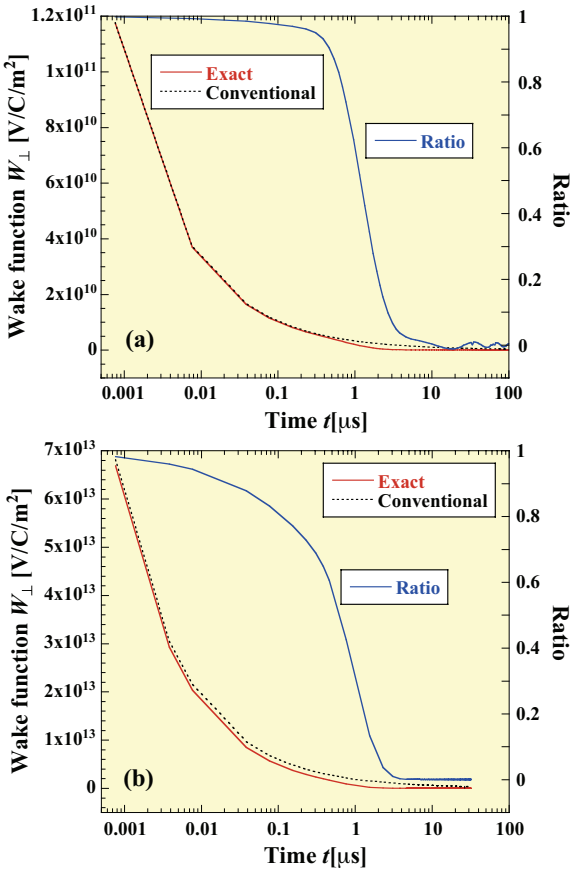

Figure 4: Exact transverse wake functions of two different SS pipes (red solid lines): (a) b=25mm and d=1mm and (b) b=3mm and d=1mm. black dotted and blue solid lines indicate the conventional expression and ratio of the exact to the conventional wake function, respectively.

Equation of Motion

The equation of transverse motion for the M-th electron bunch injected into an ERL under the resistive-wall wake is as follows:

$$y_M''(s) + K(s)y_M(s) = 0 \quad (M = 1) \tag{13}$$

$$y_M''(s) + K(s)y_M(s) = \sum_{N=1}^{M-1} h(M-N)y_N(s) \quad (M \geq 2) \tag{14}$$

$$h(M) = \frac{eI\tau_B}{E} W_\perp(M\tau_B), \quad I = \frac{eN_B}{\tau_B} \tag{15}$$

Here K, e, N_B, E and τ_B are the external focusing, the electron charge, the electron number per bunch, the electron energy and the time separation between bunches. The right-hand term of Eq. (14) means a transverse kick due to the resistive-wall wake. Since the bunch number M can be replaced with t/τ_B for $M >> 1$, the transverse position y_M of the M-th bunch is represented as a function of the time t and the longitudinal position s:

$$y_M(s) \rightarrow y(t,s),\ t \cong M\tau_B \left(M >> 1\right)$$

Hereafter $y(t,s)$ or y is used as the transverse beam position in place of y_M.

Resistive-Wall BBU Simulation

Based on Eqs. (13) to (15), resistive-wall BBU simulations in the compact ERL[3] were performed. Figure 5 shows layout of the compact ERL and the simulation path. The simulation start and end points are just after the acceleration and just before the deceleration due to accelerating cavities in the two superconducting (SC) cryomodules as shown in Fig. 5. The path length L between the two points is 55.44 m. In the simulations, effects of the magnet fields were not considered. The electron beam was assumed to have an energy of 60 MeV, a repetition rate of 1.3 GHz and an average beam current of 100 mA (a bunch charge of 77pC). All the bunches were injected with an initial position offset y_0 at the simulation start point. The transverse beam position y can always be normalized by y_0.

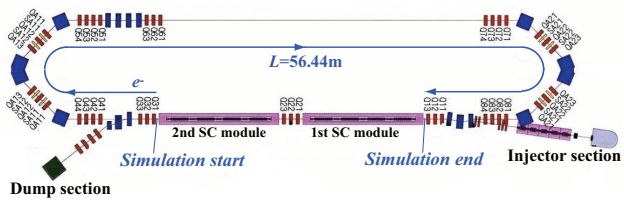

Figure 5: Layout of the compact ERL and the simulation path.

First the vacuum duct of the compact ERL was assumed to be a round SS pipe with b=25mm and d=1mm. The 25-mm radius is standard for the compact ERL vacuum ducts. Figure 6(a) shows the simulation result of the transverse beam motion for this SS pipe. The transverse beam position y at the simulation end point is increased with time and then saturated to 2 % of y_0 in a short time. In this case, effects of the resistive-wall wake are not serious. On the other hand, when the conventional wake function is used in the simulation, the transverse position is not saturated and increased infinitely with time. But this is not true. It is essential to use the exact wake function for correctly studying the resistive-wall BBU. Next the vacuum duct was assumed to be a round SS pipe with b=3 mm and d=1 mm. Figure 6(b) shows the simulation result. Although the transverse beam position is also saturated, it is increased up to 28 times of y_0. In this case, the beam hits the pipe when the initial position offset is larger than 110 μm, and the resistive-wall BBU can easily occur. Generally, when the beam energy is low and the pipe is very narrow and long, the resistive BBU becomes serious.

Finally transverse beam motion was simulated in a long undulator vacuum chamber (b=3 mm, d=1 mm) of a 5-GeV ERL SR source with a repetition rate of 1.3 GHz and an average beam current of 100 mA. The length of the undulator vacuum chamber was considered up to 100 m. Effects of magnetic field of the undulator was not considered. Figures 7(a) and 7(b) show the simulated transverse beam position at the exit of the 100-m chamber as a function of time and the dependence of the saturated position on the chamber length (at t=32.3 μs). Since the

beam energy is high, the transverse beam position is saturated to about 30 % of y_0 even for the chamber length of 100 m. The beam position displacement becomes smaller when the chamber length is shorter as shown in Fig. 7(b). However the assumed 1-mm thickness of the chamber is thinner than the ordinary one and the effective thickness including the surroundings such as undulator itself may have to be considered. Thus it is practically necessary to simulate transverse beam motions in thicker chambers

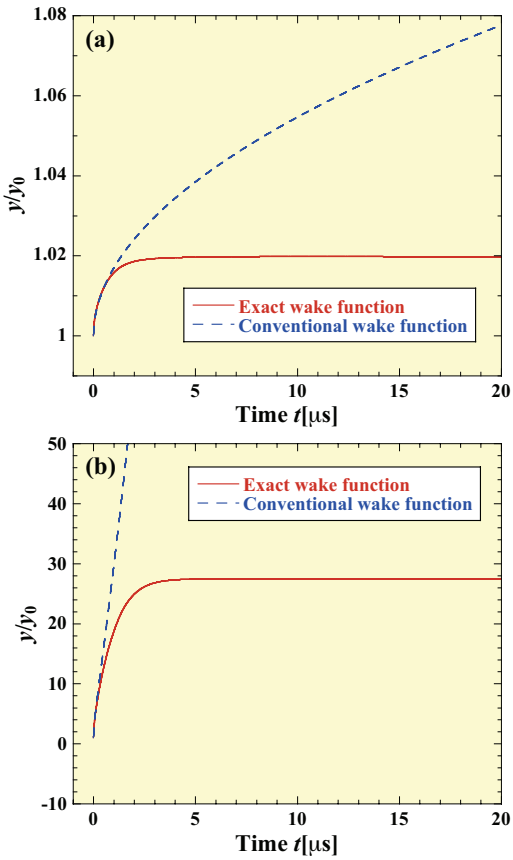

Figure 6: Simulated transverse beam position y normalized by y_0 in the compact ERL for SS pipes: (a) b=25mm and d=1mm and (b) b=3mm and d=1mm. Blue broken lines indicate simulation results using the conventional wake function.

SUMMARY

Exact expressions of longitudinal and transverse resistive-wall impedances of round pipes were obtained in order to correctly study effects of the resistive-wall wakefields. It was shown by calculations using the longitudinal impedance expressions that the parasitic loss of an ERL-based SR source can be higher than those of 3rd generation SR sources and at the same time that Cu coating can effectively reduce the impedance of a SS vacuum chamber. Based on the exact wake functions calculated from the transverse impedance expression, transverse beam motion was simulated for the compact ERL and an undulator chamber of a 5-GeV ERL and as a result it was found that the transverse beam position displacement due to the resistive-wall wakefields is saturated in a short time and does not continue to increase infinitely. The maximum position displacements in the compact ERL are 0.02 and 28 times of the initial position offset for the 1-mm thick SS vacuum pipes with 25 and 3 mm radii, respectively. The resistive-wall BBU is serious in the latter case and not in the former case. In the SS undulator chamber with 3-mm radius and 1-mm thickness of the 5-GeV ERL, the maximum position displacement was 30 % of the initial position offset even for 100-m chamber length because of the higher energy. Further simulations in thicker vacuum chambers are needed for more practical situations.

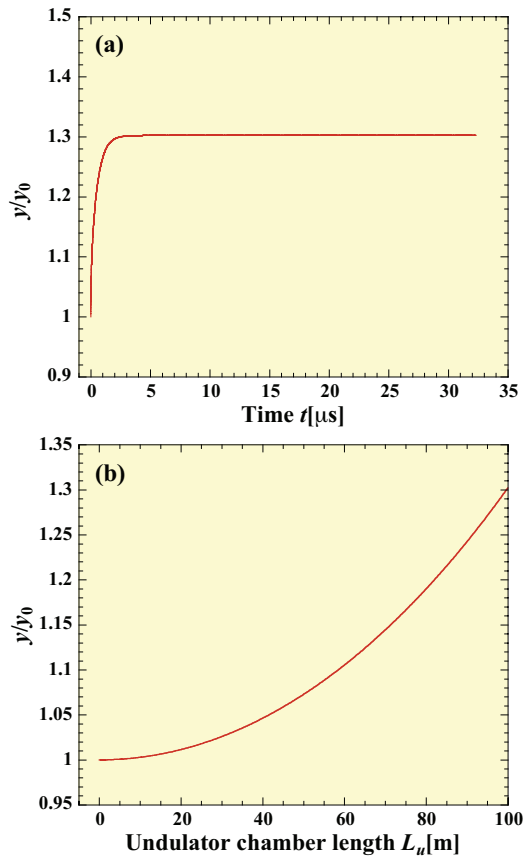

Figure 7: Simulated transverse beam position y normalized by y_0 in an undulator SS vacuum chamber: (a) dependence on time at L_u=100 m and (b) dependence on chamber length at t=32.6 μs.

REFERENCES

[1] J. M. Wang and J. Wu, Phys. Rev. ST Accel. Beams **7**, 034402(2004).
[2] N. Nakamura, Proceedings of ERL07, Daresbury Laboratory, May 21-25, pp45-49(2007).
[3] R. Hajima, N. Nakamura, S. Sakanaka, Y. Kobayashi (eds.), KEK Report 2007-7/JAEA-Research 2008-032.

List of Authors

Italic papercodes indicate primary authors

Institutes List

ASTeC, STFC Daresbury Laboratory
- Angal-Kalinin, D.
- Jones, L.
- McIntosh, P.
- Militsyn, B.
- Smith, S.
- Wheelhouse, A.

Advanced Energy Systems, Inc.
- Bluem, H.

Advanced Light Source
- Steier, C.

Argonne National Lab
- Borland, M.
- Dong, X.
- Harkay, K.
- Li, Y.
- Lill, R.
- Liu, Z.
- McNulty, I.
- Sajaev, V.
- Wang, C.
- Xiao, A.
- Yang, B.

BESSY
- Kugler, O.

Brookhaven National Lab
- Burrill, A.
- Hahn, H.
- Hammons, L.
- Kayran, D.
- Pozdeyev, E.
- Rao, T.
- Smedley, J.

Ceramics Ltd.
- Nenasheva, E.

Connecticut College
- Pan, S.

Cornell University - CLASSE
- Bazarov, I.
- Belomestnykh, S.
- Bilderback, D.
- Billing, M.
- Chojnacki, E.
- Crittenden, J.
- Dunham, B.
- Ehrlichman, M.
- Hoffstaetter, G.
- Lakshmanan, M.
- Liepe, M.
- Loehl, F.
- Mayes, C.
- Mikhailichenko, A.
- Ouzounov, D.
- Padamsee, H.
- Sagan, D.
- Tigner, M.
- Veshcherevich, V.

DESY
- Froehlich, L.

Euclid Concepts, LLC.
- Kanareykin, A.

FNAL
- Hocker, A.
- Yakovlev, V.

FZD
- Teichert, J.

Helmholtz-Zentrum Berlin
- Kamps, T.

JAEA
- Hajima, R.
- Nishimori, N.
- Sawamura, M.

KEK
- Furuya, T.
- Kako, E.
- Kawata, H.
- Kazakov, S.
- Kobayashi, Y.
- Michizono, S.
- Miyajima, T.
- Noguchi, S.
- Sakai, H.
- Sakanaka, S.
- Sato, M.
- Shimada, M.
- Shishido, T.
- Takahashi, T.
- Umemori, K.
- Watanabe, K.
- Yamamoto, M.
- Yamamoto, Y.

Naval Postgraduate School
- Lewellen, J.

Niowave, Inc.
- Grimm, T.
- Pruitt, M.

Peking University
- Liu, K.

RIKEN / Spring-8
- Togawa, K.

Reed College
- Bjorkquist, R.

Research Center Karlsruhe
- Rossmanith, R.

TJNAF
- Benson, S.
- Biallas, G.
- Boyce, J.
- Bullard, D.
- Coleman, J.
- Douglas, D.
- Evtushenko, P.
- Gould, C.
- Grames, J.
- Grippo, A.
- Gubeli, J.
- Hannon, F.
- Hardy, D.
- Hernandez-Garcia, C.
- Jordan, K.
- Kelley, M.
- Klopf, J.
- Kortze, J.
- Marchlik, M.
- Marhauser, F.
- Moore, W.
- Neil, G.
- Poelker, M.
- Powers, T.
- Sexton, D.
- Shinn, M.
- Surles-Law, K.
- Tennant, C.
- Walker, R.
- Williams, G.
- Zhang, S.

University Karlsruhe
- Baumbach, T.
- Bernhard, A.
- Ehlers, S.
- Fuchert, G.
- Peiffer, P.

University of Tokyo
- Nakamura, N.
- Shinoe, K.

University of Wisconsin-Madison
- Allen, M.
- Fisher, M.
- Hjortland, A.
- Kleman, K.
- Legg, R.

Yale University
- Hirshfield, J.
- Shchelkunov, S.